3-23-2018

Methodology to Analyze Tropical Cyclone Intensity from Microwave Imagery

Matthew W. Perkins

Recommended Citation

Perkins, Matthew W., "Methodology to Analyze Tropical Cyclone Intensity from Microwave Imagery" (2018). *Theses and Dissertations*. 1753.
https://scholar.afit.edu/etd/1753

Methodology to Analyze Tropical Cyclone Intensity from Microwave Imagery

THESIS

Matthew W. Perkins, Captain, USAF
AFIT-ENP-MS-18-M-094

DEPARTMENT OF THE AIR FORCE
AIR UNIVERSITY

AIR FORCE INSTITUTE OF TECHNOLOGY

Wright-Patterson Air Force Base, Ohio

AFIT-ENP-MS-18-M-094

METHODOLOGY TO ANALYZE TROPICAL CYCLONE INTENSITY FROM MICROWAVE IMAGERY

THESIS

Presented to the Faculty
Department of Engineering Physics
Graduate School of Engineering and Management
Air Force Institute of Technology
Air University
Air Education and Training Command
in Partial Fulfillment of the Requirements for the
Degree of Master of Science in Atmospheric Science

Matthew W. Perkins, B.S.
Captain, USAF

March 22, 2018

DISTRIBUTION STATEMENT A
APPROVED FOR PUBLIC RELEASE; DISTRIBUTION UNLIMITED.

AFIT-ENP-MS-18-M-094

METHODOLOGY TO ANALYZE TROPICAL CYCLONE INTENSITY FROM MICROWAVE IMAGERY

THESIS

Matthew W. Perkins, B.S.
Captain, USAF

Committee Membership:

Robert A. Stenger, Ph.D.
Chair

Maj Omar A. Nava, Ph.D.
Member

Matthew E. Kucas, M.S.
Member

Abstract

Satellites with microwave remote sensing capabilities can be utilized to study atmospheric phenomena through high-level cloud cover (particularly cirrus), an advantage over visible and infrared bands, which only sense cloud tops. This unique capability makes microwave imagery ideal for studying the cloud structures of tropical cyclones (TCs) in detail, and relating these features to TC intensity. Techniques to estimate the intensity of TCs using infrared imagery, such as the Dvorak technique, have been used in TC forecasting for 40 years. However, due to the inherent temporal limitations of microwave imagery, no such similar technique exists for the microwave spectrum. This study utilizes pattern recognition to develop a subjective technique for estimating TC intensity using microwave imagery. The dataset includes TC composite imagery from the Special Sensor Microwave Imager (85 GHz), Advanced Microwave Scanning Radiometer-Earth Observing System (89 GHz), Advanced Microwave Scanning Radiometer 2 (89 GHz), and the Special Sensor Microwave Imager/Sounder (91 GHz) from the Atlantic basin, and aircraft reconnaissance data used for verification. The composite imagery is binned into four categories to facilitate detection of common patterns for TCs of similar size and estimated intensity. This analysis provides the foundation for a new method to estimate TC intensity when aircraft data are unavailable. Multiple techniques are applied to explore relationships between brightness temperature values and TC intensity, and ten test cases in the Western Pacific basin are presented to validate the results. Five out of the ten TCs were classified correctly applying the microwave intensity techniques developed by this analysis.

Acknowledgements

I truly could not have completed this research successfully without the help of several key contributors. First, I would like to express the utmost gratitude to my advisor and committee chair, Dr. Robert A. Stenger, for his continued direction and support during the past 18 months. His brilliant expertise in tropical meteorology was invaluable in guiding me during this project, and the numerous meetings, discussions, and feedback were all vital contributions towards its completion. I would also like to thank my committee members, Maj Omar A. Nava and Mr. Matthew E. Kucas. I arrived at AFIT with a lack of computer coding proficiency, but with Maj Nava's assistance I built the foundation for the most important portion of my methodology. My analysis would have never come to fruition without his input. Mr. Kucas was immensely helpful when I traveled to the Joint Typhoon Warning Center this summer, as I was initially unsure how to begin addressing my research topic. The ideas, suggestions, and advice he expressed during my visit jump-started my analysis process, and the continued feedback he provided the past nine months helped me worked through the various issues that arose.

Additionally, I would like to extend thanks to the Joint Typhoon Warning Center Director and the Satellite Operations Flight Commander for sponsoring my visit to Hawaii to observe daily operations and focus my research topic. The Director clarified the objective of the project, and explained the benefit to satellite operations. The Satellite Operations Flight Commander coordinated the details of my visit, and ensured maximum efficiency of my time spent there.

One of the best aspects of my time at AFIT was the fellowship and collective sharing of ideas and processes with all of my fellow classmates. I know we all learned something from one another, and the countless study sessions, feedback on project drafts, and even the meals we shared at a local pizza place most certainly helped me achieve my academic goals. I'd like to specifically thank a particular student for his help as I learned how to code, and his assistance in my efforts to acquire the data I needed for my thesis project. You know who you are.

Lastly, I would like to thank my parents, who continue to provide unwavering love and support in all of my career and academic endeavors. I would like to specifically thank my mom, who spent many hours reading my entire thesis draft. She provided a fresh set of eyes to identify issues I overlooked and subsequently corrected to successfully complete this project. Thank you again, and I love you both.

Matthew W. Perkins

Table of Contents

List of Figures

List of Tables

Table Page

METHODOLOGY TO ANALYZE TROPICAL CYCLONE INTENSITY FROM MICROWAVE IMAGERY

I. Introduction

1.1 Motivation

Natural disasters pose a threat to people, property, and resources on a nearly daily basis across the earth. In the United States (U.S.), the Department of Defense (DoD) seeks to minimize the impact of these phenomena and the effect they have on DoD assets globally. Tropical cyclones (TCs) are one type of natural disaster that form over relatively warm oceans and threaten coastlines each year. Severe flooding and significant wind damage are the two primary threats TCs pose. Timely and accurate TC forecasts are necessary to initiate precautionary measures to reduce the negative impact of TC interaction with DoD installations.

The DoD relies on Joint Typhoon Warning Center (JTWC) forecasts for all TCs in the Central Pacific, Western Pacific, South Pacific, and Indian ocean basins. TCs routinely affect dozens of DoD installations which contain tens of thousands of personnel and billions of dollars in assets and resources. False alarms can result in millions of dollars and thousands of man-hours wasted in needless storm preparation. Missed forecasts can lead to unexpected storm impacts due to an unanticipated landfall, jeopardizing lives and the DoD mission. In the Western Pacific basin, aircraft are routinely evacuated from Korea, Japan, and Guam in advance of expected TC impacts. Thus, improved accuracy in TC prediction can reduce needless evacuation and increase the confidence in advance warning when evacuation is required.

Meteorology forecasting in the 21st century is heavily reliant on the use of numerical weather prediction (NWP) models. NWP is more accurate when both in-situ and remotely sensed weather observations are present (Warner 2010). For TCs, in-situ observations over the ocean are limited to aircraft reconnaissance and to a lesser extent weather buoys. Remote sensing of TCs is possible using geostationary and polar orbiting satellite platforms from space. The data sensed by these satellites is vital in NWP assimilation to produce accurate TC forecasts.

1.2 Problem

The availability of in-situ observations is unfeasible in nearly all ocean basins for TC analysis. The DoD uses WC-130 aircraft with a variety of weather instruments to take observations in the Atlantic basin. Due to the limited range of these aircraft and the associated cost to operate them, TC aircraft reconnaissance is not available in the Pacific and Indian basins. In lieu of in-situ observations, visible and infrared imagery provide invaluable information for monitoring and tracking TCs, which could previously surprise coastlines and populous areas with little to no warning.

Remotely sensed data provides real-time monitoring of worldwide weather systems of various scales. Satellite meteorology initially utilized the visible and infrared spectra output images of cloud cover, water vapor, smoke, and volcanic ash (Kidder and Haar 1995). However, a limitation of these spectra is the inability to provide information on what is occurring beneath the cloud top (Wilheit et al. 1977). For TCs, this is problematic as these weather systems are primarily covered with an expansive cloud shield, masking important data within and beneath the cloud top layer.

1.3 Objective

Satellites with remote sensing capabilities in the microwave band can utilized to study phenomena in the earth-atmosphere system. Microwave electromagnetic (EM) radiation can be sensed through cloud cover, a limitation of visible and infrared bands which only sense cloud tops. This unique advantage makes microwave imagery ideal for studying TCs. Techniques to classify TC intensity using infrared imagery, such as the Dvorak technique (Dvorak 1975), have been used in TC forecasting for 40 years. Due to the inherent limitations of microwave imagery, no such technique exists for this spectrum. These limitations include poor spatial resolution compared to infrared imagery, inconsistent temporal resolution due to the nature of polar orbiting satellite passes, and signal attenuation due to water vapor and rain drops both in and below the various cloud layers (Petty 2006).

Despite these limitations, the objective of this research is to utilize microwave imagery to develop a technique to subjectively estimate TC intensity. This thesis will first explore the background information necessary to devise such a technique. A thorough literature review on radiant intensity, microwave spectrum absorption and scattering, TC characteristics and structure, and microwave remote sensing in TCs will summarize the relevant background information. Next, the methodology chapter will describe the data set selected and the process used to produce TC brightness temperature composite average imagery. This will be followed by an in-depth analysis of the imagery produced in the methodology section, including an instrument comparison analysis and validation of the results. Lastly, the conclusion chapter will summarize this thesis, describe limiting factors in the analysis and results, and list ideas for future work on this topic.

II. Background

2.1 Radiant Intensity

Remote sensing of atmospheric phenomena begins with the concept of radiant intensity and how it is affected by absorption, transmission, reflection, and emissivity properties. The radiance information that eventually reaches remote sensing satellites begins with emissivity from the earth surface and atmosphere. Planck's Function $B(T)$ for a blackbody temperature relates emissivity to wavelength λ and is given as

$$B_\lambda(T) = \frac{2hc^2}{\lambda^5(\exp{(\frac{hc}{k_B\lambda T})} - 1)}\ , \tag{1}$$

where T is temperature, Planck's constant $h = 6.626 \times 10^{-34}\ Js$, the speed of light $c = 2.998 \times 10^8\ m\ s^{-1}$, and Boltzmann's constant $k_B = 1.381 \times 10^{-23}\ J\ K^{-1}$. This intensity is the quantity of power per unit area per unit wavelength per unit solid angle, or $W\ m^{-2}\ \mu m^{-1}\ sr^{-1}$ (Petty 2006).

It is apparent from Eq. (1) that blackbody temperature and wavelength have an inverse relationship, and that the relationship is non-linear unless λ is sufficiently large. Shortwave EM radiation from the sun exists mostly in the visible spectrum, where T is large (approximately 6000 K) and λ is relatively small. EM radiation emitted from the earth is significantly cooler (approximately 250 K) and microwave spectrum wavelengths are three to six orders of magnitude greater than visible spectrum wavelengths. Thus, for these longer wavelengths ($\lambda \geq 1$ mm), the Rayleigh-Jeans Approximation is more appropriate

$$B_\lambda(T) = \frac{2ck_B}{\lambda^4}T\ , \tag{2}$$

where temperature and blackbody emission are proportional (Wacker 2005).

EM radiation emitted from the earth-atmosphere system undergoes attenuation from both absorption and scattering effects as it travels upward to a sensor. If the emitted EM radiation traveling some path (s) begins at s_1 and ends at the sensor s_2, the extinction of EM radiation can be described by Beer's Law:

$$I_\lambda(s_2) = I_\lambda(s_1)\ \exp\,[-\int\limits_{s_1}^{s_2} \beta_e(s)\ ds\,]. \tag{3}$$

In this equation, the fraction of emitted EM radiation that survives to the path end at s_2 is the intensity $I_\lambda(s_2)$. β_e is the extinction coefficient which accounts for absorption and scattering along the path s. The optical thickness (τ) of the path follows from Eq. (3) and is defined as

$$\tau(s_1, s_2) \equiv \int\limits_{s_1}^{s_2} \beta_e(s)\ ds\ . \tag{4}$$

Exponentiating this function gives the transmittance (Petty 2006) between s_1 and s_2 represented as a fraction between 0 and 1:

$$t(s_1, s_2) \equiv e^{-\tau(s_1,s_2)}. \tag{5}$$

The optical thickness and transmittance can be expressed in slightly different forms when considering the plane parallel atmosphere, where horizontal variations in atmospheric structure are ignored and all relevant radiative properties depend strictly on the vertical coordinate z (Petty 2006). In this case, $s = z\ \mu^{-1}$ where z is the height, and μ is a function of the incidence angle the emitted EM radiation takes between the vertical and sensor, given as $\mu = cos(\theta)$. At nadir, $\theta = 0°$ and $\mu = 1$, indicating no loss of EM radiation due to the angle of incidence. As EM radiation travels through varying heights, the rate of absorption is equal to the rate of change of the transmittance from any height z to the top of the atmosphere. This relationship is known as the weighting function, which provides a reference height that quantifies the amount of radiation emitted from a layer of the atmosphere for a given frequency.

Kirchoff's law states that absorption of radiation is equal to emission (ε). Planck's function in Eq. (1), Beer's law in Eq. (3), the weighting function, and accounting for surface contributions to upward intensity gives the solution for total EM radiation sensed at the top of the atmosphere, where the brightness temperatures (T_B) are approximated by Eq. (2) for microwave imagery. The T_B values correspond to a layer in the atmosphere where the weighting function peaks (Petty 2006).

2.2 Microwave Absorption and Scattering

EM radiation in the microwave spectrum can be absorbed, scattered, or both. The determining factors depend on the wavelength of the EM radiation as well as the size, shape, incident angle, and molecular properties of the atmospheric constituent it comes into contact with. Water vapor and oxygen absorb (but do not scatter) at various wavelengths, liquid water can scatter and absorb, and ice will scatter (but not absorb) EM radiation (Petty 2006).

Absorption by water vapor and oxygen occurs primarily in four regions of the microwave spectrum. These regions of non-transmittance are depicted in Figure 1. Oxygen absorbs at 60 GHz and again at 118 GHz. Oxygen is well mixed throughout the atmosphere, thus utilization of channels near these bands can provide T_B values at various levels in the atmosphere. Water vapor weakly absorbs at 22 GHz and strongly absorbs at 183 GHz. For regions of the earth with high average water vapor content, such as the tropics, the bandwidth of absorption is wider and ranges from 176 to 190

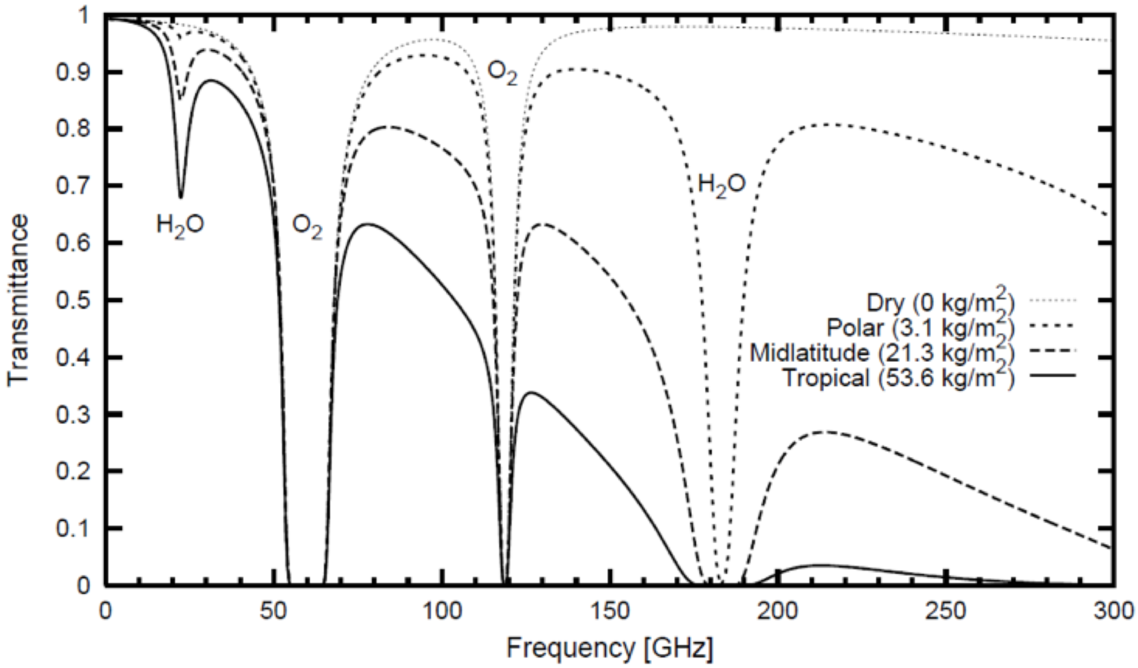

Figure 1: Zenith microwave transmittance of the cloud-free atmosphere. Spectral viewing windows for H_2O and O_2 are highlighted. These windows vary depending on the average water vapor content associated with each climatological region (Petty 2006). Used with permission.

GHz. The absorption bandwidth decreases as available water vapor content decreases, and is quite narrowly centered around 183 GHz for deserts and polar regions (Petty 2006).

Scattering of EM radiation begins with liquid cloud droplets and rain drops, although absorption still dominates in the liquid phase. Two regimes exist to describe the scattering of radiation for liquid water: Rayleigh scattering for droplets with a small radius (cloud droplets); and Mie scattering for larger drops (rain drops).

In Figure 2, particle size is correlated to each regime as a function of wavelength. In both regimes, scattering is minimal below the oxygen absorption band centered at 60 GHz (depicted in Figure 1), and absorption of EM radiation occurs for liquid water at these low frequencies. Scattering begins to increase above 60 GHz and is much more important in the high microwave frequencies. Scattering negatively affects the ability to measure EM radiation effectively, thus the highly absorptive band for water vapor centered around 183 GHz is contaminated when liquid water is present. Ice particles scatter even more rapidly than liquid water, thus above 50 GHz, microwave radiation cannot transmit through ice (Raschke 2013).

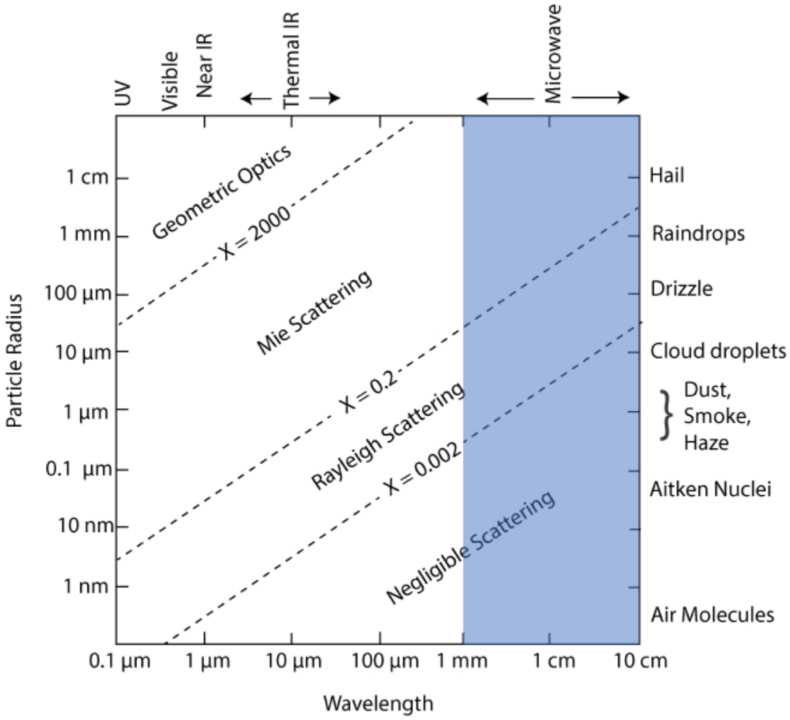

Figure 2: Relationship between particle size, radiation wavelength, and scattering behavior for atmospheric particles. Dashed lines represent rough boundaries between scattering regimes. Microwave wavelengths are highlighted in blue. Adapted from (Petty 2006). Used with permission.

2.3 Tropical Cyclones

TCs are intense, warm core, cyclonic atmospheric vorticies that form over the ocean waters predominantly equatorward of 30 degrees latitude north and south. TCs require five primary initial conditions for cyclogenesis (Chan and Kepert 2010). First, TCs require relatively warm ocean temperatures above 300 K that extend at least 50 m below the ocean surface. Next, a conditionally unstable layer must be present that extends from the surface to the upper troposphere. Relatively high values of low-level cyclonic absolute vorticity are also necessary for TC formation, thus TCs rarely form equatorward of 5 degrees latitude north and south. Additionally, high mid-level humidity and large scale mean ascent provide ideal environmental conditions, but they must be coupled with areas of organized deep convection. Lastly, relatively weak vertical wind shear is required for TC formation. TCs that form and move over ocean regions with these five characteristics will typically deepen, particularly if these conditions are enhanced. Warming ocean temperatures, decreasing vertical wind shear, and increasing deep-layer instability are examples of conditions that denote positive feedback processes in TCs.

2.3.1 TC Organization and Structure

As surface low pressure deepens, TCs typically become more axisymmetric with respect to the overall satellite appearance as well as the intense wind field that extends from the TC center (Chan and Kepert 2010). TCs are organized in spiral rain bands that move both cyclonically and generally outward from the TC center. Mature, intensifying TCs can develop a defined center that is evident in microwave imagery where a relatively small enclosed area of warm T_B values is surrounded by cold T_B values. This TC center, or *eye*, is characterized by warm, sinking air throughout the vertical column, as well as light wind speeds. The concentric ring of convection just outside the eye, known as the *eye wall*, contains the strongest winds in organized TCs. Outside the eye wall, the TC wind field decreases as radial distance from the TC center increases. Particularly intense TCs undergo secondary eye wall formation (SEF), where an outer ring of concentric convection forms and contracts inward as wind speeds increase. The inner eye wall, which contains the TC maximum surface wind speed (V_{max}), decreases in intensity until V_{max} is contained within the secondary eye wall. The secondary eye wall replaces the inner eye wall, and the process is known as an *eye wall replacement cycle*. SEF can briefly decrease V_{max} and increase the surface pressure in the TC center. The relative convective void between the inner eye wall and secondary eye wall is the *moat*. Figure 3 depicts a sample of TC structure in Hurricane Frances (2004; Sitkowski et al. 2011).

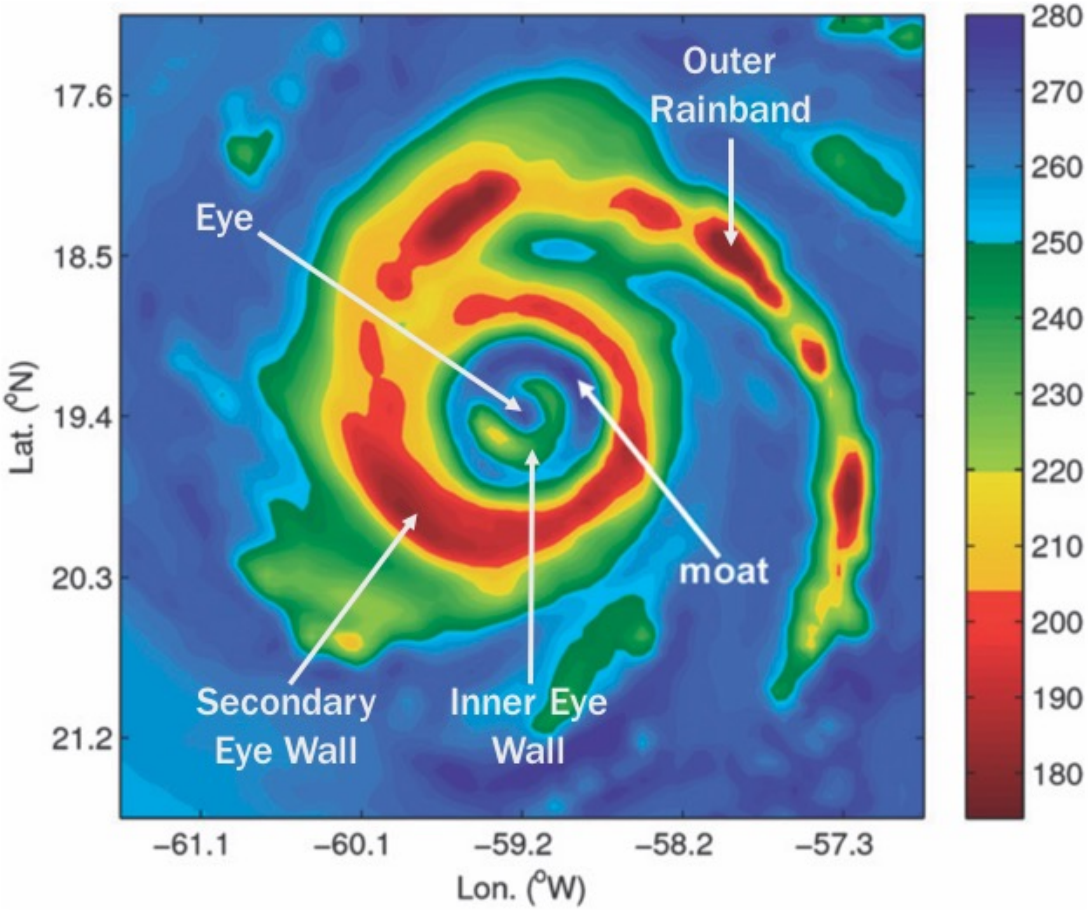

Figure 3: AMSR-E imagery with colors representing T_B values (K) from Hurricane Frances (2004) at 1709 UTC (Coordinated Universal Time) on 30 August. A well-defined warm moat appears between the two convective (cold) eye walls (Adapted from Sitkowski et al. 2011). ©American Meteorological Society. Used with permission.

2.3.2 TC Locations and Classification

TCs form and mature in seven primary ocean basins around the world. These seven ocean basins are the Atlantic, Eastern Pacific, Central Pacific, Western Pacific, Southern Pacific, Northern Indian, and Southern Indian oceans. This paper will focus on four of these seven basins: Atlantic, Eastern Pacific, Central Pacific, and Western Pacific.

The nomenclature for a TC varies by ocean basin and is further broken down into categories in some regions. TCs are referred to as tropical depressions, tropical storms, and hurricanes in the Atlantic, Eastern Pacific, and Central Pacific basins. TCs are further classified by category once they reach hurricane strength as depicted in Table 1. TCs typically form in the Atlantic basin between June and November, though rare exceptions occur outside this range of months. Atlantic TCs form between the west coast of Africa and the east coasts of the U.S. and Central America, tracking west to northwest in the tropics and turning north to northeast in the mid-latitudes. The relatively warm ocean temperatures throughout the Atlantic basin allow TCs to persist up to and beyond 50 degrees north in latitude.

Eastern Pacific TCs form off the east coast of Central America between May and November, tracking west to northwest before dissipating over the cool ocean temperatures north of 30 degrees north in latitude. Central Pacific TCs form from May to November between 140 and 180 degrees west in longitude. TCs do not regularly form in this ocean basin due to marginal ocean temperatures, though the region becomes more active during seasons with above average ocean temperatures, such as El Niño years. Western Pacific TCs can form year-round, but primarily form between April and January between 100 and 180 degrees east in longitude. TC movement in this region is similar to the Atlantic basin, tracking west to northwest in tropical latitudes before turning north to northeast in the mid-latitudes. Western Pacific TCs are referred to as typhoons rather than hurricanes, and are not further broken down into numerical categories. Extremely intense typhoons are denoted as super typhoons as depicted in Table 1. The Western Pacific is the most active basin each year on average, due to consistently ideal formation conditions as described in section 2.3.

Table 1: TC wind speed and nomenclature for Atlantic, East and Central Pacific, and Western Pacific basins (Chan and Kepert 2010).

Wind Speed [kt]	Atlantic Ocean, Central and East Pacific	Western Pacific
≤ 33	Tropical depression	Tropical depression
34 - 63	Tropical storm	Tropical storm
64 - 82	Cat 1 Hurricane	Typhoon
83 - 95	Cat 2 Hurricane	Typhoon
96 - 112	Cat 3 Hurricane	Typhoon
113 - 136	Cat 4 Hurricane	Typhoon
≥ 137	Cat 5 Hurricane	≥ 130 Super Typhoon

2.4 Microwave Remote Sensing in TCs

TCs can be remotely sensed by instruments aboard polar orbiting satellites in low earth orbit. Various microwave frequencies can be exploited to obtain information on different TC characteristics. In general, low frequencies provide information closest to the earth's surface, and high frequencies provide information furthest from the earth's surface due to the transmittance properties in each band. For example, Figure 1 depicts high transmittance of both oxygen and water vapor near 0 GHz.

Frequencies of approximately 5 GHz are used to transmit through the TC and detect phenomena at the surface, such as ocean wave speed and direction (Figa-Saldaña et al. 2002). Water vapor transmittance has a relative minimum at approximately 22 GHz, and a relative maximum at approximately 37 GHz (Petty 2006). Ice is minimally scattered below 50 GHz, thus 37 GHz is ideal for detection of rain drops. In particular, 37 GHz highlights large raindrops that have grown by collision coalescence as they fall through the cloud towards the earth's surface. Thus, this frequency provides low-level information within the TC. The frequencies from 85-91 GHz are a relative maximum for oxygen transmittance, and similar to the 37 GHz band, rain drops are easily detected. Because microwave radiation cannnot transmit through ice above 50 GHz, this range of frequencies also highlights ice particles by scattering. Thus, these frequencies detect deep convection where rain drops and ice particles are present (Cecil and Zipser 1999). Deep convection in the TC eye wall is a direct indicator of TC wind intensity. Thus, the frequencies between 85 GHz and 91 GHz are the most useful for determining TC intensity information.

2.4.1 Special Sensor Microwave Imager (SSMI) and Special Sensor Microwave Imager/Sounder (SSMI/S)

The SSMI/S instrument was first launched on 18 October, 2003, aboard the Defense Meteorological Satellite Program (DMSP) F-16 satellite (Poe et al. 2001). Currently, SSMI/S is carried aboard DMSP F-16, F-17, and F-18 satellites. SSMI/S is the successor to SSMI, and features some additions to its predecessor that make it ideal for interrogating TCs. Both SSMI and SSMI/S fly on polar orbiting satellites, and both use a conical scanning strategy. Conical scanning has an inherent advantage over cross-track scanning instruments as the imagery resolution does not degrade from nadir to the edge of the scanning footprint. Figure 4 depicts the conical scan strategy for SSMI/S. SSMI has a 1400 km swath width with 12.5 km resolution at 85 GHz, whereas SSMI/S increases this width to 1707 km and maintains 12.5 km resolution at 91 GHz. The extra 307 km captured in each scan reduces the possibility of not sensing a TC due to the spatial gap in data between ascending and descending passes in the polar orbit. Additionally, SSMI/S senses microwave radiation at 91 GHz, whereas SSMI uses an 85 GHz channel. The change to 91 GHz alters the T_B values

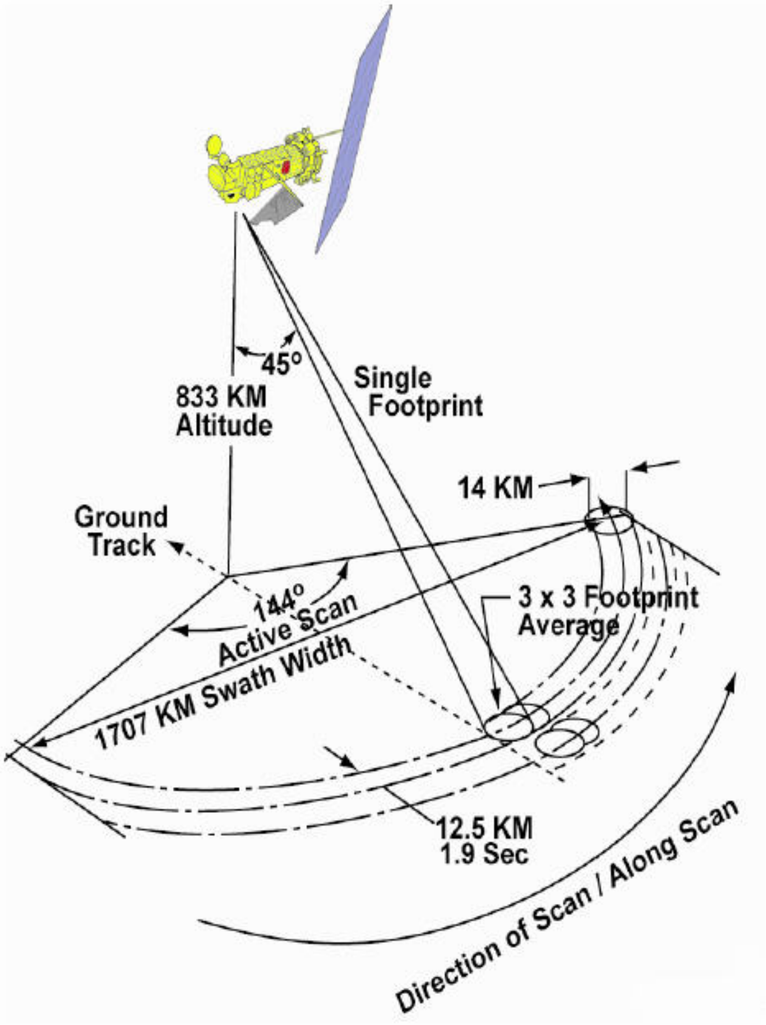

Figure 4: SSMI/S scan geometry (Poe et al. 2001).

sensed by SSMI/S compared to SSMI. The 91 GHz band is more sensitive to frozen hydrometeors than 85 GHz. Thus, SSMI/S can scan the exact same phenomena as SSMI and return different T_B values due to the difference in frequency. The 91 GHz T_B values are typically lower than the 85 GHz values, which highlight regions of enhanced convective activity in TCs better than 85 GHz bands. Thus, SSMI/S is a better choice than SSMI for sensing microwave radiation associated with TCs. SSMI/S is ideal due to its increased scan width, and its 91 GHz band for sensing ice associated with convective processes indicative of TC intensity. Figure 5 depicts SSMI and SSMI/S for Typhoon Saomai (2006) retrieved from the Naval Research Library (NRL) public website. Though the images were captured less than 15 minutes apart, the SSMI/S image depicts additional regions in the TC eye wall and rain bands where T_B is 210 K or lower compared to the SSMI imagery (Hawkins et al. 2008).

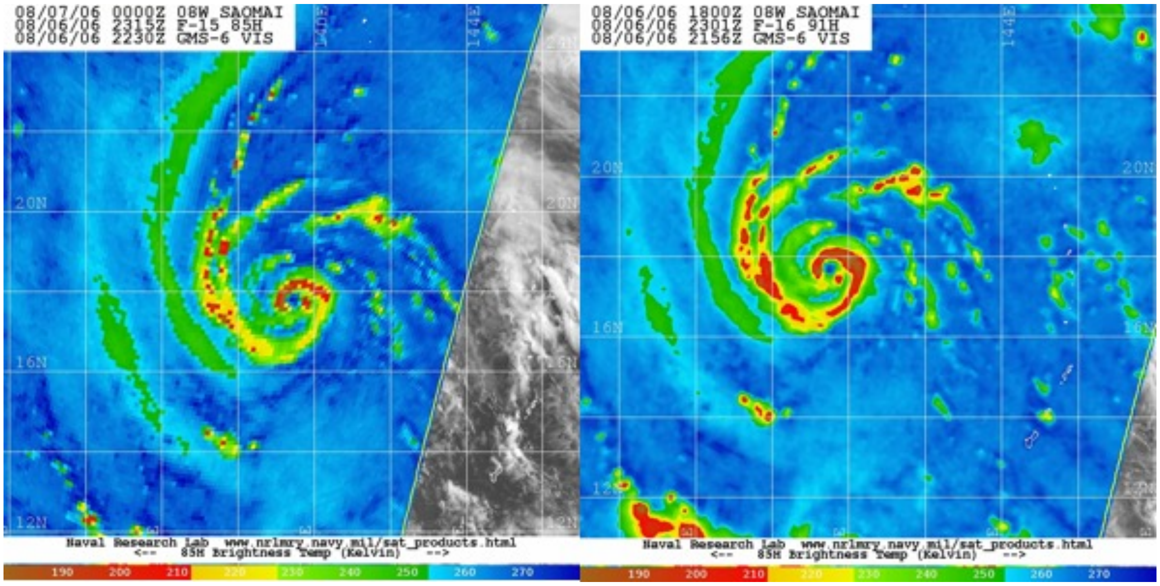

Figure 5: DMSP F-15 SSMI 85 GHz (left) and F-16 SSMI/S 91 GHz (right) imagery of Typhoon Saomai (2006) on 6 August at 2315 UTC (left) and 2301 UTC (right; from NRL 2017).

2.4.2 Advanced Microwave Scanning Radiometer for the Earth Observing System (AMSR-E) and Advanced Microwave Scanning Radiometer 2 (AMSR2)

The AMSR-E instrument was launched on May 4, 2002, aboard the National Aeronautics and Space Administration (NASA) satellite Aqua. Similar to SSMI and SSMI/S, AMSR-E flew aboard a polar orbiting satellite, and used a conical scanning strategy to minimize degradation of the scanned footprint at the edge of the scanning swath. AMSR-E had a 1450 km swath width, which is slightly larger than the 1400 km width of SSMI, but smaller than the 1707 km width of SSMI/S (Poe et al. 2001; Du et al. 2014). AMSR-E used an 89 GHz band for detection of deep TC convection, which highlights ice particles more than the 85 GHz band in SSMI, but slightly less than the 91 GHz band in SSMI/S. AMSR-E features superior resolution at 5 km for each individual sample in the 89 GHz band, compared to the 12.5 km resolution of SSMI at 85 GHz and SSMI/S at 91 GHz. AMSR-E was operational until 4 October, 2011, when it ceased rotating. The successor to AMSR-E, AMSR2, was launched on 18 May, 2012. AMSR2 flies on the Global Change Observation Mission (GCOM) W1 polar orbiting satellite. AMSR2 also uses the 89 GHz band, and the resolution is similar at 4 km. Thus, data sets from AMSR-E and AMSR2 can be used in conjunction with one another as there is no change to frequency, and insignificant change to spatial resolution and T_B values between instruments. A comparison between the two instruments is depicted in Table 2.

Table 2: Instrument characteristics for AMSR-E and AMSR-2 (Du et al. 2014). ©Multidisciplinary Digital Publishing Institute. Used with permission.

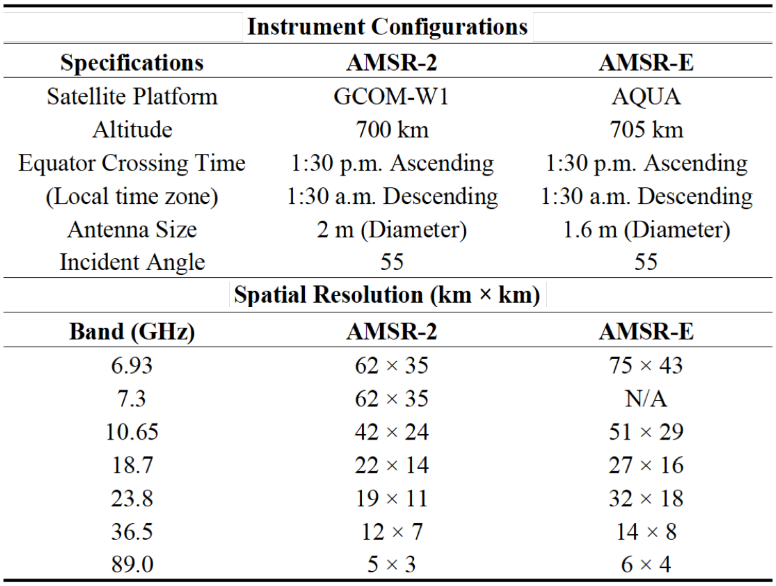

	Instrument Configurations	
Specifications	**AMSR-2**	**AMSR-E**
Satellite Platform	GCOM-W1	AQUA
Altitude	700 km	705 km
Equator Crossing Time	1:30 p.m. Ascending	1:30 p.m. Ascending
(Local time zone)	1:30 a.m. Descending	1:30 a.m. Descending
Antenna Size	2 m (Diameter)	1.6 m (Diameter)
Incident Angle	55	55
	Spatial Resolution (km × km)	
Band (GHz)	**AMSR-2**	**AMSR-E**
6.93	62 × 35	75 × 43
7.3	62 × 35	N/A
10.65	42 × 24	51 × 29
18.7	22 × 14	27 × 16
23.8	19 × 11	32 × 18
36.5	12 × 7	14 × 8
89.0	5 × 3	6 × 4

2.4.3 Tropical Rainfall Measurement Mission (TRMM) Microwave Imager (TMI)

The TMI instrument was launched on November 27, 1997, aboard the NASA and Japanese Aerospace Exploration Agency (JAXA) joint satellite TRMM. Unlike many satellites carrying microwave instruments for studying atmospheric phenomena, TRMM orbited the earth in a unique non-sun synchronous manner. The ascending (descending) passes of TRMM ended at 35 degrees north (south) rather than passing over the north (south) pole (Lee et al. 2002). Thus, TRMM captured data only over the tropical and subtropical regions of the planet. TRMM used a conical scanning strategy (depicted in Figure 6) similar to polar orbiting satellites.

TRMM was lower in altitude at 403 km than the typical polar orbiting satellites above earth that range from 700 to 850 km in altitude. As a result, the swath width for each TMI pass was only 758.5 km. TMI used a 85 GHz band for detecting scattering due to ice particles in TCs, similar to SSMI. The closer proximity to the earth's surface resulted in improved resolution for TMI at approximately 7 km for the 85 GHz, compared to SSMI and SSMI/S at 12.5 km for 85 GHz and 91 GHz, respectively. Table 3 depicts the frequency, polarization, and resolution characteristics for TMI. TRMM's orbit decayed after losing fuel in 2014, and it was deactivated on April 9, 2015.

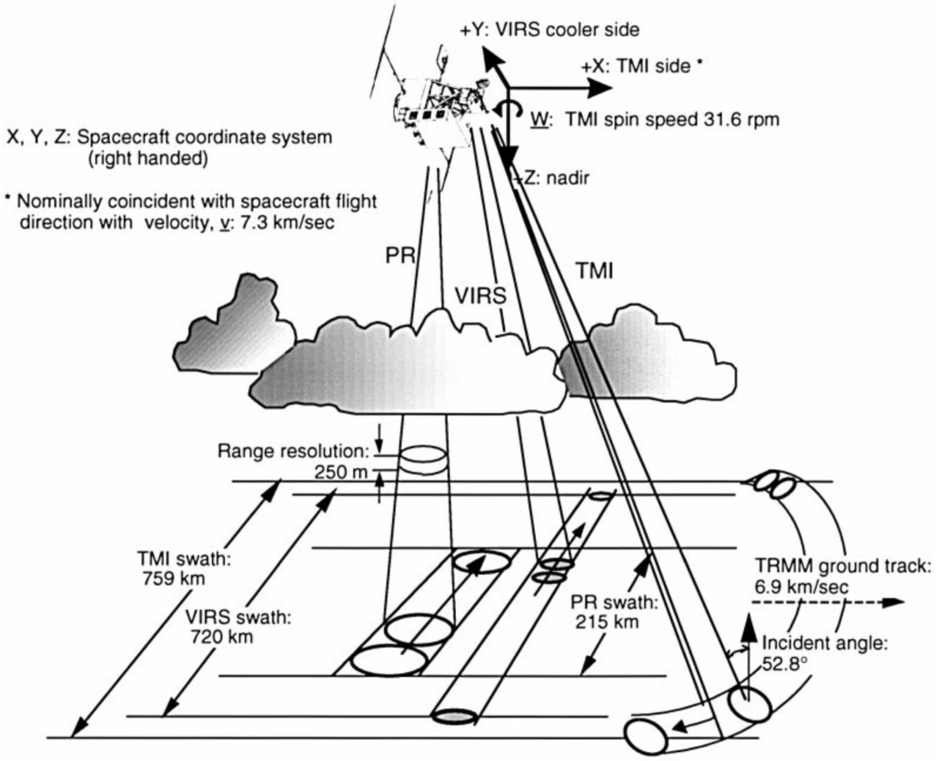

Figure 6: TRMM scan geometry (Kummerow et al. 1998). ©American Meteorological Society. Used with permission.

Table 3: TMI instrument characteristics (Lee et al. 2002). ©American Meteorological Society. Used with permission.

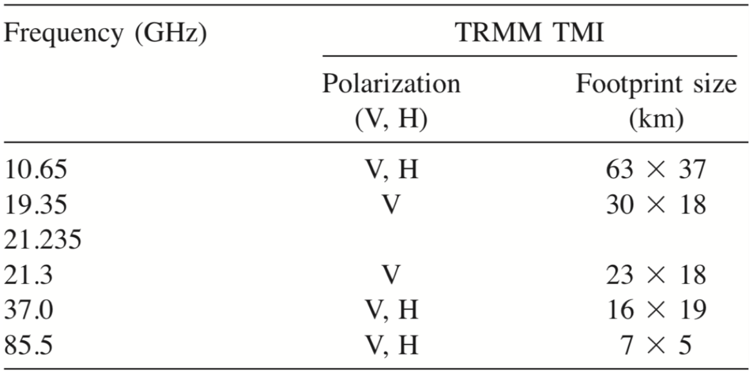

Frequency (GHz)	TRMM TMI	
	Polarization (V, H)	Footprint size (km)
10.65	V, H	63 × 37
19.35	V	30 × 18
21.235		
21.3	V	23 × 18
37.0	V, H	16 × 19
85.5	V, H	7 × 5

2.5 Previous Research

2.5.1 Warm Anomaly Technique: SCAMS

Satellites began using microwave bands to sense meteorological phenomena in the 1970s. The Scanning Microwave Spectrometer (SCAMS) on the Nimbus 6 was the earliest microwave instrument used to infer TC intensity through the warm anomaly technique. Kidder et al. (1978) related temperature anomalies in the upper troposphere to the surface pressure gradient and wind speed based on hydrostatic and pressure gradient relationship equations. As discussed in the background section, the weighting function provides a reference height for the highest quantity of radiation reaching a satellite sensor. The weighting function for the 55 GHz channel on SCAMS (depicted in Figure 8) peaked in the region of maximum temperature anomaly, between 100 and 200 millibars in the upper troposphere. In Figure 7, 36 TCs of varying strength are plotted as a function of T_B anomaly, with the majority of TCs between 940 and 1000 millibars.

A correlation coefficient of -0.89 provided strong evidence that the warm anomaly technique is valid. Determining finer scale features was not possible in this era as the

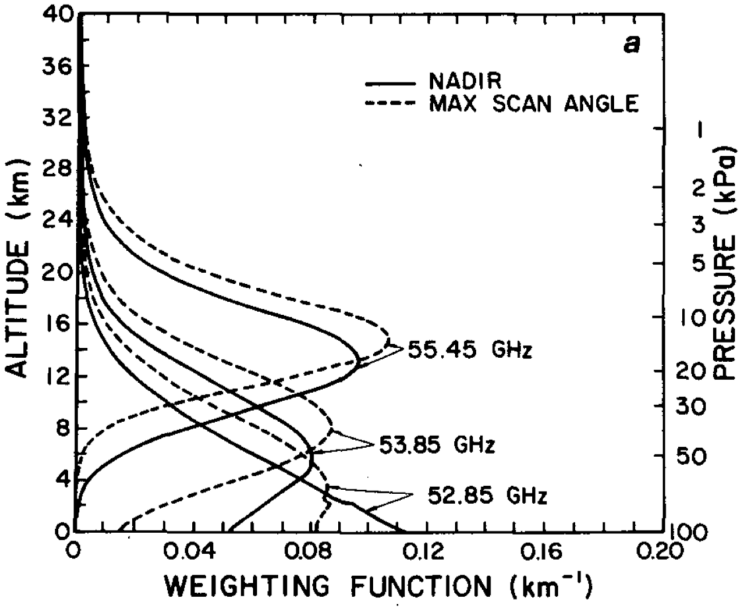

Figure 7: SCAMS weighting function for the 15 degrees North Annual Atmosphere (Kidder et al. 1978). ©American Meteorological Society. Used with permission.

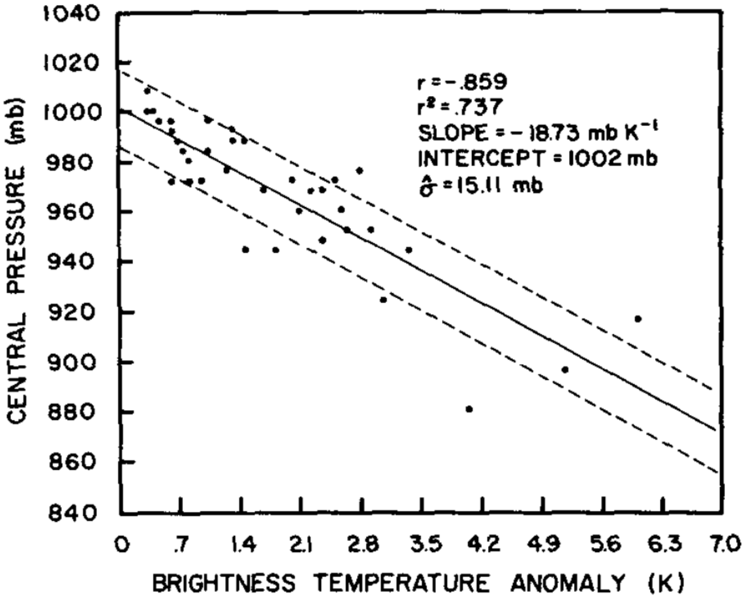

Figure 8: Central surface pressure versus temperature anomaly for 36 TCs (64 knots or greater) (Kidder et al. 1978). ©American Meteorological Society. Used with permission.

resolution of the imagery was only 145 km at nadir, and up to 360 km at the maximum scan angle. Thus, each data point in the instrument scan encompassed a large portion of the TC. This binary indication of warm anomaly values averaged throughout the TC was not particularly useful for operational forecasters determining the predicted TC track or intensification rate of change. Similar experiments continued through the 1980s and 1990s as new satellites with better resolution continued to confirm the warm anomaly technique as a valid practice for determining TC intensity in mean sea level pressure (MSLP). In the early 2000s, research using the current generation of instruments began.

2.5.2 Warm Anomaly and Center Fix Technique: AMSU

The Advanced Microwave Sounding Unit (AMSU) launched in 1998 featured a significant improvement in resolution, with 45 km available at nadir and 147 km at the maximum scan angle. In addition to AMSU-A providing higher resolution upper tropospheric T_B data in the near-oxygen bands between 50 and 55 GHz, the 89 GHz channel on AMSU-B or its replacement, MHS, can be used to locate the TC center. In section 2.2, Figure 1 depicts an oxygen transmittance maximum between the highly absorptive frequencies at 60 and 118 GHz. Ice crystals strongly attenuate the EM radiation by scattering, which results in relatively cool T_B values. These cool regions depict enhanced convective activity in the eye wall of the TC. A T_B maximum inside the eye wall depicts the TC center. Thus, the location of the TC center can be inferred using the 89 GHz channel in addition to the warm anomaly technique in the bands between 50 and 55 GHz (Brueske and Velden 2003). Figure 9 depicts the upper tropospheric warm anomaly for Hurricane Bonnie (1998) as a cross section using bands between 50 and 55 GHz. The warm anomaly is centered over 75°W, and the cross section is plotted along 29°N. Thus, a reasonable approximation of the TC eye size and location can be inferred using this technique. Figure 10 depicts

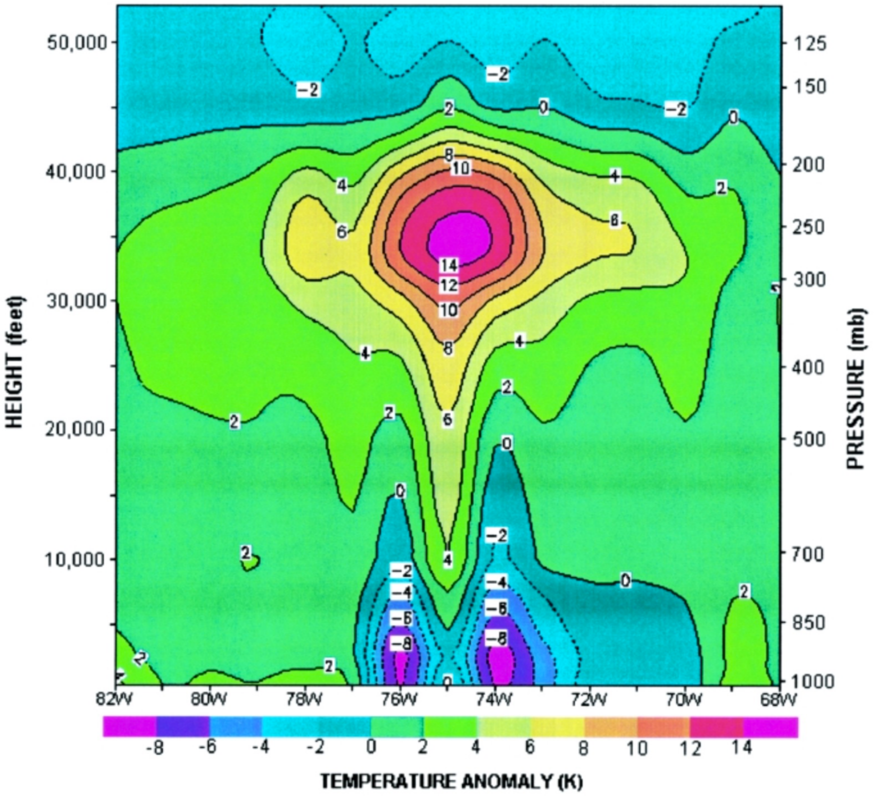

Figure 9: Cross section of temperature anomalies through Hurricane Bonnie (1998) on 25 August at 1200 UTC retrieved from AMSU data (Brueske and Velden 2003). ©American Meteorological Society. Used with permission.

microwave and infrared imagery for Hurricane Isidore (2002). The TC eye is obscured in the infrared imagery, but is clearly evident in the AMSU-B imagery as a 270 K T_B maximum value relative to the TC inner core.

2.5.3 Wind Retrieval Technique

Wind retrieval in TCs cannot be directly measured using passive microwave remote sensors. Active microwave sensors, such as the Advanced Scatterometer (ASCAT), emit a microwave signal downward through the earth-atmosphere system. This 5 GHz signal can transmit through both oxygen and water vapor (Figa-Saldaña et al. 2002). The EM radiation is backscattered off the ocean surface upward to

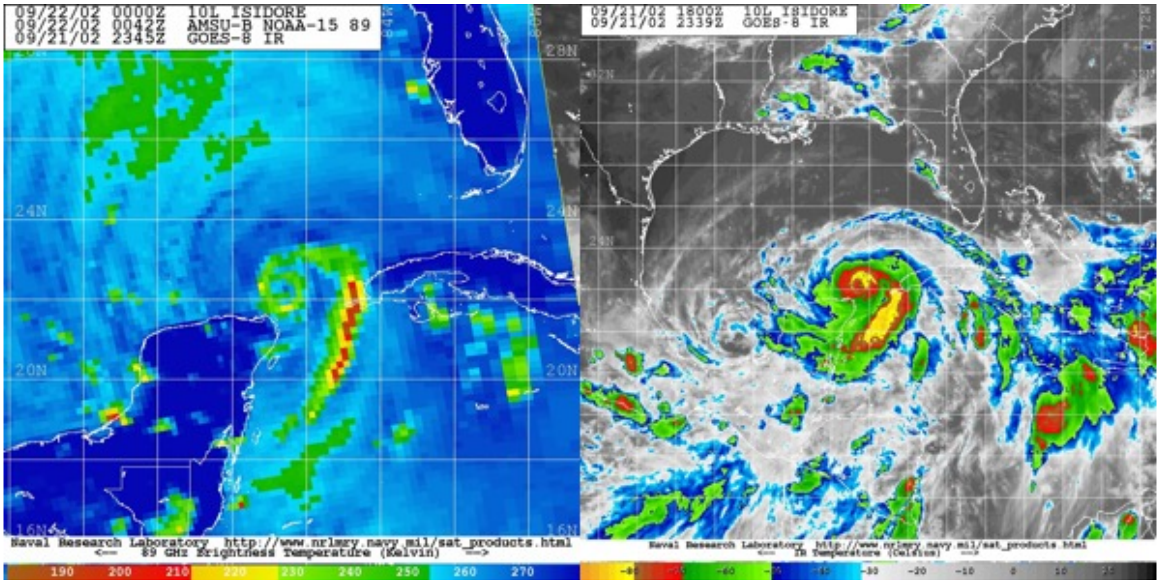

Figure 10: NOAA-15 AMSU-B 89 GHz (left) and GOES-8 infrared (right) imagery of Hurricane Isidore (2002) on 22 September at approximately 00 UTC (from NRL 2017).

the sensor, providing wind direction and velocity information derived from the ocean waves. This fraction of returned radiation is less susceptible to the scattering issues due to large raindrops that plague the higher microwave frequencies. Unfortunately, contamination occurs on the ocean surface due to splashing of raindrops and high wind variability in convective downdrafts. Thus, the active sensors are of limited use when wind speeds exceed 50 kt in rain bands and the eye wall of TCs. Figure 11 depicts Hurricane Jose (2017) wind vectors based on ASCAT data. The wind vectors near the TC center are black, indicating possible data contamination in the eye wall.

Methods for deriving wind information from T_B values, known as a gradient wind retrieval, exist in lieu of direct measurements. The T_B distribution is first determined at various vertical levels in the atmosphere. Next, the hydrostatic equation is integrated to determine the heights of these vertical levels. The gradient wind equation is then applied to determine the tangential wind speeds within the TC. Research to verify this method indicates the computed wind speeds often

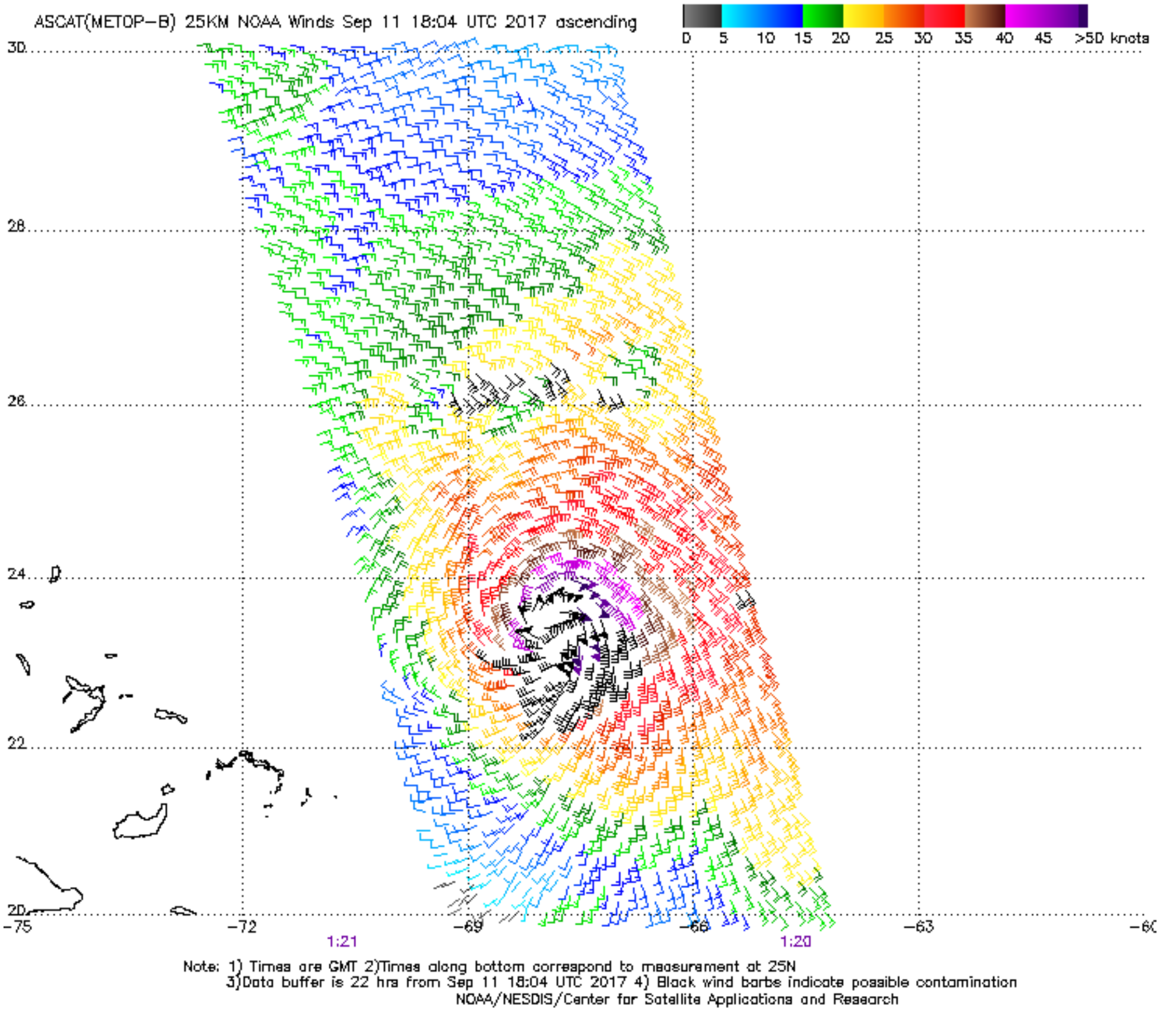

Figure 11: METOP-B ASCAT 5 GHz imagery of Hurricane Jose (2017) on 11 September at 1804 UTC (Center for Satellite Applications and Research 2017).

underestimate the actual recorded wind speeds. These errors are attributed to the signal attenuation of the EM radiation due to water vapor and rain drops, and the averaging that is applied over the width of the 45 km resolution cell (Kidder et al. 2000). This phenomenon causes low-level cold anomalies in the data, which can be adjusted by setting the temperature anomalies between the surface and 500 mb to 0. Figure 12 depicts tangential wind speeds in Hurricane Bonnie (1998) using both the unadjusted and adjusted AMSU gradient wind retrieval method compared to aircraft reconnaissance measured wind speeds. The adjusted AMSU gradient wind retrieval

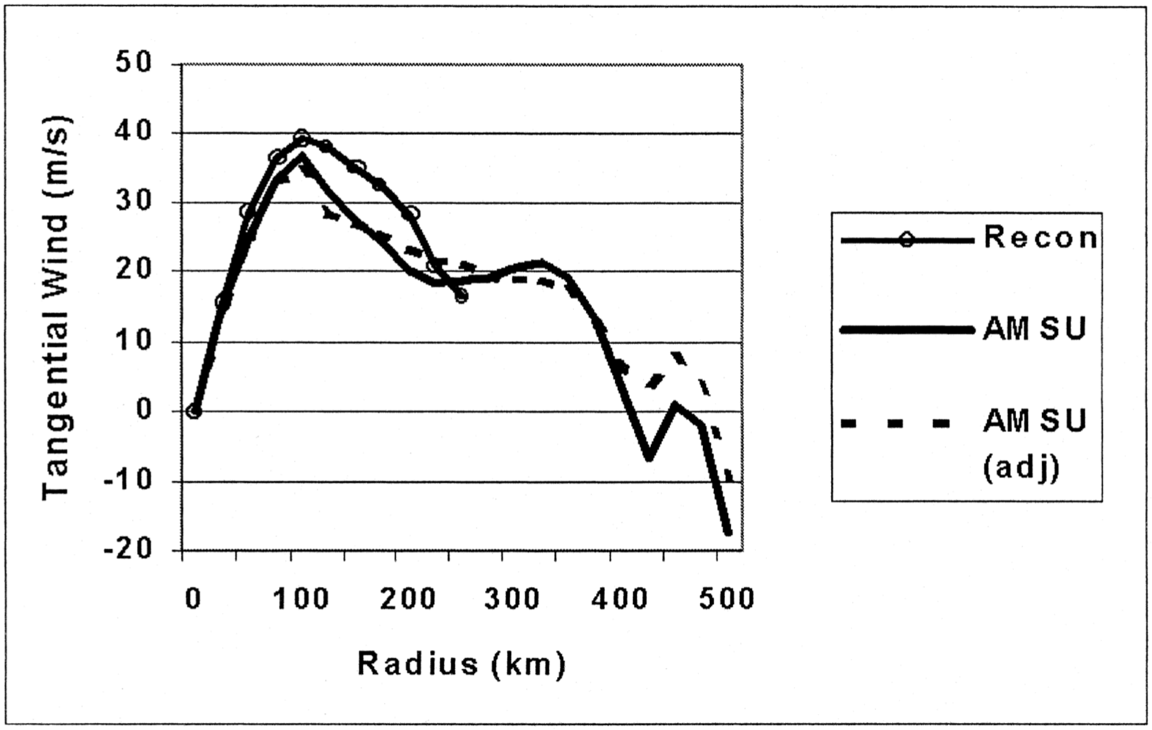

Figure 12: Azimuthally averaged tangential wind at 3 km for Hurricane Bonnie (1998) 25 August at 1200 UTC from the U.S. Air Force Reserve flight-level data and the AMSU gradient wind retrievals. The dashed line depicts the AMSU winds after the low-level cold anomalies were removed. No aircraft data were available for radii greater than 250 km (Kidder et al. 2000). ©American Meteorological Society. Used with permission.

method does little to correct the underestimation of wind speeds compared to aircraft measured wind speeds. Thus, this method is not particularly accurate for determining TC maximum wind intensity.

2.5.4 Techniques for TC Intensity Estimates

Through the early 1970s, universal-accepted, formal methods for characterizing TC intensity did not exist. This changed in 1975, when the Dvorak technique for estimating TC intensity using infrared satellite imagery was published. This method requires following a list of rules and procedures to analyze a TC's convective signature and cloud top temperature data by performing a formulaic data analysis, comparing these features to climatological patterns associated with TCs of various intensities, and determining trends relative to previous imagery for the same TC. Upon completing these tasks, a tropical number (T-number) is assigned to the TC (Dvorak 1975). The T-number ranges from T1 to T8, with intervals in half steps. Each number is related to minimum surface pressure in the TC on an empirical chart as depicted in Figure 13. An adjustment of one-half or one full T-number can be made by the analyst if the TC is changing rapidly. This final T-number after adjustment is defined as the current intensity (C.I.) number.

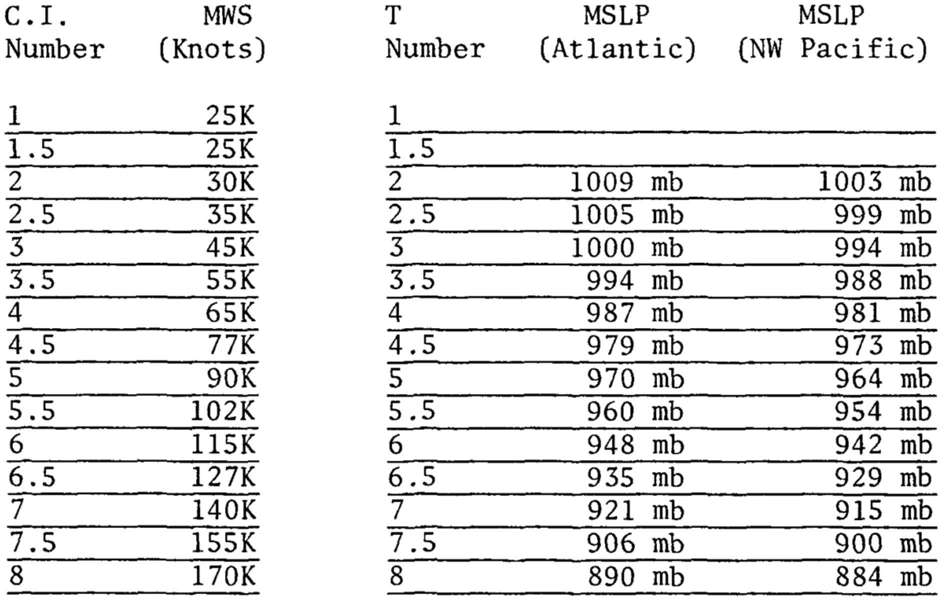

C.I. Number	MWS (Knots)
1	25K
1.5	25K
2	30K
2.5	35K
3	45K
3.5	55K
4	65K
4.5	77K
5	90K
5.5	102K
6	115K
6.5	127K
7	140K
7.5	155K
8	170K

T Number	MSLP (Atlantic)	MSLP (NW Pacific)
1		
1.5		
2	1009 mb	1003 mb
2.5	1005 mb	999 mb
3	1000 mb	994 mb
3.5	994 mb	988 mb
4	987 mb	981 mb
4.5	979 mb	973 mb
5	970 mb	964 mb
5.5	960 mb	954 mb
6	948 mb	942 mb
6.5	935 mb	929 mb
7	921 mb	915 mb
7.5	906 mb	900 mb
8	890 mb	884 mb

Figure 13: Empirical relationship between C.I. number, maximum wind speed (MWS), T-number, and MSLP (Dvorak 1975). ©American Meteorological Society. Used with permission.

The Dvorak technique was widely accepted by the tropical meteorology community, and a modernized version of it is used today globally by TC forecasting agencies such as the National Hurricane Center (NHC) and JTWC. Issues with the technique include subjectivity of the cloud signatures and manpower hours required to constantly apply it, to include time spent learning and mastering the nuances of the technique (Velden et al. 2006). An effort towards automation began in the mid 1980s, and evolved over the next two decades. In 2006, the current version of the method, now known as the Advanced Dvorak Technique (ADT), is fully automated in real-time. ADT does not attempt to mimic the old subjective technique through automated processes; rather, it uses a modernized version of digital infrared thresholds and rules, extending its capabilities far beyond the original method.

Attempts to create a method similar to ADT using microwave imagery have proven difficult. The primary limitations involve the poor resolution of microwave imagery compared to infrared imagery, and infrequent data sampling due to the polar orbiting nature of satellites with microwave sensors on board (Petty 2006). Polar sensors only sample a small portion of the earth with each pass, making constant monitoring and capturing rapid intensity changes nearly impossible.

Research on developing a Dvorak-like technique for microwave imagery began in the 1990s. Cecil and Zipser (1999) used the 85 GHz channel to highlight precipitation-sized ice particles associated with a strong updraft due to the large quantity of microwave EM radiation scattering that occurs at that frequency. The cold T_B values indicate both updraft strength and precipitation efficiency. To differentiate between cold T_B values caused by ice particles rather than ocean surface emissivity, an empirical algorithm is applied that weights the horizontal and vertical polarization, given as the polarization corrected temperature (PCT).

In Figure 14, TC maximum sustained wind is plotted as a function of average PCT over the TC center. The correlation coefficient is somewhat weak at -0.54, with NW Pacific basin TCs accounting for most of the outliers in the data. When the same TCs were analyzed 24 hours after the PCT computation, the correlation coefficient increased to -0.65, indicating the PCT value may be more useful for future TC intensity estimates rather than current intensity estimates. A temporal lag is theorized to exist between production of an ice scattering signature and the response of the TC intensity.

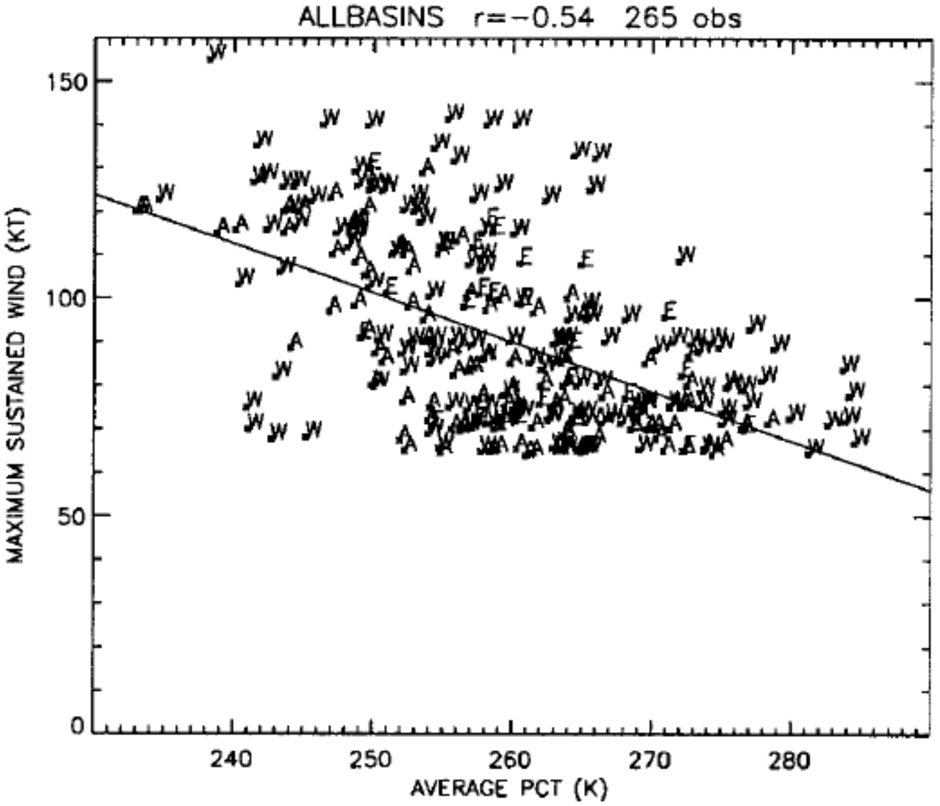

Figure 14: TC maximum sustained wind as a function of PCT at 85 GHz. Letters indicate ocean basin for each data point: A = Atlantic, E = NE Pacific, and W = NW Pacific (Cecil and Zipser 1999). ©American Meteorological Society. Used with permission.

2.5.5 Composite Averaging Techniques

One approach to identification of patterns in large data sets is to average some variable over the entire set. For satellite imagery, remotely sensed meteorological phenomena can be collectively summed and averaged to manually search for common patterns. Mapes et al. (2009) used this technique with infrared imagery data sets to identify patterns in tropical mesoscale convective systems (MCSs). Though a significant gain in temporal resolution is achieved, this averaging method can smear or scramble unique aspects of individual events. This effect can be mitigated by binning similar events. However, reducing the number of binned events creates noise in the averaged results. Care must be taken to maintain a sufficient sample size in binned categories without smearing out important aspects of the data. Figure 15 depicts cloud top temperature composites centered on tropical MCS events. The initiation for the tropical MCS is denoted as zero hour (0 h) with composite averages binned in three-hour groups before and after 0 h. Changes in the orientation and magnitude of contoured cloud top temperatures are visible as cloud tops cool leading up to the initiation of the MCS, and warm thereafter. This composite technique can be applied to microwave imagery T_B values to look for patterns in the data as TCs form, intensify, and weaken.

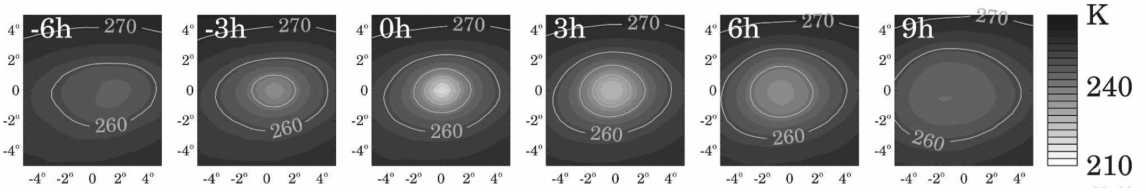

Figure 15: Composite fields near 10,393 MCS cloud systems, from (left) -6 hours to (right) +9 hours with respect to initial cold cloud appearance. Gray-scale shading depicts 10 x 10 patches of cloud-top temperature in K (Mapes et al. 2009). ©American Meteorological Society. Used with permission.

III. Methodology

3.1 Data Selection

Data for this research includes TCs in the Atlantic basin from 2004 to 2017. Sensors vary between the available years for imagery selection, the frequency used, and the native resolution of the microwave instrument. Composite averages of microwave T_B values for each sensor are generated for data analysis and cross-comparison between instruments. The Atlantic basin is selected due to the higher confidence in intensity estimates augmented by extensive aircraft reconnaissance data compared to all other ocean basins. Imagery is collected from SSMI/S, AMSR-E, AMSR2, and TMI. This imagery is publicly available from the NRL TC web page.

3.2 NRL TC Microwave Imagery Data

Microwave imagery rasters are generated by the NRL when passive microwave sensors aboard polar orbiting satellites pass over a TC. NRL does not offer file transfer protocol (FTP) access to their imagery, thus a download script is required to obtain the desired image files in an efficient manner. In this paper, the script searches the Atlantic basin subdirectories for all microwave rasters generated for each desired satellite sensor. The image files contain useful metadata embedded in the file name. The first half of the file name contains non-subjective TC information, while the latter half contains subjective information derived from a combination of human and automated data.

3.2.1 NRL Imagery Metadata

The first 13 characters in each file name provide the year, month, day, and time the data was captured, with date and time separated by a period. Next, the satellite name and frequency information are given as a string. For example, AMSR-E data reads *aqua1.89h*. This is the string the download script uses to isolate only the Aqua AMSR-E imagery, and this can be easily changed to match any satellite and frequency available in the NRL archive. Next, the TC number and name are provided. This information is useful for isolating a specific TC. This paper, however, composites all TCs for several microwave sensors. Thus, the TC number and name are useful only in detecting weak, unnamed TCs denoted as *invest* areas. Invest areas are disorganized and provide no value in a pattern recognition technique for TC intensity. A script searches for any TC names containing the string *invest* and deletes them.

The second half of the file name contains information derived from NHC *best track* data. First, wind intensity is given in knots rounded to the nearest integer ending in five or zero. For example, a TC with maximum sustained winds of 78 knots would be rounded up to 80 knots, but a TC with maximum sustained winds of 77 knots would be rounded down to 75 knots. This value is derived manually by the NHC forecasters on duty, and it is a subjective estimate. The wind intensity estimate is vital for this paper, and is used as truth for binning TC microwave imagery.

Second, the estimated minimum TC surface pressure is given in whole millibars (mb). Similar to wind intensity, this value is subjective and is estimated by NHC forecasters. Though TC intensity can be reasonably estimated using minimum surface pressure, this information is discarded in lieu of wind intensity as the basis for binning TC data. Next, the file name contains the estimated latitude and longitude of the TC center. The integer triplets represent latitude (longitude), and are followed by a

N (W) for north (west). The latitude (longitude) value is estimated to one tenth of a decimal degree. For example, 395N-631W corresponds to 39.5 degrees north, 63.1 degrees west. Once again, these values are estimated and manually set by an NHC forecaster.

Lastly, imagery file names beginning with the 2006 Atlantic hurricane season contain microwave coverage information as a percentage of the total image raster. Polar orbiting microwave sensors scan the earth's surface over a given swath width unique to each sensor. AMSR-E, for example, has a swath width of 1445 km. Thus, even if AMSR-E passes directly over a TC center, the entire raster only contains some fraction of microwave T_B information. The percent coverage in the file name is denoted "xxpc", where xx is the integer percentage value that corresponds to the fraction of microwave T_B data in the image. For example, "58pc" denotes a raster where 58 percent of the image contains T_B values. The percent coverage value is the basis of NRL imagery generation, where images are only made available if the value is greater than 25 percent. Figure 16 depicts a labeled sample of file name metadata for Hurricane Irma (2017).

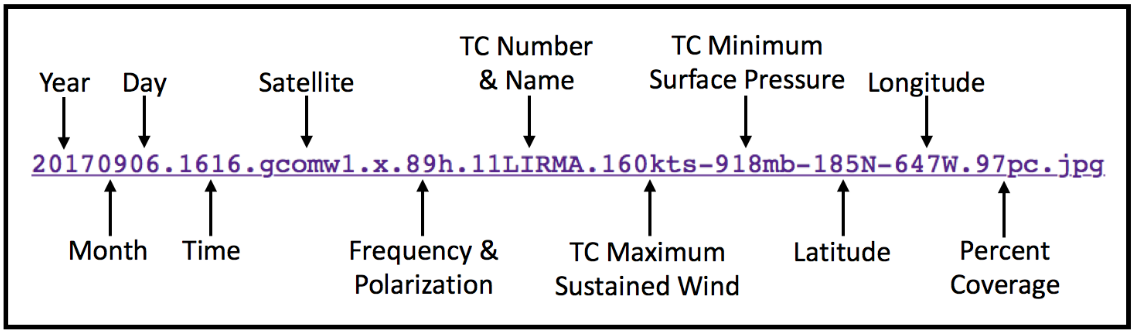

Figure 16: Sample of file name metadata for NRL rasters. This file name contains AMSR2 horizontally polarized 89 GHz imagery for Hurricane Irma (2017) from 6 September at 1616 UTC (from NRL 2017).

3.2.2 NRL Imagery Characteristics

NRL TC microwave imagery is centered on the estimated location of the TC low-level circulation. The location is subjective and is estimated by forecasters based on a combination of satellite imagery and aircraft reconnaissance data. The figure boundaries are approximately 1600 km in both zonal and meridional directions, and encompass an approximate 2,560,000 km^2 area . Derived microwave T_B values are represented as colored pixels, with a color scale depicted at the bottom of the figure. Figure 17 depicts cold T_B values of approximately 190 K as dark red in color, while warm values of approximately 250 K are green. The depicted microwave T_B data does not fill every pixel within the image file as the orbital path of the satellite rarely passes directly over the TC center. The remaining portion of the image consists of infrared satellite imagery to fill in the gaps in microwave data.

Header information in the upper left of the figure contains metadata similar to the file name information in the previous section. The top line contains the date, time, TC number, and TC name. The middle line contains the date, time, and sensor information for the microwave data depicted in the image, while the bottom line contains the same information for the infrared imagery that fills in gaps in microwave coverage. Geopolitical boundary and latitude-longitude grid overlays orient the user spatially to the TC data. Each pixel represents a 16 km^2 area that is 4 km along each side of the pixel. The actual resolution of the microwave instrument is often coarser than the 4 km resolution of each pixel, thus an interpolation and smoothing process is used in the generation of each image. SSMI is the only microwave sensor that does not use a 4 km resolution pixel or an interpolation and smoothing process. The result is data with a much coarser appearance than the other instruments used in this paper, masking important TC features. Thus, SSMI data is not used.

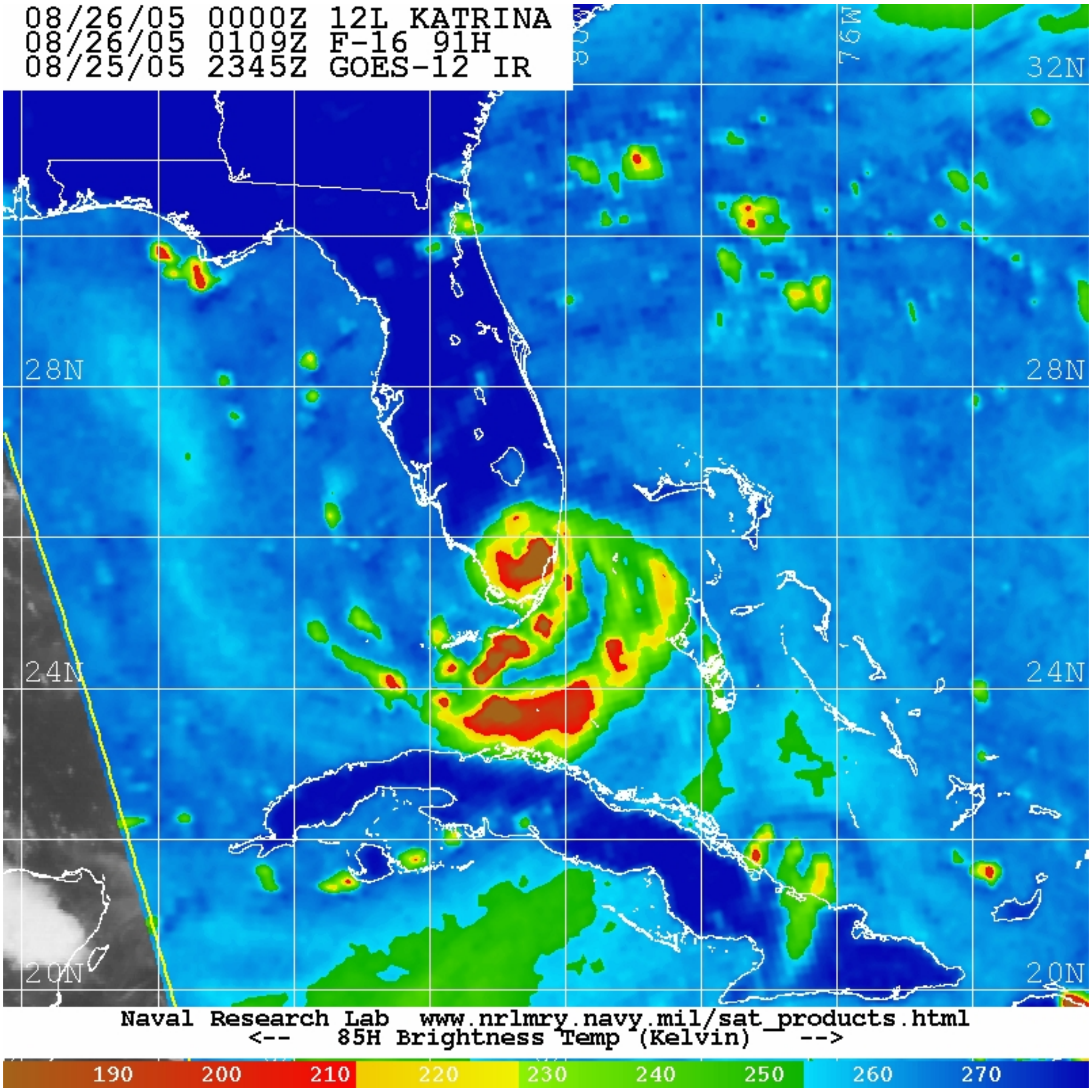

Figure 17: NRL SSMI/S horizontally polarized 91 GHz imagery for Hurricane Katrina (2005) from 26 August at 0109 UTC (from NRL 2017).

3.2.3 SSMI/S Imagery

NRL SSMI/S horizontally polarized 91 GHz imagery is available from August 2005 through the 2017 Atlantic hurricane season. All 11,988 images for this period were retrieved from the NRL database as Joint Photographic Experts Group (JPG) data, a compressed digital image format. SSMI/S has the greatest number of image samples for a single instrument compared to AMSR-E, AMSR2, and TMI. Though initially only available on DMSP F-16, it is currently aboard three DMSP satellites, whereas the other three sensors are aboard only one satellite each.

3.2.4 AMSR-E and AMSR2 Imagery

NRL AMSR-E horizontally polarized 89 GHz imagery is available from September 2003 until October 2011 when the sensor failed. A total of 2,132 images from June 2004 until October 2011 were retrieved from the NRL database as JPG data. Data before the 2004 Atlantic hurricane season does not contain metadata in the file name, thus it is omitted. AMSR2 replaced AMSR-E in June 2014, and imagery is available through the 2017 Atlantic Hurricane season. All 1235 images for this period are downloaded from the NRL database as JPG data. AMSR2 also uses the horizontally polarized 89 GHz channel, and only a minor change in resolution exists between the two sensors. Thus, data from both instruments is used together in the image compositing process to obtain a reasonable sample size of data.

3.2.5 TMI Imagery

NRL TMI horizontally polarized 85 GHz imagery is available from September 1998 through the 2014 Atlantic hurricane season. A total of 6,495 images from June 2004 through October 2014 were retrieved from the NRL database as JPG data. Data before the 2004 Atlantic hurricane season does not contain metadata in the file name, thus it is omitted. Table 4 summarizes the data used for each sensor.

Table 4: Microwave sensor, channel, period, and number of images collected.

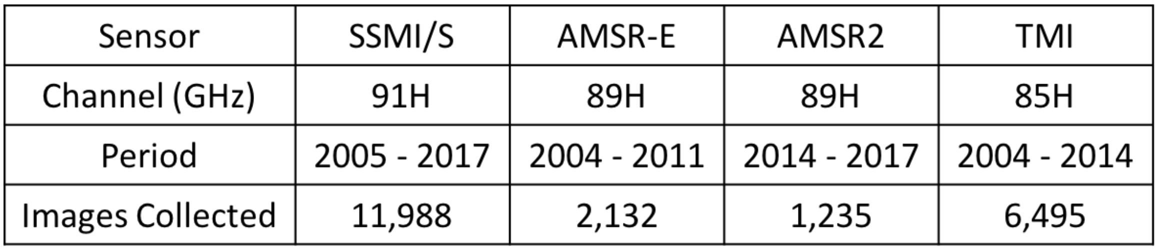

Sensor	SSMI/S	AMSR-E	AMSR2	TMI
Channel (GHz)	91H	89H	89H	85H
Period	2005 - 2017	2004 - 2011	2014 - 2017	2004 - 2014
Images Collected	11,988	2,132	1,235	6,495

3.3 Data Sorting

Not all of the retrieved microwave imagery is used in development of an intensity estimate technique for TCs. This paper will focus on stronger TCs that pose a significant threat to human life, assets, and resources. Thus, all imagery associated with TCs below Category 1 strength are discarded, as summarized in Table 5. The remaining imagery is sorted by TC category into a series of data bins. Separate analysis of each TC category depicts changes in the T_B pattern as the intensity varies. Fewer than 14 Category 4 images are available for each sensor. Additionally, all available Category 4 imagery have an estimated intensity of 135 knots, only two knots below the Category 5 threshold. Thus, the Category 4 and 5 imagery are binned together as one joint category. AMSR-E and AMSR2 images are also combined for each category to provide a greater sample size for composite averaging. Henceforth, the combined data from these two instruments will be simply referred to as AMSR. The number of images for each sensor by category is depicted in Table 6.

Table 5: Microwave sensor, number of images collected, discarded, and remaining.

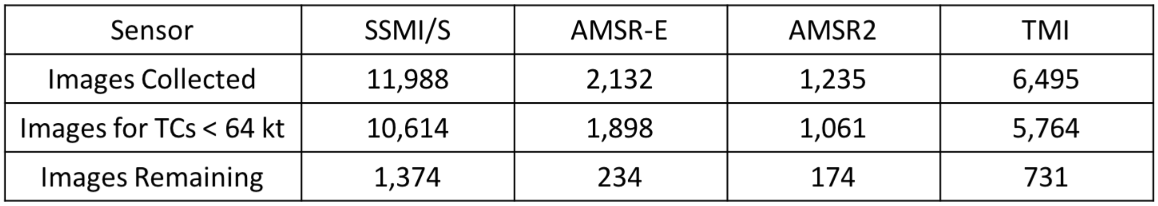

Sensor	SSMI/S	AMSR-E	AMSR2	TMI
Images Collected	11,988	2,132	1,235	6,495
Images for TCs < 64 kt	10,614	1,898	1,061	5,764
Images Remaining	1,374	234	174	731

Table 6: Number of microwave images for each sensor binned by category.

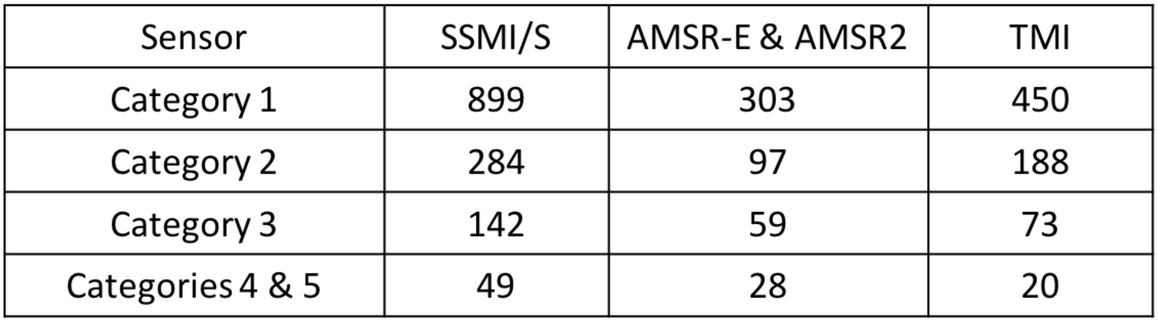

Sensor	SSMI/S	AMSR-E & AMSR2	TMI
Category 1	899	303	450
Category 2	284	97	188
Category 3	142	59	73
Categories 4 & 5	49	28	20

3.4 Image Processing

NRL imagery depicts T_B values from 180 K to 280 K. Colder T_B values (in red) indicate intense convection where absorption of rain drops and scattering of ice crystals is highest. Warmer T_B values (in blue) represent the background ocean temperature. Thus, the red, yellow, and green colored areas where T_B values are colder than 250 K contain useful information depicting TC structure and intensity of convection. Each pixel's color is a combination of three color elements, red (R), green (G), and blue (B), collectively referred to as RGB. These RGB values range from 0 to 255 (unitless). If all three RGB values are 0, the pixel is black. If they are all 255, the pixel is white.

Calculating a composite average of all three RGB values is problematic. The combination of the three variables will produce entirely different colors that mask intuitive pattern recognition of TC convective features. Thus, it is useful to isolate one color variable to mirror the single T_B variable represented by each pixel. As T_B values increase from 180 K to 250 K, linear scale adjustments are made such that the R value decreases linearly from 255 at 180 K to 0 at 250 K. Specifically, the original

R values are adjusted in the red portion of the color scale between 180 K and 213 K by the function

$$R = |R_0| - 395, \tag{6}$$

where R is the scaled red pixel value, $|R_0|$ is the absolute value of the original red pixel value, and 395 is an empirically determined constant. Similarly, the yellow portion of the color scale between 213 K and 228 K is adjusted by the function

$$R = |G_0| - 360, \tag{7}$$

where $|G_0|$ is the absolute value of the original green pixel value, and the green portion of the color scale between 228 K and 250 K is adjusted by the function

$$R = R_0 - 30. \tag{8}$$

The blue ocean background, white coastlines, gray and white infrared imagery, and white latitude and longitude grid lines represent noise in the context of this paper. Additionally, T_B values above 250 K are not conducive to identification of TC convective features. A filter sets R for these pixels to 0 to isolate the areas where T_B values are below 250 K. The resultant images contain pixels with only black and red colors, as depicted in Figure 18.

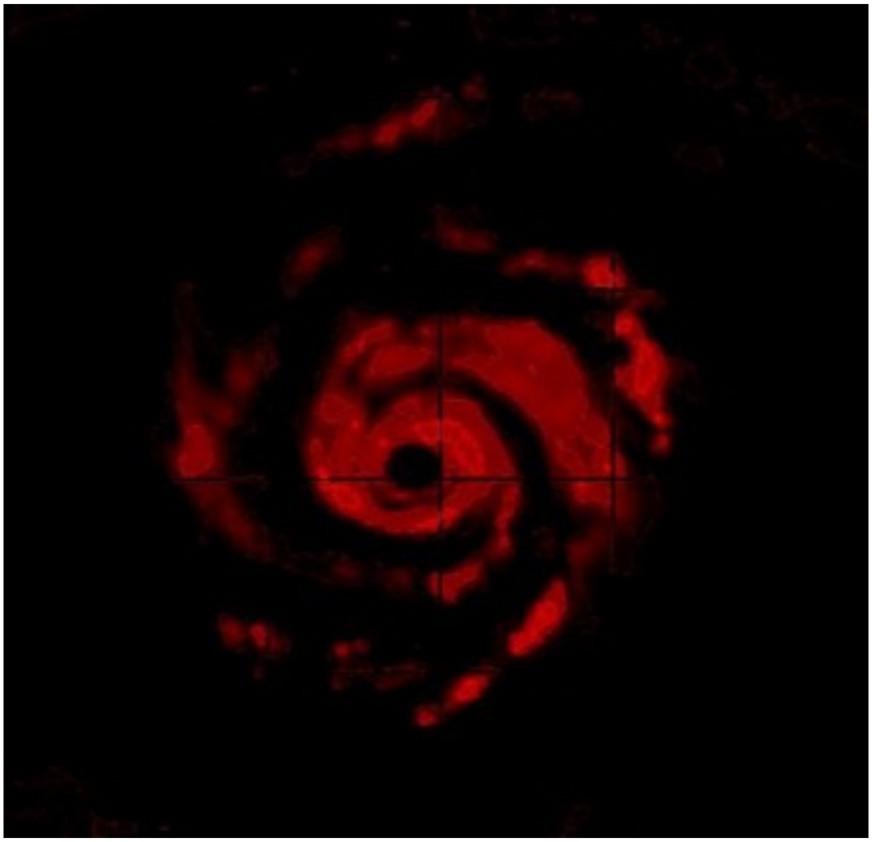

Figure 18: SSMI/S imagery of Hurricane Maria (2017) on 23 September at 2028 UTC after application of a linear scaling function for R values and a filter to isolate T_B values above 250 K (Adapted from NRL 2017).

3.5 Image Composite Averaging

A composite average of each pixel R value in the scaled and filtered TC microwave imagery collectively identifies spatial differences in the T_B data relative to the distance and azimuth from the TC center. Many pixels in each image are black in color and represent low values where R approaches zero. It is not useful to sum these values as part of the averaging process, as they do not depict convective processes within TCs. Thus, a threshold of $R > 10$ is set to include only pertinent data in the composite averaging process, henceforth referred to as *output*. Additionally, each *output* image depicts a 640,000 km^2 area 800 km in both zonal and meridional directions centered on the TCs. The location of the TC center is denoted with a white + symbol to easily identify the spatial relationship between convective features relative to the center. A sample *output* image for Category 2 TMI data is depicted in Figure 19.

3.5.1 T_B Conversion

TC microwave imagery is depicted in values of T_B by convention. Each output image initially contains only R values for each pixel, an unintuitive depiction for data analysis. Thus, these R values are scaled a second time to depict T_B average values at each pixel location in the output data. R decreases from 255 at 180 K to 0 at 250 K, a net change of 70 K over the 255 integer values of R. The function

$$T_B = -\frac{70}{255}R + 250, \tag{9}$$

scales R to T_B.

3.5.2 Microwave Frequency Variability

Differences in T_B value due to the variance in the three frequencies used is a consideration when building the new T_B scale. T_B values for 85, 89, and 91 GHz data vary due to the difference in ice particle scattering sensitivity. Figure 20 depicts this phenomena using Hurricane Wilma (2005) as an example. Though the images for both TMI and SSMI/S were taken only 39 minutes apart, TMI depicts T_B values ranging from 205 K to 220 K in the eye wall, whereas SSMI/S T_B values range from 195 K to 210 K in the same region. Additionally, SSMI/S depicts an additional area of moderate convection ($T_B < 230$ K) in a rain band south of the eye wall, whereas

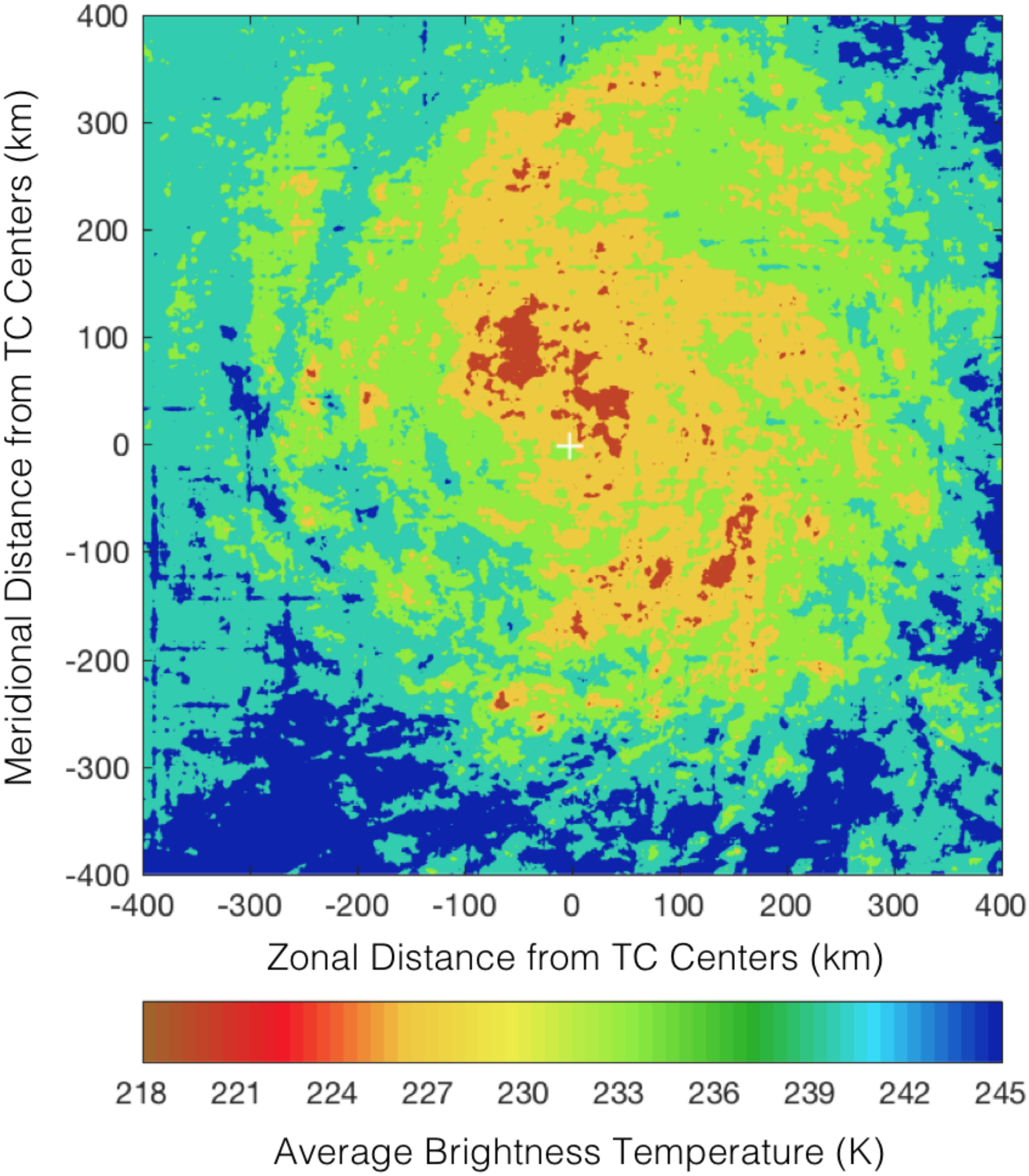

Figure 19: Composite average brightness temperature (K) for TMI Category 2 data. Location of TC center is denoted with a white + symbol.

TMI does not depict this feature at all. Thus, the new color scale for the *output* has different minimum and maximum values depending on the frequency of the sensor.

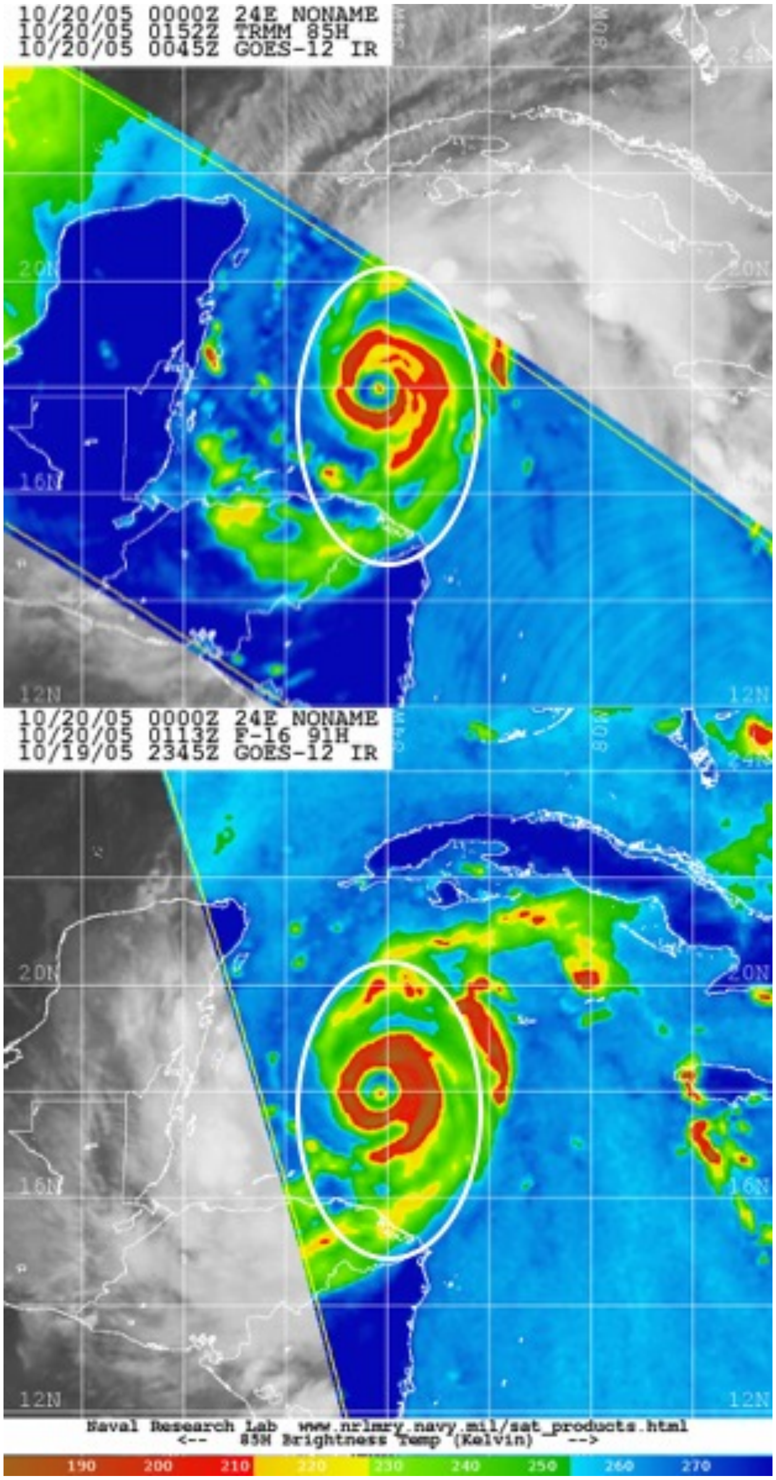

Figure 20: Comparison of T_B in 85 GHz and 91 GHz imagery for Hurricane Wilma (2005). TMI imagery (top) taken on 20 October at 0152 UTC depicts lower T_B values in convective features inside white oval compared to SSMI/S imagery (bottom) taken on 20 October at 0113 UTC (Adapted from NRL 2017).

3.5.3 T_B Normalization

The range of T_B values depicted by NRL imagery extends from 180 K to 280 K, whereas the *output* T_B values represent a much smaller range. Thus, a new T_B scale and color map is required to depict the more subtle changes in T_B necessary to identify notable TC convective features. The minimum and maximum T_B values are determined by calculating T_B values two standard deviations (σ) from the mean assuming a Gaussian distribution for each sensor (Bain and Engelhardt 1991). This method centers the new T_B scale around 95 percent of the data to eliminate extreme outliers on either end of the scale. Thus, the T_B mean values in the *output* are bounded by the 2.5th and 97.5th percentile of the data for each category. The bounds are given by the function

$$n = N * \frac{P}{100}, \tag{10}$$

where N is the total number of ordered T_B mean values in each *output* image, P is the desired percentile (2.5 for minimum bound, 97.5 for maximum bound), and n is the ordinal rank of the value corresponding to the input P. Tables 7 and 8 depict the minimum and maximum bounds calculated using Eq. (10) for each category by sensor. A mean minimum and maximum bound is calculated for each sensor to maintain a consistent T_B scale across the four *output* categories for each sensor. The consistent T_B scale is necessary to compare changes in the T_B pattern as the intensity varies.

Table 7: Minimum T_B (K) bounds used by sensor and category, with a sensor mean using all four categories. Values are rounded to the nearest integer.

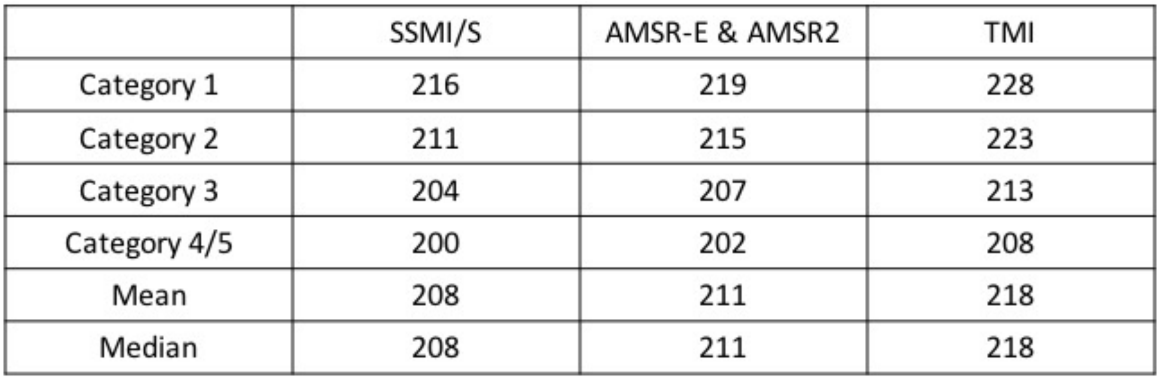

	SSMI/S	AMSR-E & AMSR2	TMI
Category 1	216	219	228
Category 2	211	215	223
Category 3	204	207	213
Category 4/5	200	202	208
Mean	208	211	218
Median	208	211	218

Table 8: As in Table 7, except for maximum T_B (K).

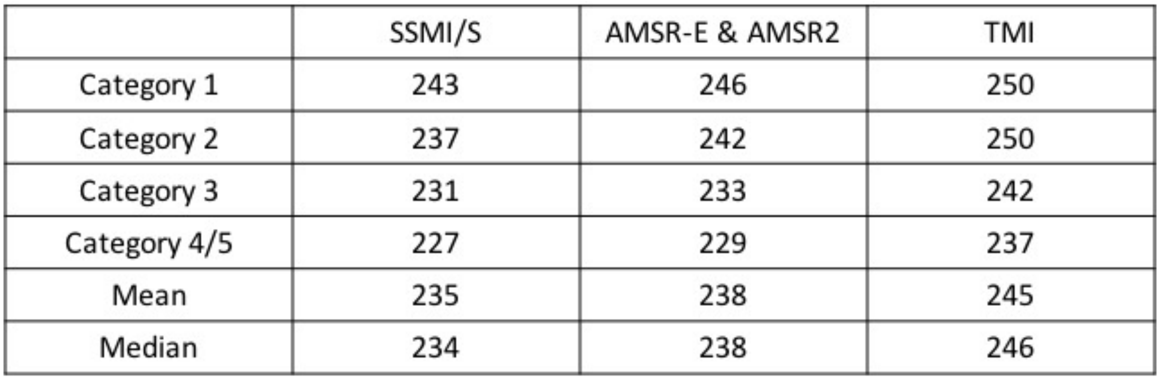

	SSMI/S	AMSR-E & AMSR2	TMI
Category 1	243	246	250
Category 2	237	242	250
Category 3	231	233	242
Category 4/5	227	229	237
Mean	235	238	245
Median	234	238	246

IV. Analysis and Results

4.1 Image Composite Analysis

Composite average T_B imagery binned by TC categories for SSMI/S, AMSR, and TMI are analyzed to identify T_B patterns, structure, and spatial relationships. Common features identified for each TC category will form the basis of a subjective technique for determining TC intensity. The analysis discussion in each section will initially focus on the structure in the inner portion of the TC, where the eye, inner eye wall, moat, and secondary eye wall are typically found. A widely accepted term and general distance from the TC center encompassing these features does not exist in meteorological literature. Thus, this inner portion of the TC will simply be referred to as the *core*, and this term will refer to features within 150 km of the TC center. Additionally, the standard mathematical division of the Cartesian grid into four quadrants will provide orientation to various features within the TC using cardinal directions. The northeast (NE), northwest (NW), southeast (SE), and southwest (SW) quadrants are depicted in Figure 21. The TC core is also depicted in Figure 21.

4.1.1 SSMI/S Category 1

SSMI/S Category 1 composite average T_B imagery is depicted in Figure 22. T_B values for the entire figure range from 214-230 K. A warmer T_B region of 220 K over the center point is surrounded by cooler T_B values ranging from 214-217 K. This warmer region is consistent with where the TC eye would typically be located in the individual SSMI/S Category 1 images. The cooler T_B regions extending 10-150 km radially from the center point are consistent with enhanced convection in the TC eye wall, and wrap around the eye in a band-like pattern. The convection in the

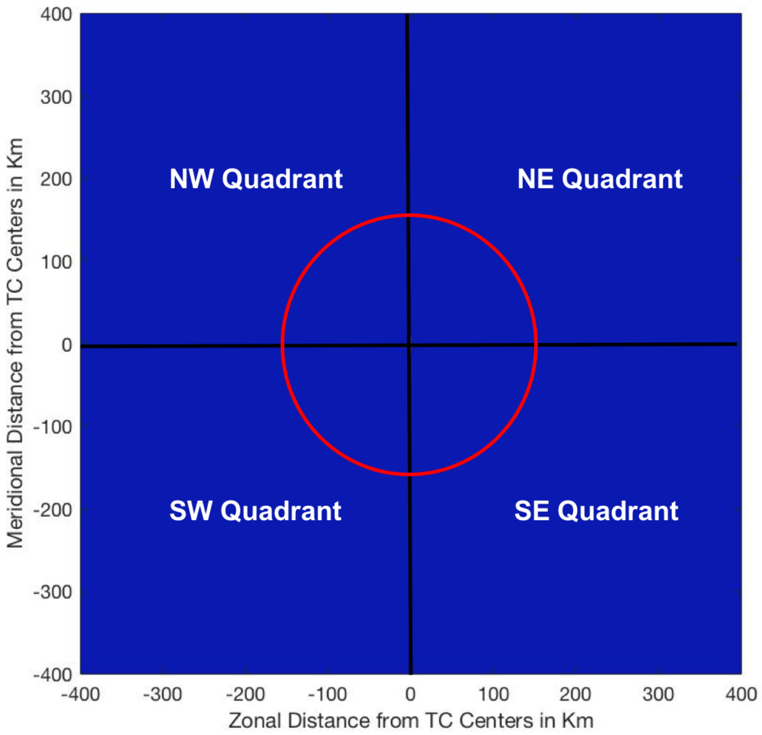

Figure 21: Location and title of the four TC quadrants relative to the TC center. The TC center is depicted where the two black axis lines cross. The red circle depicts the TC core, which extends from the TC center out radially to 150 km.

core of the TC structure is asymmetric, with most of the convection displaced to the north and east of the center point. The thickness of these relatively cooler T_B regions range from 25-50 km in the SW and SE quadrants, to 50-100 km in the NW and NE quadrants.

Overall, the T_B pattern is fairly asymmetric about the center point. Enhanced convective regions < 220 K depict a reasonable representation of the overall structure expected in a TC of Category 1 intensity. This overall structure extends radially to 300 km in the NE quadrant, 200 km in the NW quadrant, 100 km in the SW quadrant, and ranges from 150 km along the south axis of the SE quadrant to 300 km along the east axis of the SE quadrant.

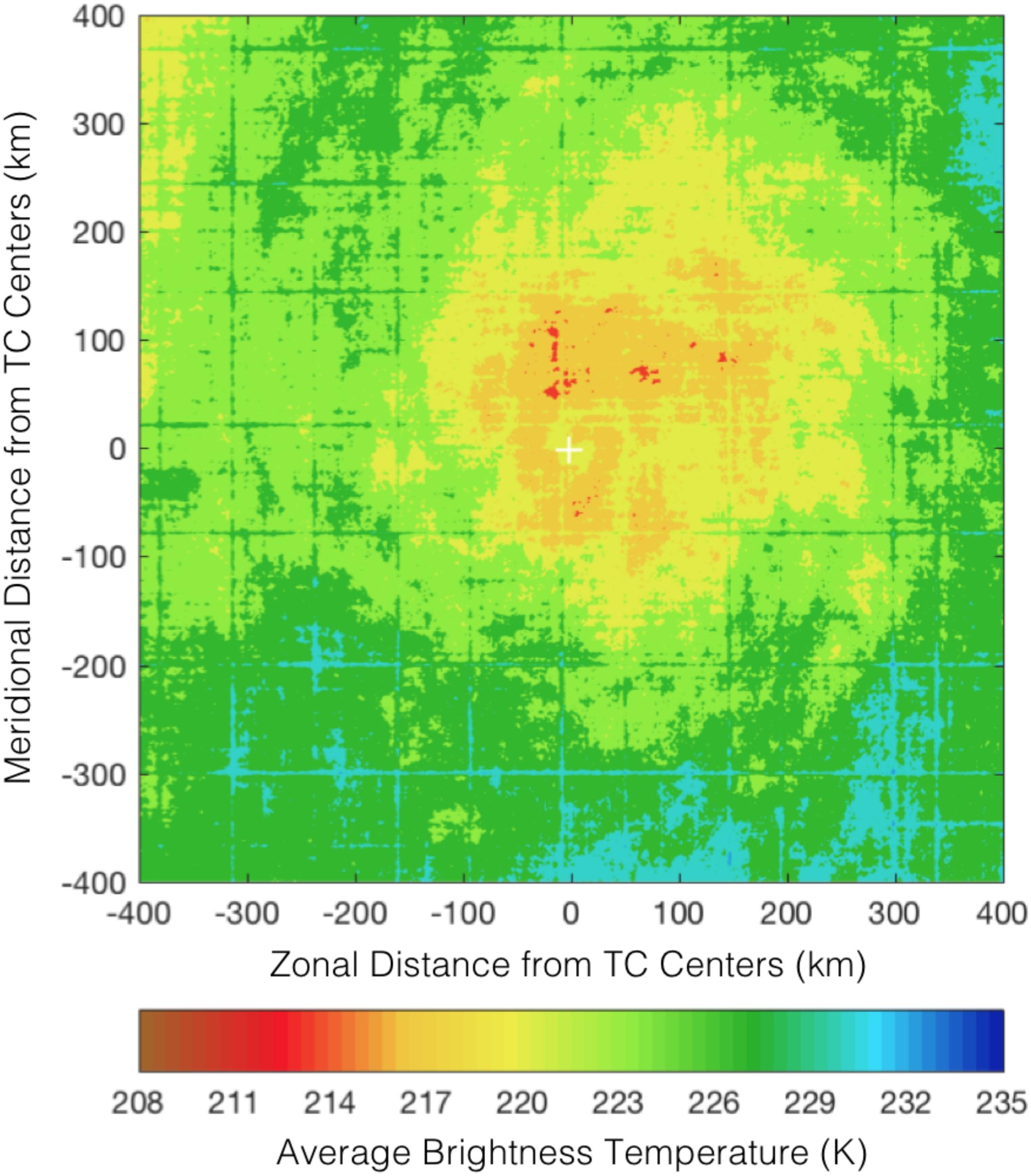

Figure 22: SSMI/S Category 1 composite average T_B. A white + symbol denotes the center point, which is the collective center of the individual TC images.

4.1.2 SSMI/S Category 2

SSMI/S Category 2 composite average T_B imagery is depicted in Figure 23. T_B values for the entire figure range from 208-235 K. Much cooler T_B values exist within 150 km of the center point compared to the SSMI/S Category 1 imagery, with values ranging from 208-214 K in the NE quadrant. T_B values range from 214-217 K in the NW quadrant of the TC core. In the SW quadrant, core values range from 214-217 K yet only extend radially up to 50 km. The SE quadrant core T_B values are cooler in comparison, ranging from 211-214 K radially out to 50 km, and from 214-217 K radially out to 100 km. The apparent band-like T_B pattern depicted in the Category 1 imagery is no longer evident, yet a greater extent of cooler T_B values associated with convection exists in the NW, SW, and SE quadrants. Additionally, small pockets of cool T_B values < 214 K are evident 200-300 km from the center point in the NW and NE quadrants. Overall, the TC is more axisymmetric than for Category 1, but the coolest T_B values exist in the NW and NE quadrants. Small pockets of T_B values < 220 K exist in the SW quadrant up to 100 km from the center point, which is double the extent in the SW quadrant of Category 1. Additionally, the extent of the < 220 K values range from 300-400 km in the NE quadrant, remain at 200 km in the NW quadrant, and decrease to 100-200 km in the SE quadrant. The decrease in eastward extent in the NE and SE quadrants may be evidence of a more organized structure in this portion of the TC, as the enhanced area of convection exists closer to the center point. In the Category 1 imagery, this convection was displaced well to the east of the center, which is not typical of a well-organized, axisymmetric TC.

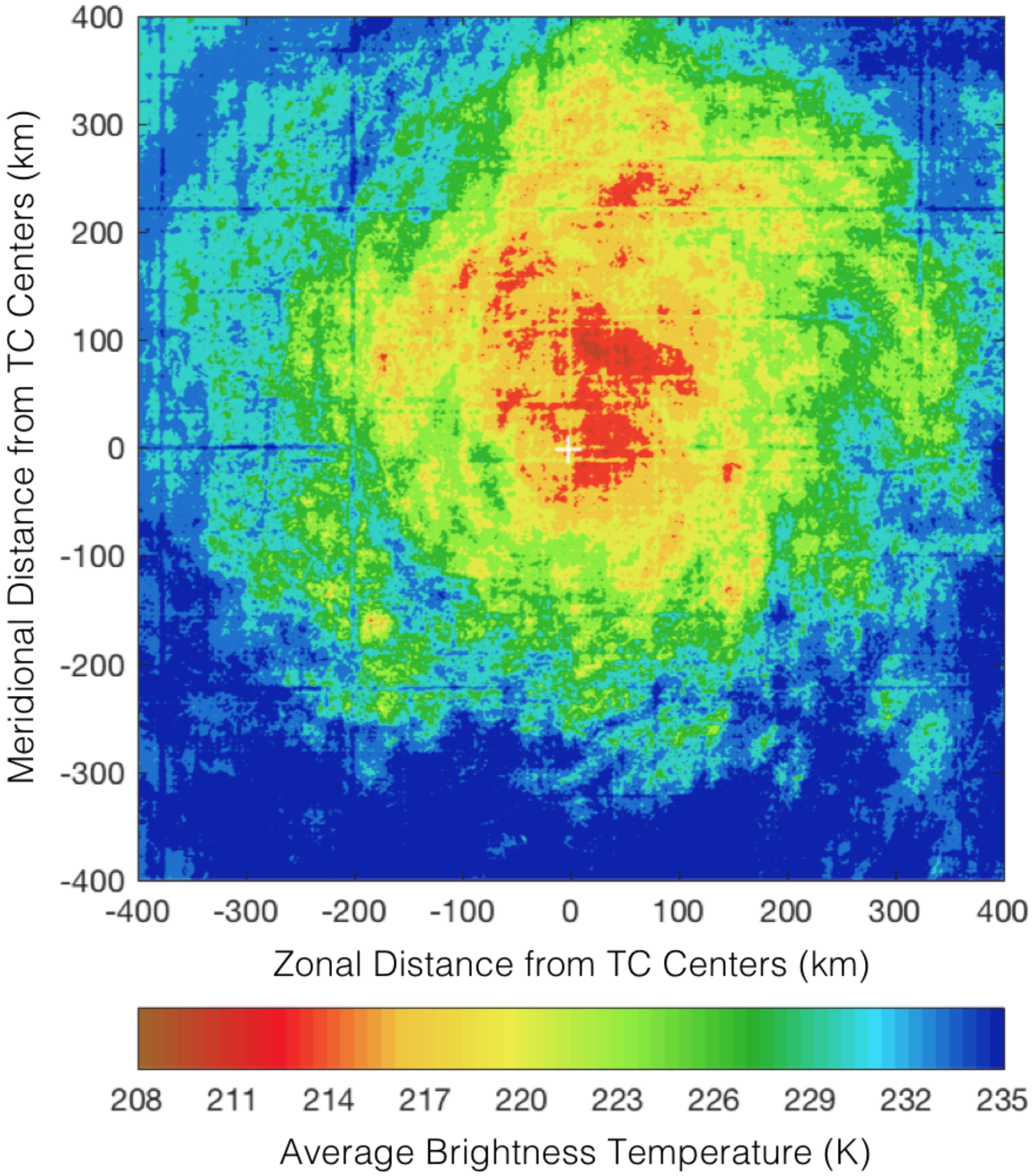

Figure 23: Composite average T_B as in Figure 22, except for SSMI/S Category 2.

4.1.3 SSMI/S Category 3

SSMI/S Category 3 composite average T_B imagery is depicted in Figure 24. T_B values for the entire figure range from 208-235 K. Within 150 km of the center point, T_B values 208-214 K decreased significantly from Category 2 to 50-100 km in radial extent in the NE quadrant. Very few areas with T_B values cooler than 217 K exist in the NW quadrant in the core region, but values ranging from 217-220 K extend out to 200 km. T_B values near 217 K extend to 100 km in the SW quadrant, and to 150 km in the SE quadrant. The total area of T_B values $<$ 214 K regardless of quadrant is significantly lower compared to the Category 2 imagery, whereas the axisymmetry of T_B values $<$ 220 K is noticeably increased. The T_B values $<$ 214 K show less bias to the NE quadrant, and exist primarily within 50 km of the center point. These phenomena are explained by the observed tendency that as TC intensity increases, axisymmetry typically increases. Additionally, the most intense convection exists closer to the TC center in the eye wall, which does not have a great radial extent for the TCs sampled in the composite imagery.

Overall, the TC axisymmetry has increased compared to Category 2, with T_B values $<$ 230 K extending to 300 km in all quadrants. Banding features are visible in all quadrants, with a noticeable outer band of $<$ 214 K T_B values in the NW quadrant 300 km from the center point. As the sample size of individual TC images decreases, an increased T_B gradient exists in the composite imagery. T_B values near 217 K in the core of all quadrants are surrounded by T_B values near 223 K, with no pixels corresponding to 220 K T_B values present. Similarly, these 223 K pixels are surrounded by T_B values near 230 K, with little transition of any values between 223 K and 230 K. This phenomenon is observed in all composite imagery with fewer than 200 samples of individual TC images.

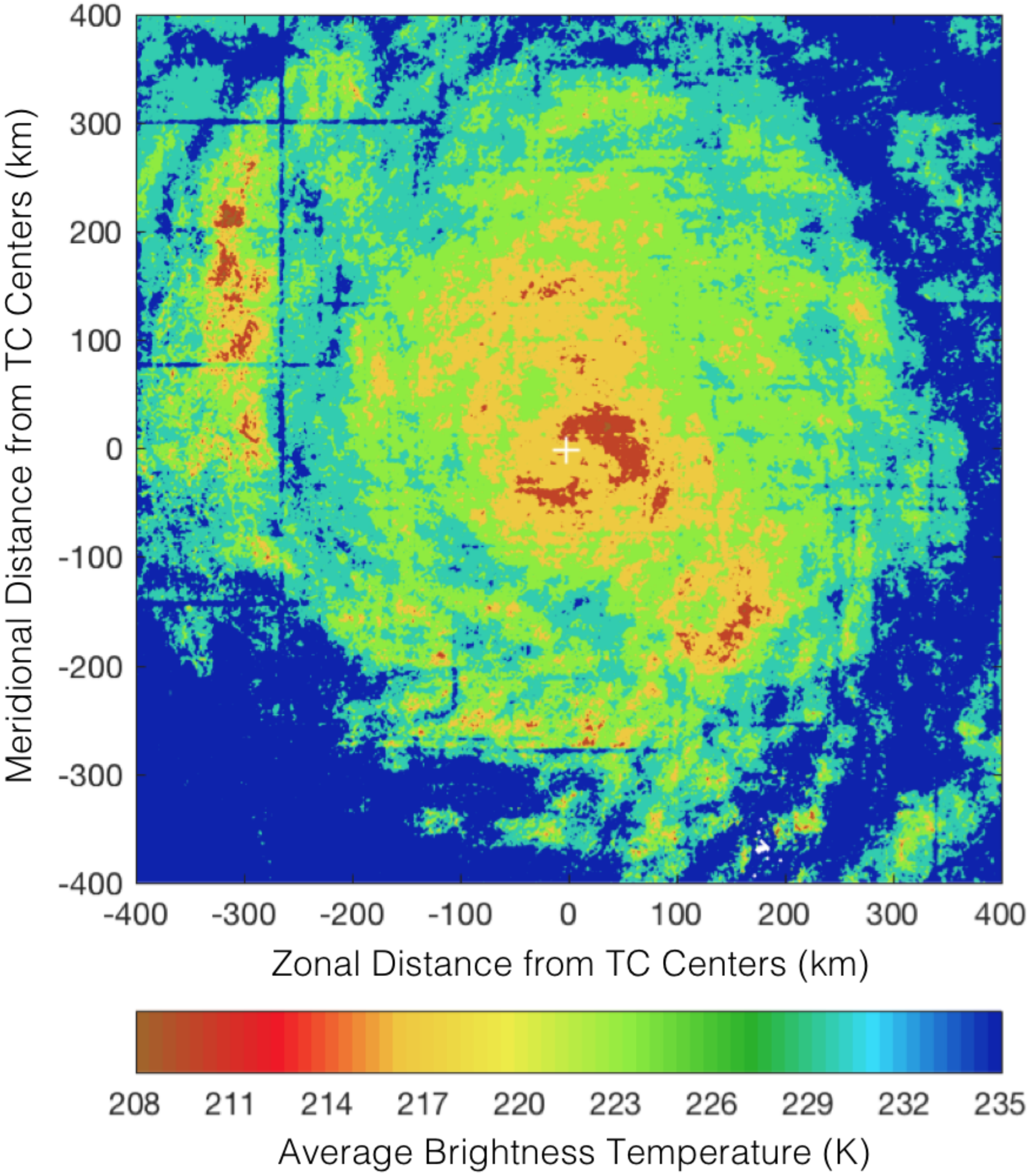

Figure 24: Composite average T_B as in Figure 22, except for SSMI/S Category 3.

4.1.4 SSMI/S Categories 4 and 5

SSMI/S Categories 4 and 5 composite average T_B imagery is depicted in Figure 25. T_B values for the entire figure range from 208-235 K, though areas where T_B was not < 250 K (for at least one individual TC image sample) are depicted in white. Within 150 km of the center point, T_B values 208-214 K increase in total surface area and radial extent in all but the NE quadrant compared to Category 3 imagery. The greatest radial extent for the coolest T_B values shifts from the NE quadrant to the NW and SW quadrants, which extend 100-150 km from the center point. The radial extent remains 50-100 km in the NE quadrant and approximately 100 km throughout the SE quadrant. T_B values < 220 K in the core are axisymmetric and extend 100-150 km in all four quadrants. The large mass of T_B values 208-214 K in the core clearly distinguishes Category 4 and 5 from Category 3 imagery and depicts the highly axisymmetric nature of strong convection in the core of particularly intense TCs.

Overall, the composite average TC remains axisymmetric similar to Category 3, with evident banding features in all four quadrants 150-400 km from the center point. Whereas T_B values < 214 K were confined within 50 km of the center point in Category 3 imagery, these values exist throughout all of the spiral rain bands depicted in the outer portion of the TC. A region of relatively little convection is evident in the NW and NE quadrants 200-300 km from the center point, separating the outer rain bands from the rest of the TC inner structure. The extremely intense nature of Category 4 and 5 TCs support strong convection in both the core and outer portions of the structure.

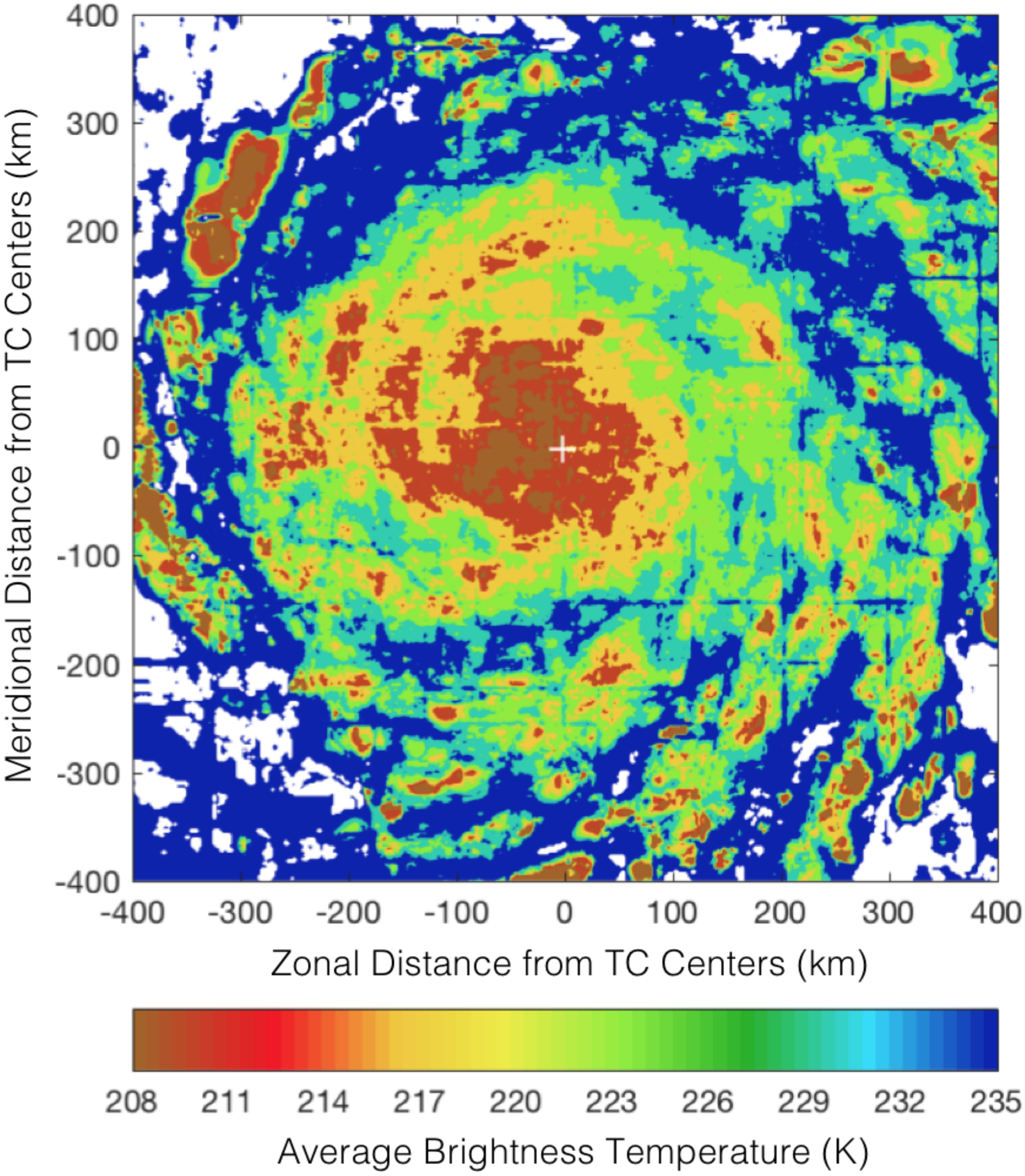

Figure 25: Composite average T_B as in Figure 22, except for SSMI/S Categories 4 and 5. White pixels in the image denote areas where $T_B > 250$K for the entire dataset and are thus removed prior to the composite average process.

4.1.5 AMSR Category 1

AMSR Category 1 composite average T_B imagery is depicted in Figure 26. T_B values for the entire figure range from 217-238 K. Small clusters of relatively cool T_B values 217-220 K exist in all four quadrants, extending radially 150-200 km from the center point. The greatest number of these clusters are in the NE quadrant, followed by decreasing totals in the SE, NW, and SW quadrants, respectively. No banding pattern is evident in the depicted T_B values. The limited areas of convection are asymmetric about the center point, with a bias to the NE quadrant. T_B values are generally < 226 K throughout the core in all four quadrants, though the radial extent of these values are < 100 km in the SW quadrant. Additionally, T_B values in the NE quadrant are generally < 223 K throughout the TC core.

Overall, the T_B pattern is asymmetric about the center point, with values < 226 K depicting the general structure of a Category 1 TC. This general structure extends radially out to 200 km in all quadrants, similar to the extent of the small T_B clusters 217-200 K. This structure is elliptical in shape due to the asymmetric nature of weaker TCs and has greater extent in meridional directions compared to zonal directions. No outer banding features are evident in any quadrant, and T_B values are > 226 K in the SW and SE quadrants, beyond 150 km from the center point. T_B values are also > 226 K in the NE and NW quadrants, beyond 250 km from the center point.

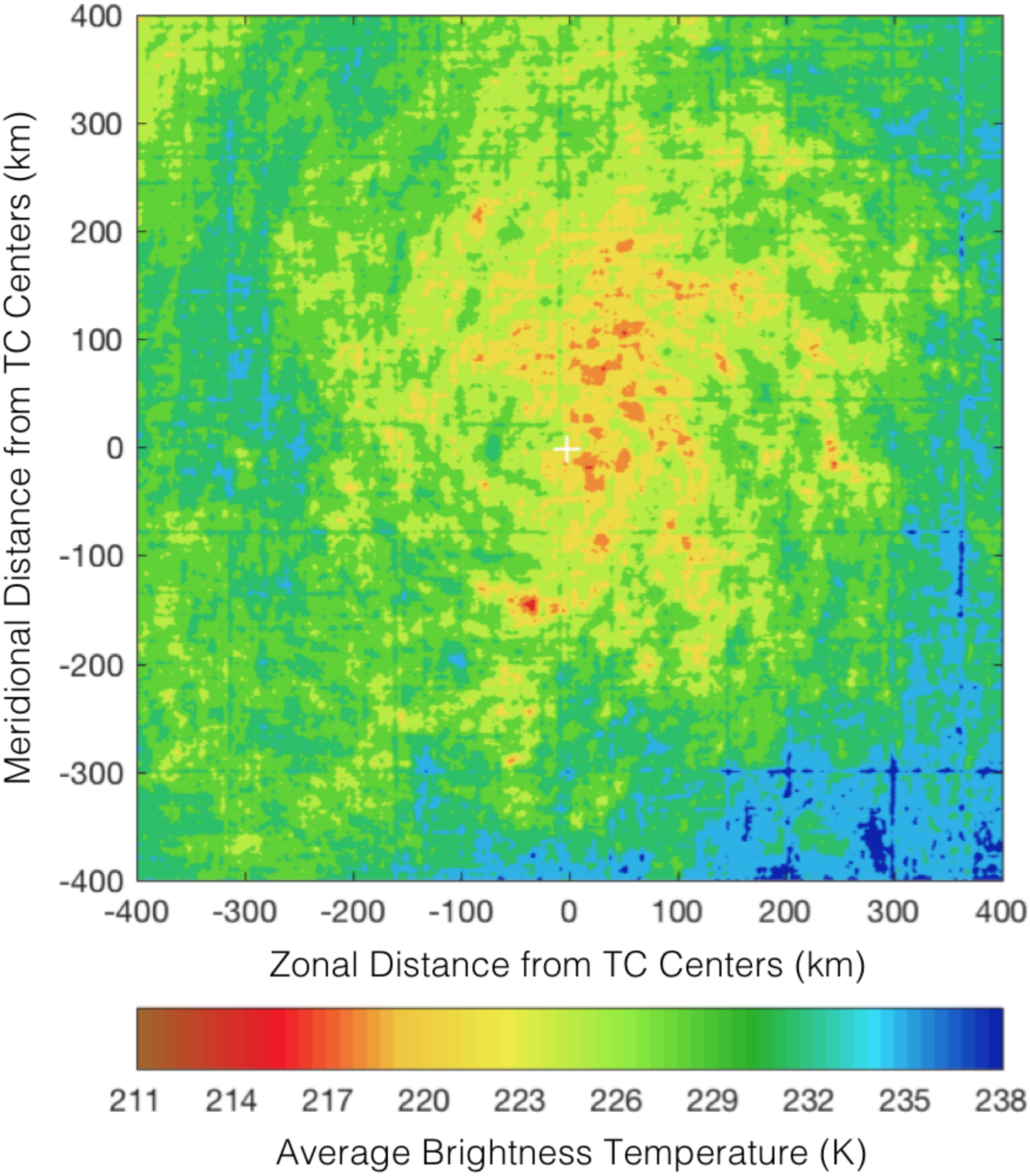

Figure 26: Composite average T_B as in Figure 22, except for AMSR Category 1.

4.1.6 AMSR Category 2

AMSR Category 2 composite average T_B imagery is depicted in Figure 27. T_B values for the entire figure range from 211-238 K, though areas where T_B was not < 238 K (for at least one individual TC image sample) are depicted in white. The small clusters of relatively cool T_B values 217-220 K in the Category 1 imagery are now oriented in band-like patterns. These banding features exist in the NE, NW, and SE quadrants, extending radially up to 200 km from the center point. The symmetry of these features about the center point is improved in the NW and SE quadrants compared to the Category 1 imagery. Outside the band-like features, T_B values remain generally < 226 K throughout the core in the NE, NW, and SE quadrants. T_B values in the SE quadrant are < 226 K within 100 km of the center point, with areas devoid of convection 100-150 km from the center point.

Overall, the T_B pattern depicts increased symmetry about the center point compared to Category 1. The shape of the general structure is similar to a comma, and the distribution of the convection is elliptical in nature. The primary mass of convection where T_B is < 226 K is oriented with greater meridional extent than zonal extent, similar to the Category 1 imagery. One exception where the zonal extent of convection is greater than the meridional extent exists in the SW quadrant. Two band-like features exist 150-300 km from the center point meridionally and 150-400 km from the center point zonally. This suggests that convection in the outer spiral rain bands is able to wrap around the TC in the SW quadrant, while an inhibitive factor prevents the same phenomenon from occurring in the core of the TC for this quadrant at Category 2 intensity. Band-like features are also evident in the NE, NW, and SE quadrants extending up to 300 km from the center point.

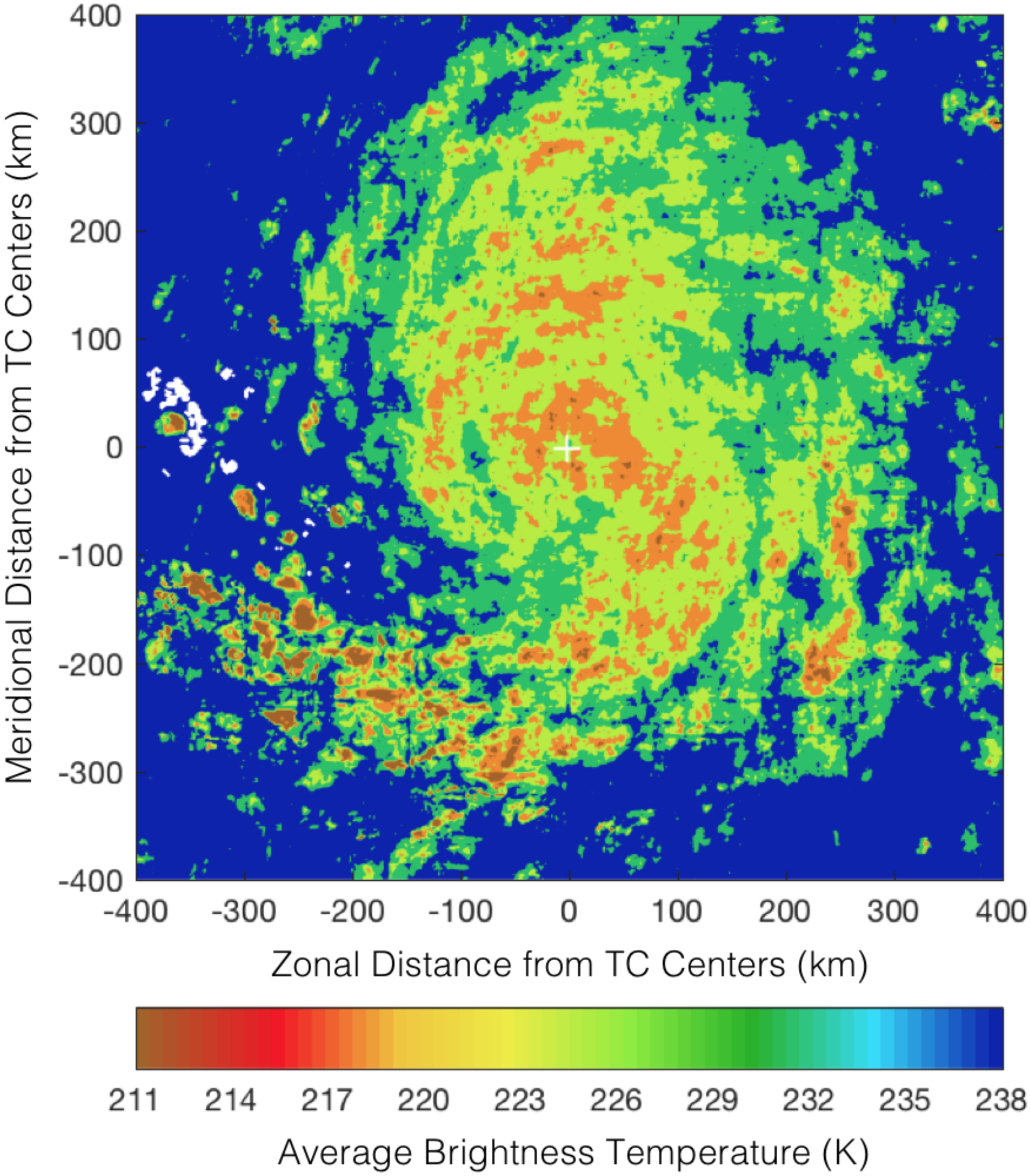

Figure 27: Composite average T_B as in Figure 22, except for AMSR Category 2. White pixels in the imagery denote areas where $T_B > 238$ K for the entire dataset and are thus removed prior to the composite average process.

4.1.7 AMSR Category 3

AMSR Category 3 composite average T_B imagery is depicted in Figure 28. T_B values for the entire figure range from 211-238 K, though areas where T_B was not $<$ 238 K (for at least one individual TC image sample) are depicted in white. The band-like features in the Category 2 imagery with T_B values 217-220 K are concentrated closer to one another in the core and contain clusters of T_B values 211-214 K within each band. The core rain bands exist predominantly in the SW and SE quadrants, extending up to 100 km from the center point. Portions of the band-like features exist in the NE quadrant, extending 50-100 km from the center point. The symmetry of the convection in the core is not greatly increased from the Category 2 imagery, but a much larger surface area of convection with $T_B < 220$ K exists within 100 km of the center point. This depicts the existence of a prevalent, intense eye wall feature, which is indicative of a stronger overall TC.

Overall, the T_B pattern depicts increased symmetry about the center point compared to Category 2. Both the comma shape and elongated nature of the convection in the meridional directions are no longer evident. Three or more spiral rain bands with intense convection, depicted by T_B values 211-214 K, exist in all four quadrants. The rain bands extend up to 400 km in the SW and SE quadrants, while extending up to 300 km in the NW and NE quadrants. The rain bands are oriented with greater zonal extent relative to the center point than meridional extent, with bands extending up to 400 km in zonal directions and up to 300 km in meridional directions. These bands are longer in length and more intense, with cooler T_B values compared to the Category 2 rain bands.

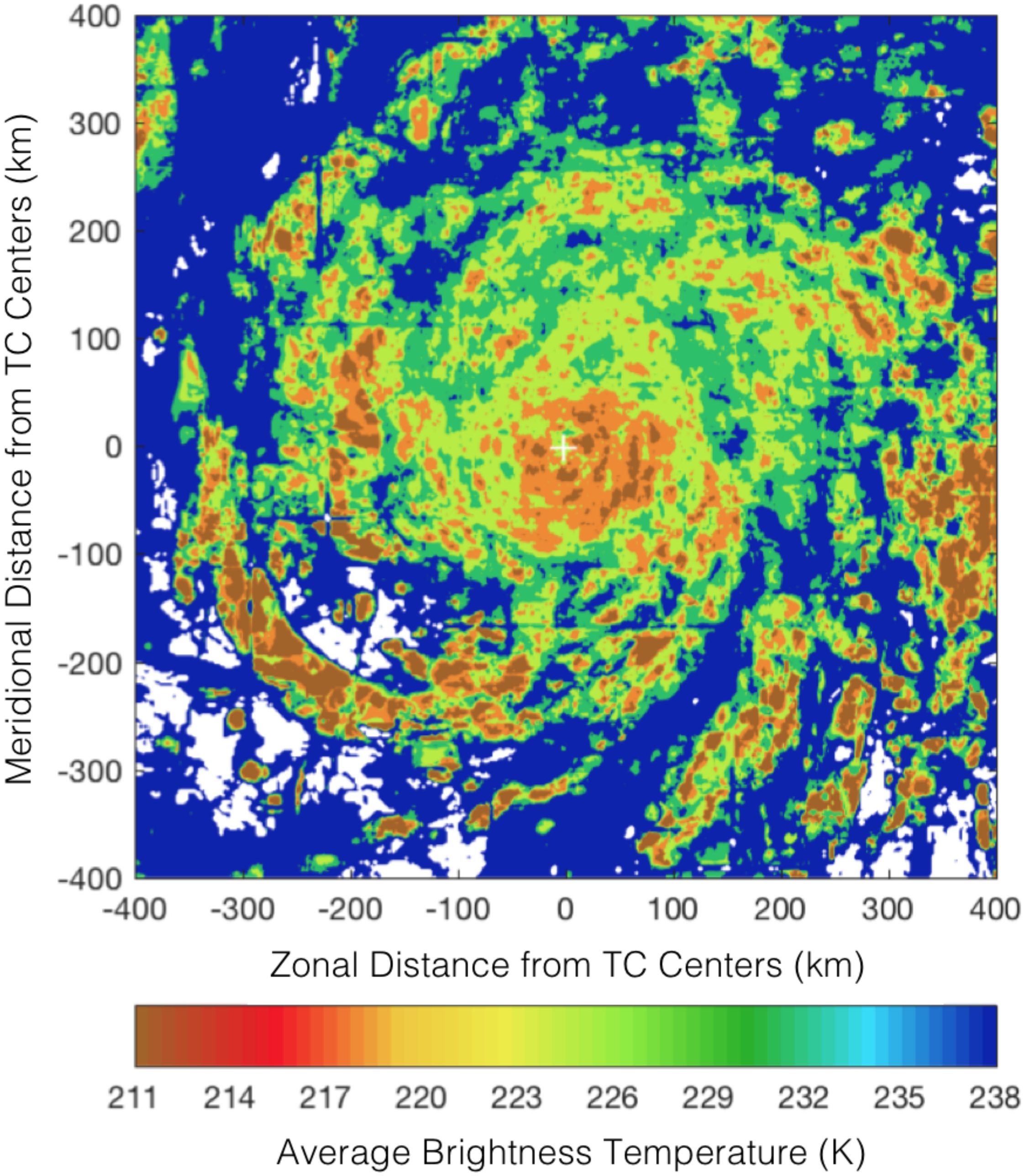

Figure 28: Composite average T_B as in Figure 22, except for AMSR Category 3. White pixels in the imagery denote areas where $T_B > 238$ K for the entire dataset and are thus removed prior to the composite average process.

4.1.8 AMSR Categories 4 and 5

AMSR Categories 4 and 5 composite average T_B imagery is depicted in Figure 29. T_B values for the entire figure range from 211-238 K, though areas where T_B was not $<$ 238 K (for at least one individual TC image sample) are depicted in white. Within 100 km of the center point, T_B values 211-214 K increase in total surface area and radial extent in all four quadrants compared to Category 3 imagery. The width of these cooler T_B values depicts a more intense and prominent eye wall compared to the category 3 imagery. This eye wall convection has the greatest radial extent in the NE and SE quadrants, extending up to 100 km from the center point, and may be influenced by SEF. This eye wall feature is less evident in the NW and SW quadrants, though T_B values 211-214 K exist in both quadrants and extend up to 50 km from the center point. The axisymmetry of this eye wall convection is increased from the Category 3 imagery, though a greater NE bias in the distribution is evident.

Overall, the T_B pattern depicts axisymmetry of convection similar to the Category 3 imagery. The outer spiral rain bands are less defined than the Category 3 imagery, though both the amount and width of the intense 211 K convection has increased. This convection extends up to 300 km in the SW, NW, and NE quadrants, while it extends up to 400 km in the SE quadrant. The distribution of the outer rain band convection is no longer oriented with greater extent in either the zonal or meridional directions, though the extent is greater in the eastern half of the imagery than the western half, and the extent is greater in the southern half of the imagery than the northern half.

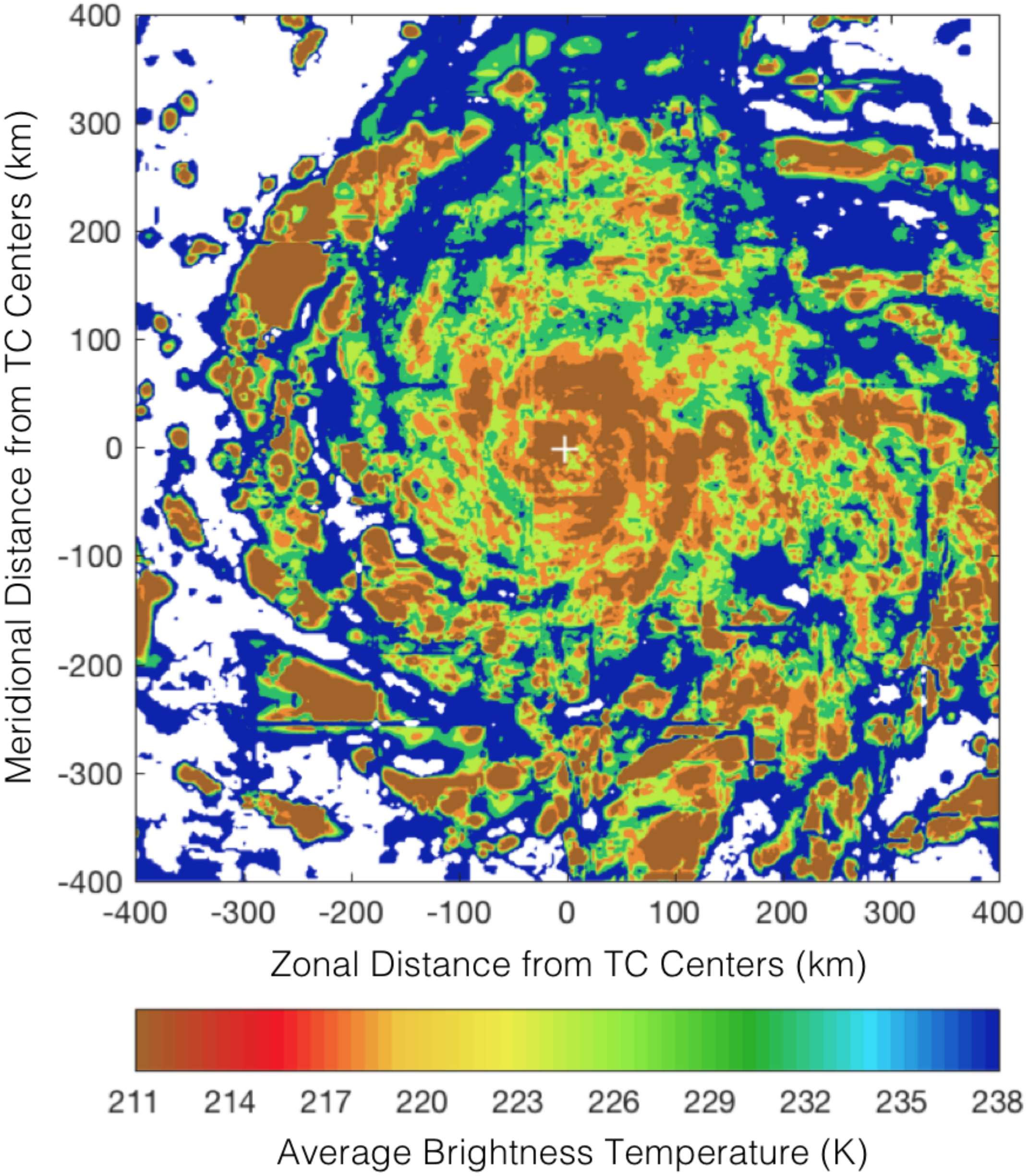

Figure 29: Composite average T_B as in Figure 22, except for AMSR Categories 4 and 5. White pixels in the imagery denote areas where $T_B > 238$ K for the entire dataset and are thus removed prior to the composite average process.

4.1.9 TMI Category 1

TMI Category 1 composite average T_B imagery is depicted in Figure 30. T_B values for the entire figure range from 221-245 K. In the core, clusters of convection with T_B values 221-224 K are embedded within a larger, broader area of convection with T_B values 227-230 K in the NW, NE, and SE quadrants. Additionally, this convection extends 150-200 km from the center point in the NE and SE quadrants, while extending 100-150 km from the center point in the NW quadrant. A weak banding pattern is somewhat evident as convection wraps around the center point, yet the organization within the core is not axisymmetric. A small area of T_B values 230-233 K exists in the SW quadrant, yet this quadrant is relatively devoid of convection compared to the other three quadrants. The NE quadrant contains the greatest surface area of convection, followed by the SE, NW, and SW quadrants, respectively.

Overall, the T_B pattern is asymmetric about the center point, with most of the convection to the north and east of the center point. T_B values < 230 K depict the general structure of a Category 1 TC, with this structure extending radially out 200-250 km in the NW, NE, and SE quadrants. Additionally, the radial extent is greatest in the NE quadrant, which is commonplace in weak, asymmetric TCs. No outer banding features are evident in any quadrant. T_B values are warmest in the SW quadrant, with a curved area of T_B values > 242 K located 200-300 km from the center point.

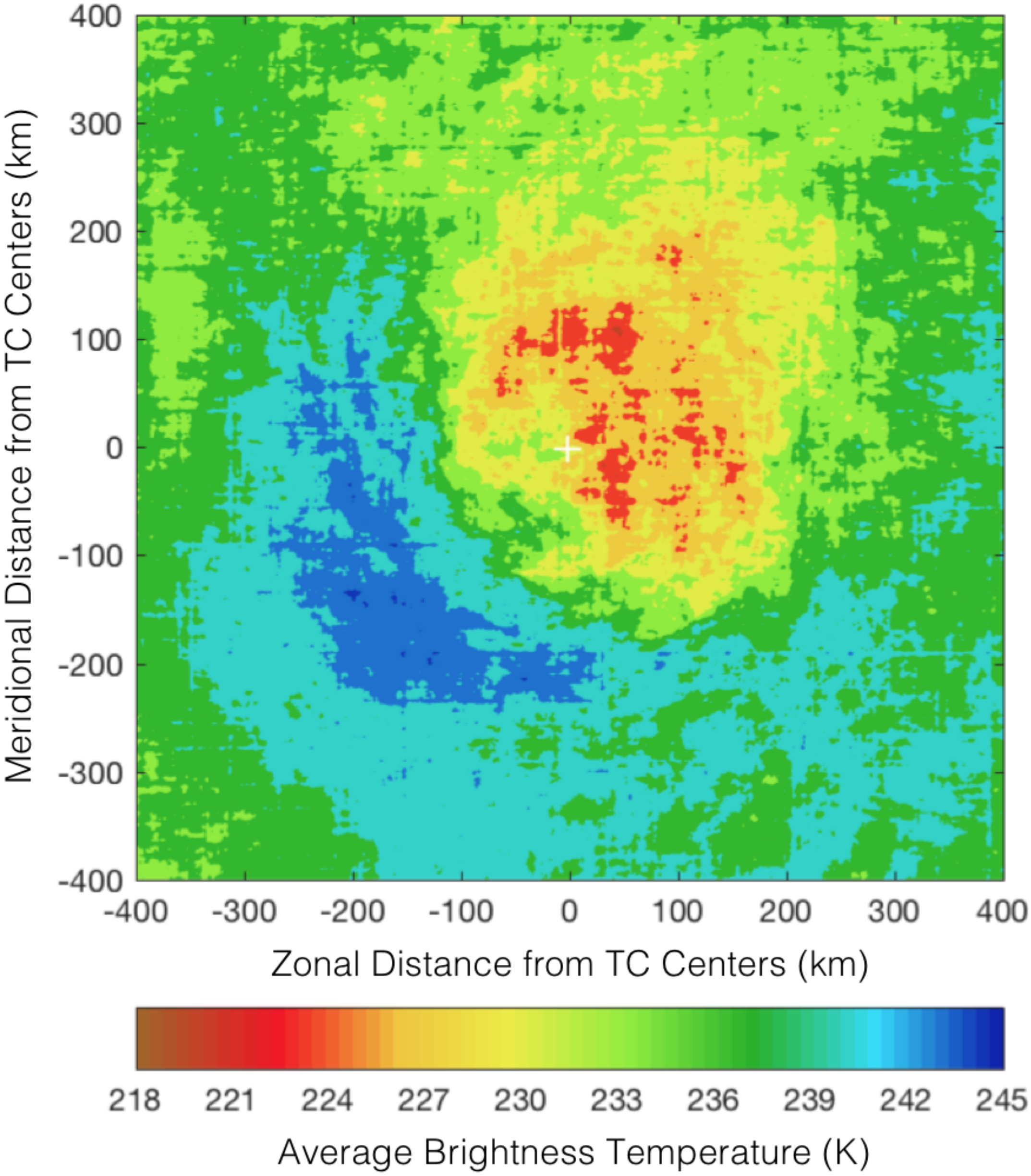

Figure 30: Composite average T_B as in Figure 22, except for TMI Category 1.

4.1.10 TMI Category 2

TMI Category 2 composite average T_B imagery is depicted in Figure 31. T_B values for the entire figure range from 221-245 K. Similar to the Category 1 imagery, the core depicts clusters of convection with T_B values 221-224 K embedded within a large, broad area of convection with T_B values 227-230 K in the NW, NE, and SE quadrants. Additionally, the greatest surface area with the most intense convection has shifted from the NE quadrant to the NW quadrant. This convection extends 100-150 km from the center point in the NW, NE, and SE quadrants. No banding features are evident in the inner core, yet banding does exist 100-150 km from the center point in the SE quadrant. The SW quadrant is still mostly devoid of convection, though T_B values 227-230 K are evident within 50 km of the center point. The axisymmetry of the core convection is slightly increased from the Category 1 imagery, but is still mostly displaced to the north and east of the center point.

Overall, the T_B pattern depicts slightly increased axisymmetry about the center point, as more convection has shifted west of the center in the NW quadrant. Banding features are evident in the outer portion of the TC in the NW, NE, and SE quadrants. These bands extend radially up to 300 km from the center point in the NW quadrant, 350 km from the center point in the NE quadrant, and 200 km from the center point in the SE quadrant. The SW quadrant depicts scattered weak convection with T_B values 230-233 K up to 300 km from the center point, yet is still mostly devoid of T_B values < 227 K.

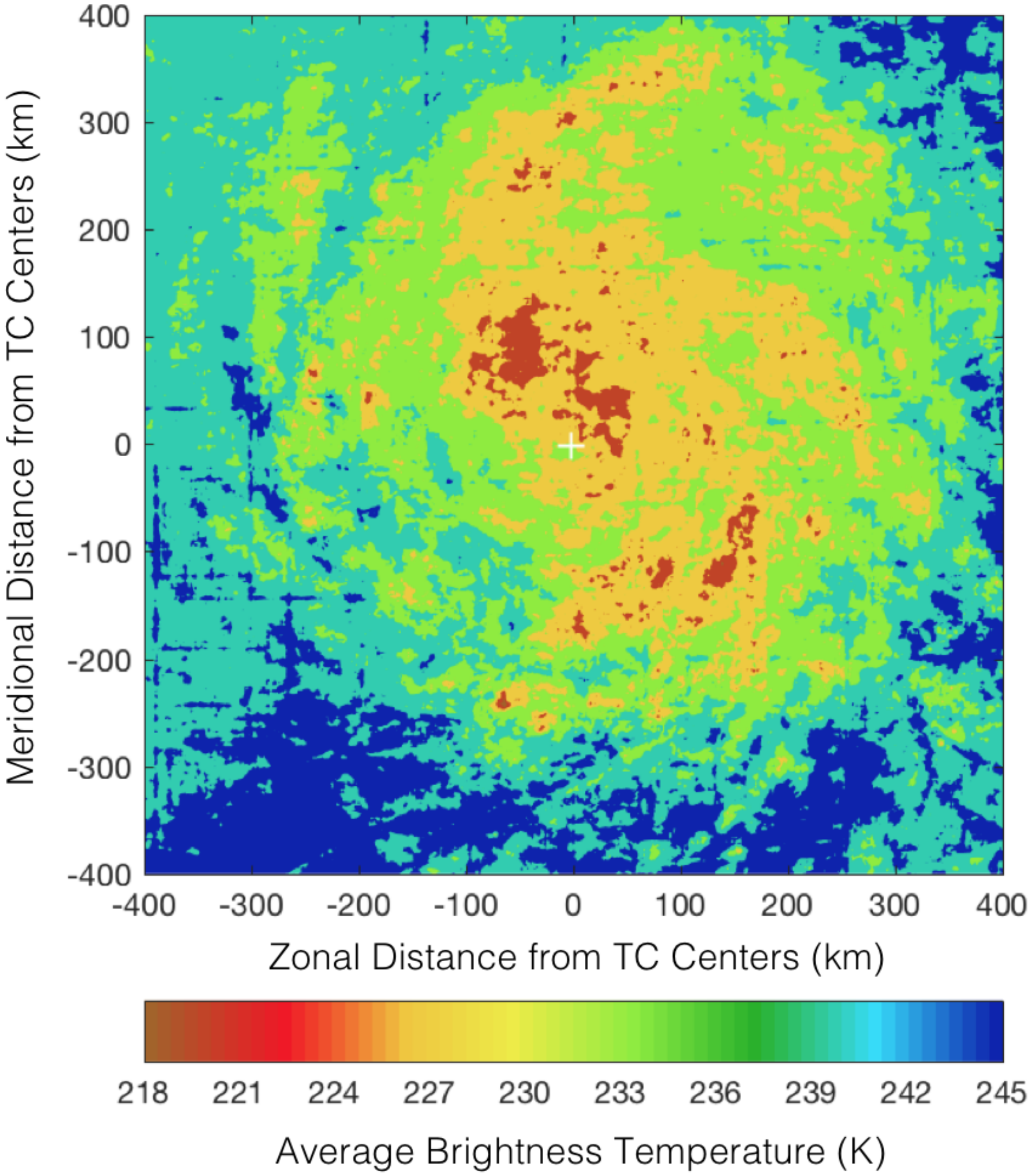

Figure 31: Composite average T_B as in Figure 22, except for TMI Category 2.

4.1.11 TMI Category 3

TMI Category 3 composite average T_B imagery is depicted in Figure 32. T_B values for the entire figure range from 218-245 K, though areas where T_B was not $<$ 245 K (for at least one individual TC image sample) are depicted in white. The core depicts significantly more convection than the Category 2 imagery, both in total surface area and intensity of T_B values. The axisymmetry of the core convection is dramatically increased from the Category 2 imagery, as bands of convection with T_B values 218-221 K are evident and extend radially out to 150 km in all four quadrants. Intense, concentric, and continuous bands depict the eye wall, and this signature is evident in all four quadrants within 50 km of the center point. The SE quadrant contains the greatest surface area of the coolest T_B values and thus contains the strongest convection relative to the other three quadrants.

Overall, the T_B pattern depicts increased axisymmetry about the center point, though banding features do not extend further outward than 150 km in the SW quadrant. Outer rain bands extend radially out to 400 km from the center point in the NW quadrant, 350 km in the NE quadrant, and 400 km in the SE quadrant. These spiral rain bands are less organized in the SE and NE quadrants compared to the NW quadrant, as the convection is discontinuous in the former two quadrants. The structure of the TC is slightly elliptical in nature. Rain bands extend in both meridional directions 350-400 km from the center point, while they extend in both zonal directions only 200-250 km from the center point.

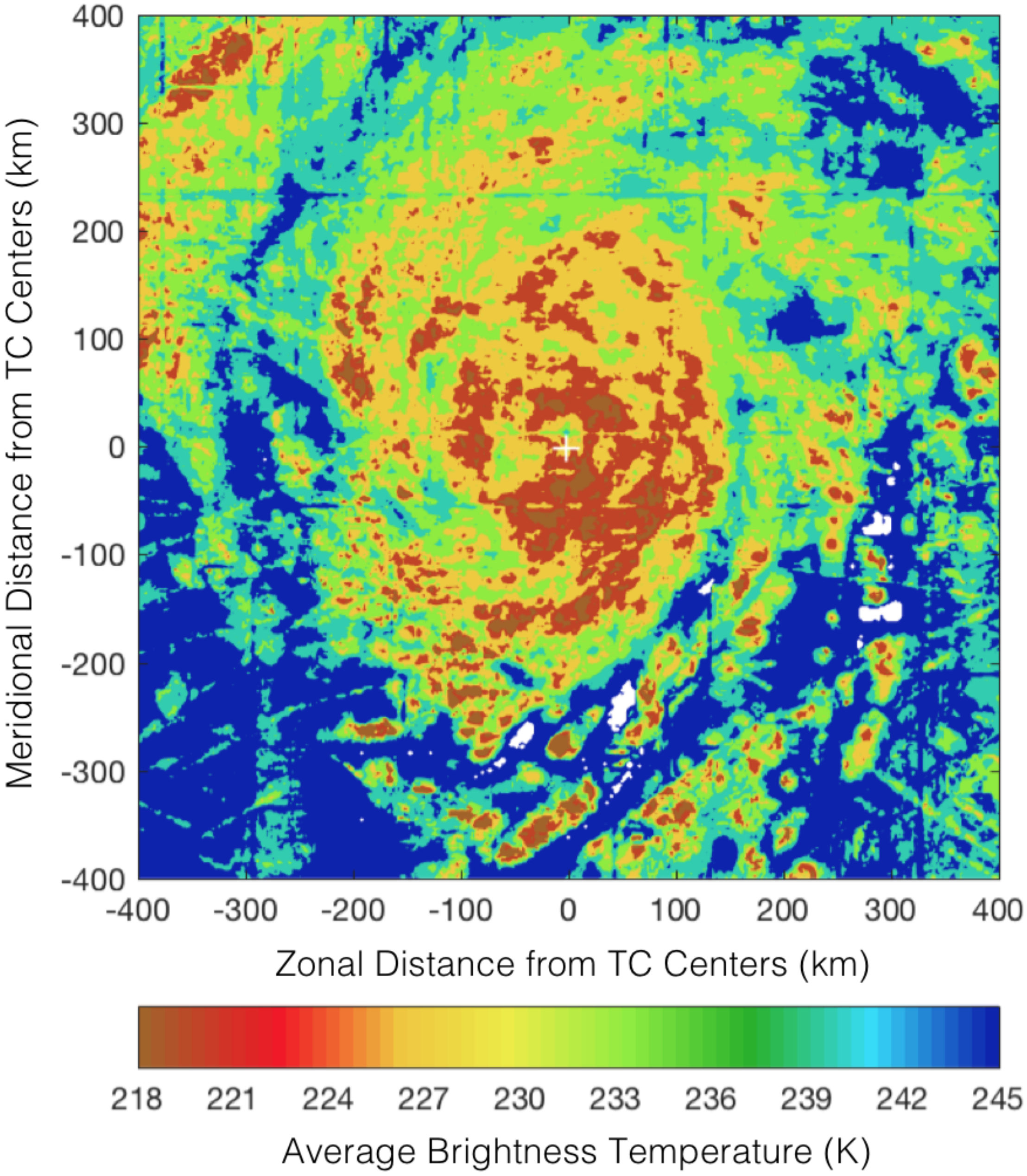

Figure 32: Composite average T_B as in Figure 22, except for TMI Category 3. White pixels in the image denote areas where $T_B > 245$ K for the entire dataset and are thus removed prior to the composite average process.

4.1.12 TMI Categories 4 and 5

TMI Category 4 and 5 composite average T_B imagery are depicted in Figure 33. T_B values for the entire figure range from 218-245 K, though areas where T_B was not < 245 K (for at least one individual TC image sample) are depicted in white. The intense convection in the core with T_B values 218-221 K occupies approximately the entire surface area within 100 km of the center point in all four quadrants. This concentric mass appears similar to that of a mesoscale convective complex (MCC); a common summertime phenomenon in the central region of the North American continent due to the areal extent of the cloud tops. This mass depicts the eye wall convection, which is axisymmetric and significantly wider than the eye wall convection in the Category 3 imagery. Thin areas relatively devoid of convection exist just beyond the outer periphery of the eye wall, which may depict the moat.

Overall, the T_B pattern depicts increased axisymmetry about the center point compared to the Category 3 imagery. Outer rain bands exist in all four quadrants. The elliptical distribution of the structure has shifted clockwise approximately 45 degrees, with the greatest extent in the SW and NE quadrants. Banding features extend up to 400 km from the center point in the NE and SW quadrants and up to 300 km from the center point in the NW and SE quadrants. The outer corners of the imagery in the NW and SE quadrants are largely devoid of any data beyond 200 km from the center point. The reason for this phenomenon is unclear, and may be a byproduct of the low sample size of individual TC images for Category 4 and 5.

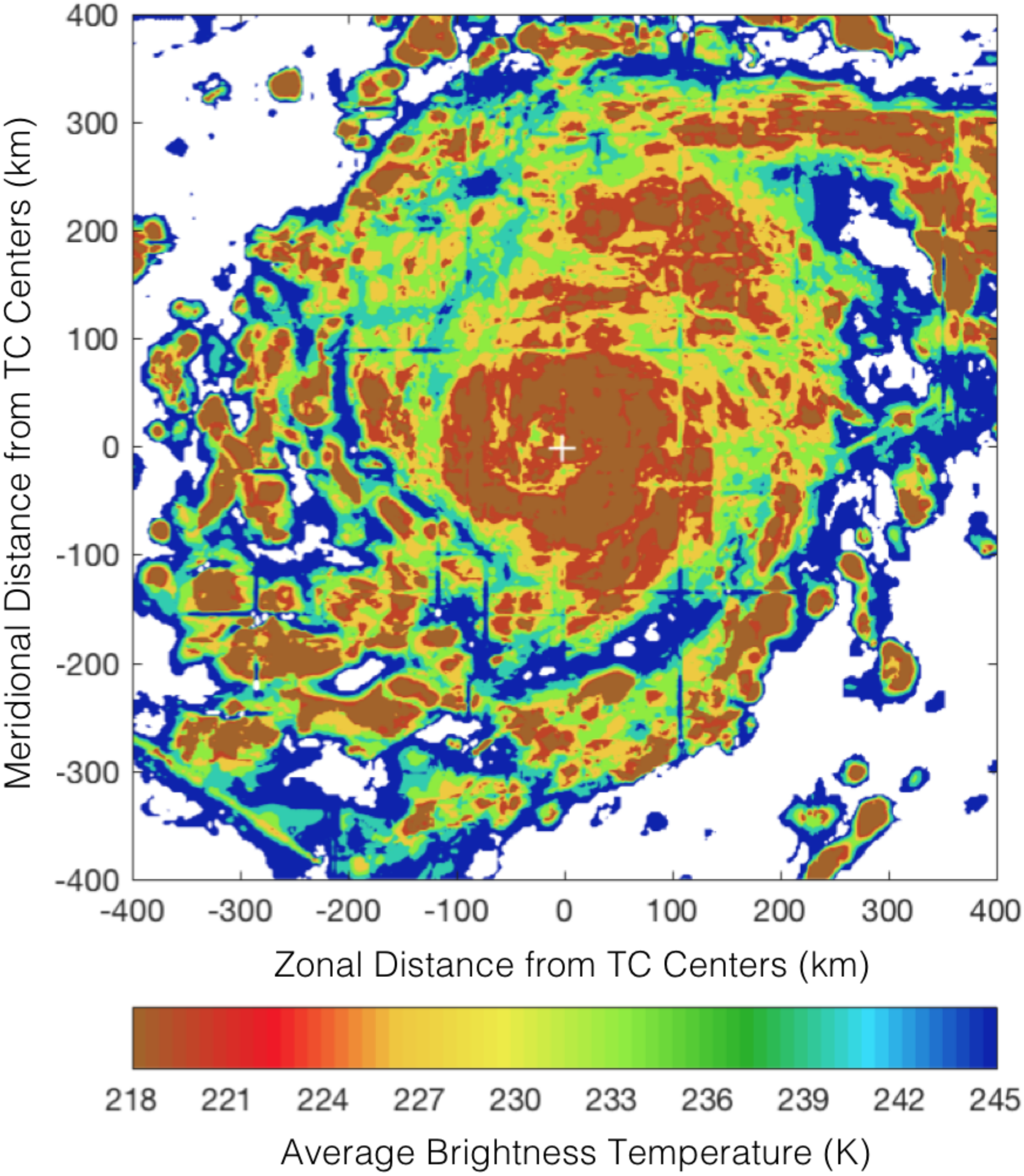

Figure 33: Composite average T_B as in Figure 22, except for TMI Categories 4 and 5. White pixels in the image denote areas where $T_B > 245$ K for the entire dataset and are thus removed prior to the composite average process.

4.2 Instrument Comparison Analysis

Various features in the T_B pattern for each microwave instrument, binned by TC intensity category, are identified in Section 4.1. The next step in the development of a subjective technique to assess TC intensity is to compare the features the microwave instruments have in common. Figures 22-33 will be annotated to highlight the T_B features discussed in the previous section. Notable areas of convection will be encompassed by a black closed curve, and an open black curve will highlight areas where banding is evident.

It is important to note that the analysis in the previous section focused on the actual T_B numeric values, as they are useful in a relative sense to depict the areas of the most intense convection, areas devoid of convection, and general TC structure. However, the numbers are simply averages, and are not useful as part of an operational technique to classify TC intensity using microwave imagery. Thus, specific T_B values and ranges of values are intentionally avoided in the TC intensity classification schematics. Additionally, areas of convection in the composite average imagery may resemble a circular or elliptical *mass* of convection, and are referred to in this manner for purposes of this paper. In practice, these depicted convective masses do not necessarily imply that the convection exists only in disorganized clusters. It is likely banding exists, and only resembles a convective mass due to the composite averaging process. Thus, the areas labeled as a convective mass in the below schematics imply the most likely area for banding features with higher convection intensity relative to other portions of the TC.

4.2.1 Category 1 Comparison

Three general characteristics are evident in the Category 1 TC composite average microwave imagery based on the spatial relationship of the T_B values relative to one another. Figure 34 depicts these three characteristics as a schematic for classifying TC microwave imagery intensity. First, the convection is displaced to the north and east of the TC center, as AMSR, SSMI/S, and TMI depict cooler T_B values in this region. These T_B relative minimum values extend up to 200 km from the TC center and are depicted in Figure 35. The depicted convective mass is not axisymmetric and is elliptical in nature in both the AMSR and TMI imagery. The elliptical convective mass is oriented with greater extent in meridional directions in both images.

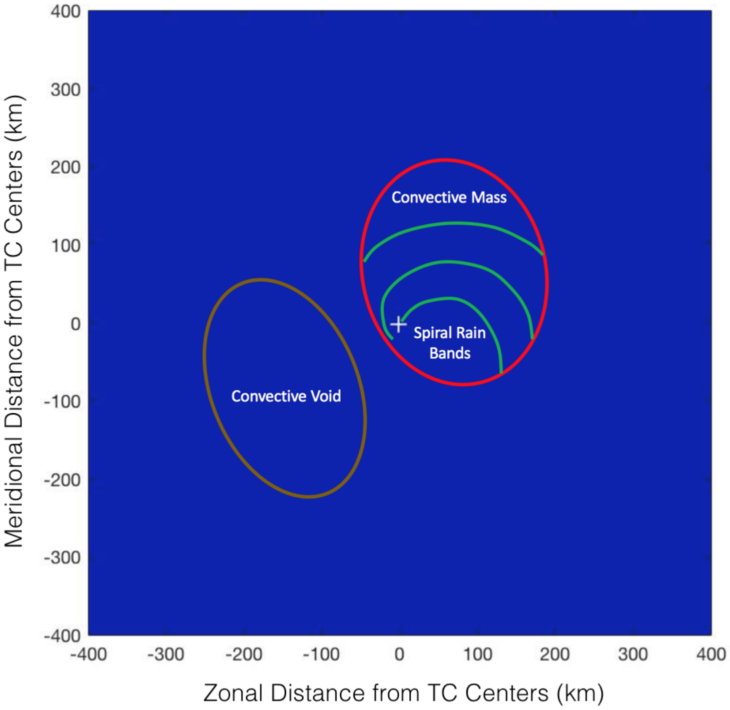

Figure 34: Generalized schematic depicting characteristics of a Category 1 TC in microwave imagery from 85-91 GHz. The red circle depicts the area that typically has the most intense convection. The brown circle depicts the region generally devoid of convection. The green curves depict the orientation and extent of weak spiral rain bands in the TC core.

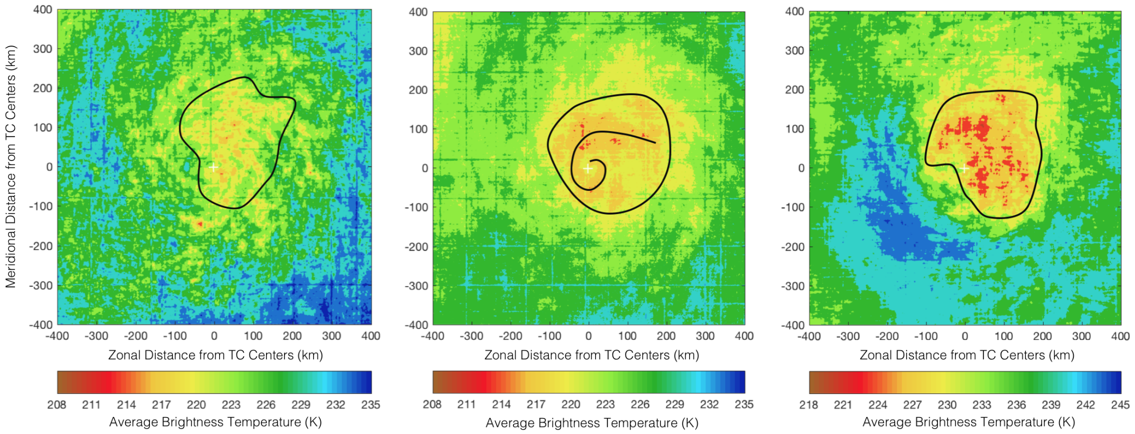

Figure 35: AMSR (left), SSMI/S (middle), and TMI (right) Category 1 composite average T_B. Black closed curves encompass regions where notable T_B values are discussed in the text and black open curves depict rain bands in the T_B pattern.

Next, significant banding is not evident in the AMSR and TMI imagery, whereas banding is evident in the SSMI/S imagery. Cooler T_B values 214-217 K are evident amidst the greater mass of 220 K convection. This apparent banding around the TC center is significantly less wide in the NW quadrant compared to the NE quadrant. Lastly, the SW quadrant is generally devoid of convection with an area of relatively warm T_B values evident in the TMI imagery.

4.2.2 Category 2 Comparison

Five general characteristics are evident in the Category 2 TC composite average microwave imagery based on the spatial relationship of the T_B values relative to one another. Figure 36 depicts these five characteristics as a schematic for classifying TC microwave imagery intensity. First, the strongest convection shifts to the west on TMI and SSMI/S and occupies a more compact area closer to the center for all sensor imagery as depicted in Figure 37. The extent of the most intense convection from the TC center decreases from 200 km to 100-150 km on AMSR and SSMI/S.

Next, an open eye wall is evident on AMSR imagery, extending out to 50 km from

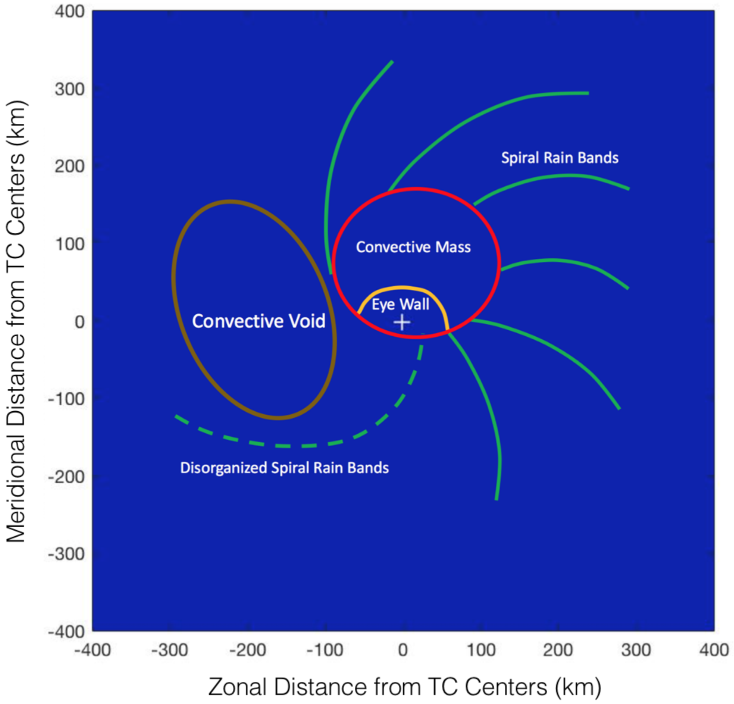

Figure 36: Generalized schematic depicting characteristics of a Category 2 TC in microwave imagery from 85-91 GHz. The red circle depicts the area that typically has the most intense convection. The orange open curve depicts the maximum extent of the eye wall convection. The solid green curves depict the orientation and extent of organized spiral rain bands. The dashed green curve depicts the orientation and extent of spiral rain bands more likely to be broken or disorganized compared to other banding features.

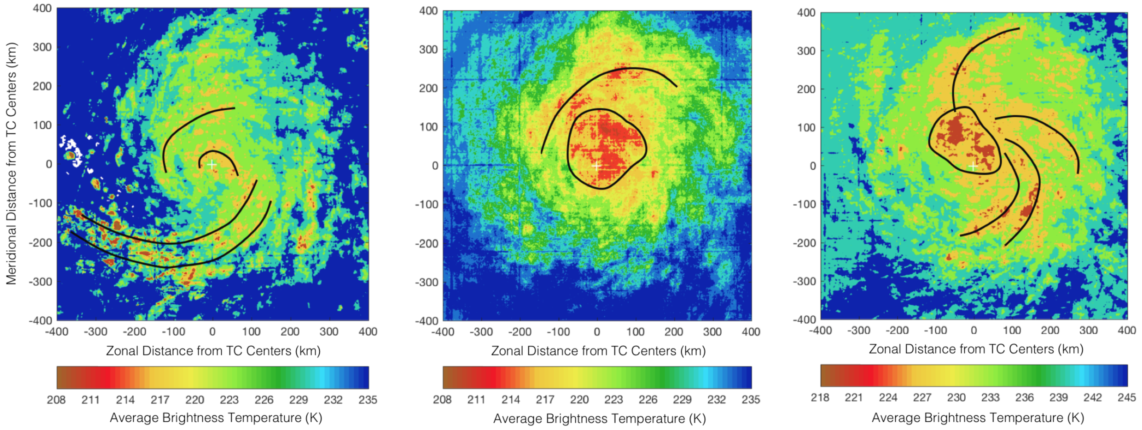

Figure 37: Composite average T_B as in Figure 35, except for Category 2.

the TC center. Intense convection also exists in this area on SSMI/S and TMI, and it is likely the eye wall is embedded in this convective mass. Next, spiral rain bands are evident on all sensor imagery, especially AMSR (which depicts two rain band features) and TMI. These banding features extend outward from the inner convective mass out to an average of 300 km from the TC center, and they primarily exist in the NW, NE, and SE quadrants.

Next, AMSR depicts outer banding features in the SE quadrant 200-400 km from the TC center, yet the convection appears broken and disorganized relative to the spiral rain bands in the other three quadrants. As axisymmetry improves in a favorable environment, banding features in this region of the TC will become more likely to exist. Lastly, the convective void depicted in the Category 1 schematic shifts north by approximately 100 km. This convection free region is evident on AMSR imagery north of the SW quadrant rain bands. TMI also depicts warmer T_B values in the same portion of the SW and NW quadrants.

4.2.3 Category 3 Comparison

Four general characteristics are evident in the Category 3 TC composite average microwave imagery based on the spatial relationship of the T_B values relative to one another. Figure 38 depicts these four characteristics as a schematic for classifying TC microwave imagery intensity. First, a closed eye wall is likely to exist based on axisymmetric regions of cold T_B values surrounding the TC center in AMSR, SSMI/S, and TMI imagery as depicted in Figure 39. This eye wall convection extends out to 75 km.

Next, banding is evident on SSMI/S in the NW quadrant and TMI in all four quadrants approximately 100 km from the TC center. These rain bands likely depict

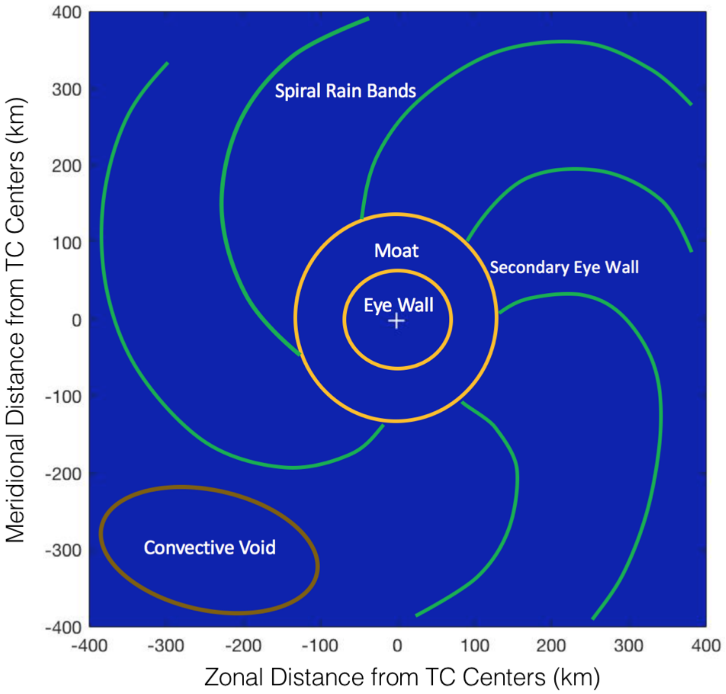

Figure 38: Generalized schematic depicting characteristics of a Category 3 TC in microwave imagery from 85-91 GHz. The orange circles depict the outermost extent of the primary and secondary eye walls with a moat between them. The solid green curves depict the orientation and extent of spiral rain bands. The brown circle depicts the region generally devoid of convection.

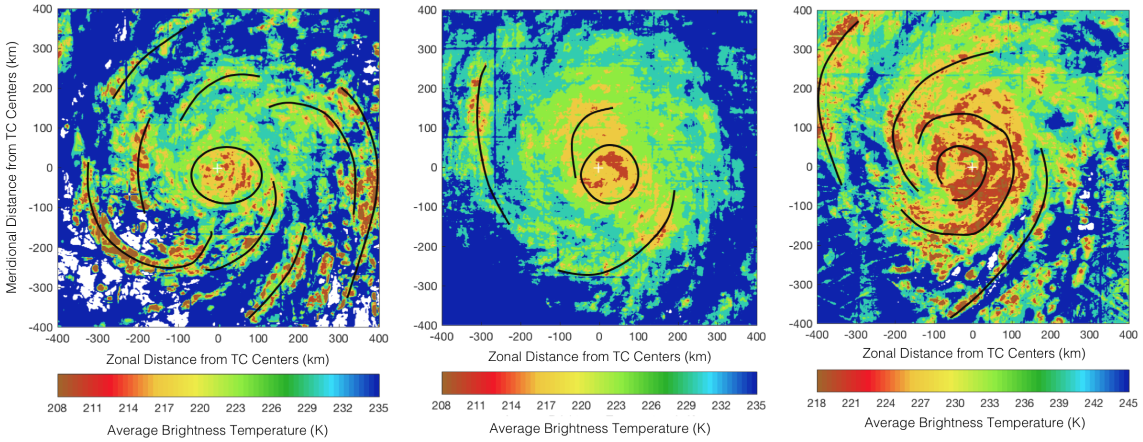

Figure 39: Composite average T_B as in Figure 35, except for Category 3.

the secondary eye wall, which moves inward to replace the primary eye wall. A moat typically exists between the two eye walls, and warmer T_B values are evident in this region beyond the inner eye wall for AMSR, SSMI/S, and TMI. Next, spiral rain bands exist in all four quadrants for all three microwave sensor images, as axisymmetry of the TC improves. These bands extend out to 400 km in all four quadrants, and AMSR depicts three or more bands. Lastly, a convective void exists in the SW quadrant with no convection evident in SSMI/S and TMI beyond 200 km. Convection does exist beyond 200 km in the SW quadrant in the AMSR imagery, but only eastern portion of the SW quadrant.

4.2.4 Categories 4 and 5 Comparison

Three general characteristics are evident in the Category 4 and 5 TCs composite average microwave imagery based on the spatial relationship of the T_B values relative to one another. Figure 40 depicts these three characteristics as a schematic for classifying TC microwave imagery intensity. First, the eye wall convection is more intense on AMSR, SSMI/S, and TMI with extremely cold T_B values within 100 km of the TC center as depicted in Figure 41. This dense, uniform ring of convection exists in all four quadrants across the 100 km radius of the eye wall in the SSMI/S and TMI imagery, similar in appearance to a small MCC.

Next, the secondary eye wall is evident beyond the inner eye wall convection, with banding extending 200 km from the TC center on AMSR, SSMI/S, and TMI in all four quadrants. The warmer T_B values between the dense inner eye convection and the secondary eye wall depict the moat, and this feature is more evident than in the Category 3 imagery. Lastly, the overall structure and axisymmetry of the TC for AMSR, SSMI/S, and TMI is similar to the Category 3 imagery with spiral rain bands extending out to 400 km in all four quadrants. The convective void no longer exists in the western portion of the SW quadrant.

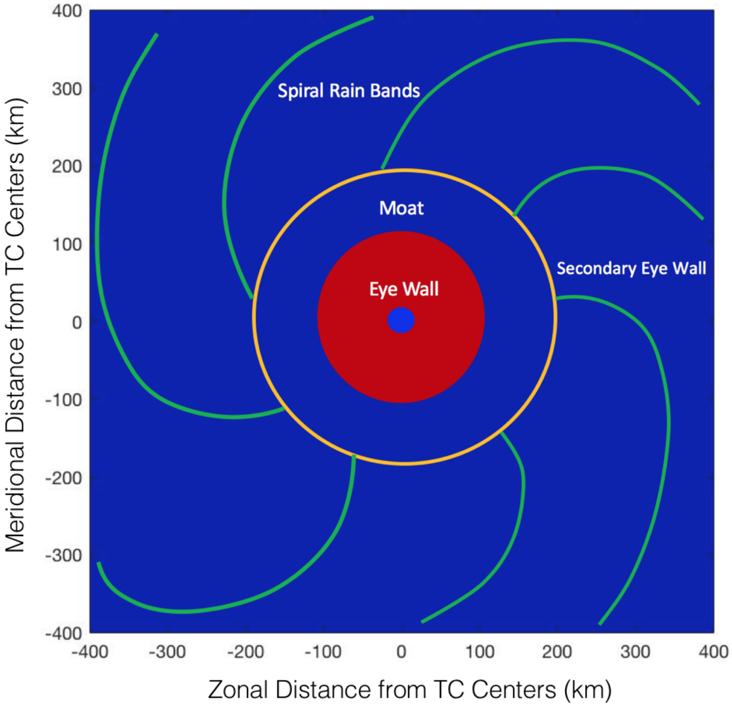

Figure 40: Generalized schematic depicting characteristics of Category 4 and 5 TCs in microwave imagery from 85-91 GHz. The solid red circle depicts the intense eye wall convection. The orange circle depicts the outermost extent of the secondary eye wall. The solid green curves depict the orientation and extent of spiral rain bands.

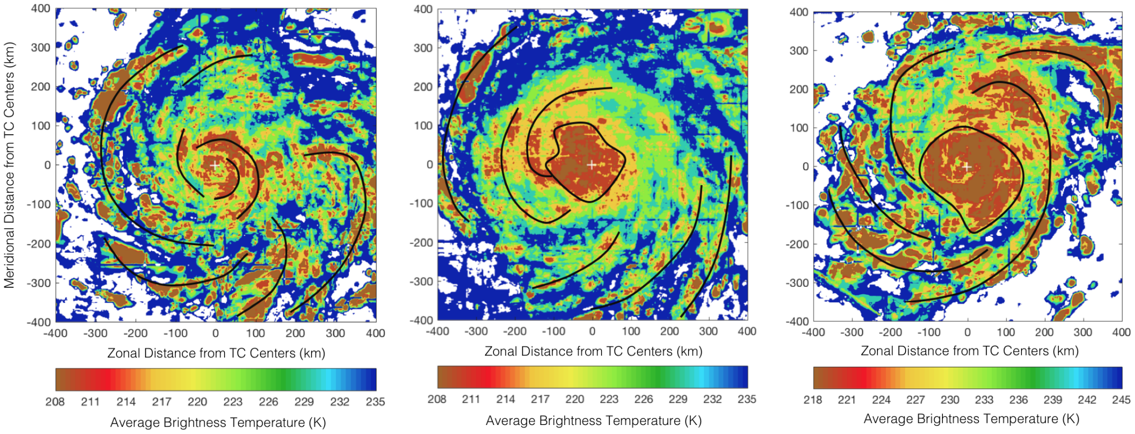

Figure 41: Composite average T_B as in Figure 35, except for Categories 4 and 5.

4.3 Microwave Intensity Technique Results Validation

The four schematics depicting TC characteristics in microwave imagery were developed based on an Atlantic basin dataset of composite average imagery. The result of this technique provides an estimate of TC intensity for a single microwave image. The use of Atlantic basin microwave imagery to validate this technique could present a bias as it was used in the process to create the four TC schematics. Thus, ten case studies are presented using only TCs in the Western Pacific basin. These cases were selected at random with a minimum of two cases per TC category. The intensity for each image is assessed using the idealized schematics, and this result is validated using the real-time best track estimated intensity assessed by JTWC. Best track is a subjective estimate of TC data assessed by JTWC personnel, as aircraft reconnaissance is rarely available in the Western Pacific basin.

4.3.1 Category 1 Results Validation

Two test cases are evaluated as examples of the results validation process for Category 1 TCs. First, SSMI/S imagery for Typhoon Dolphin (2015), depicted in Figure 42, is evaluated based the spatial relationship of the T_B values to imply the TC structure. The TC center is exposed on the SE side suggesting the core is not yet well formed. A lack of convection exists to the SW and NW of the center, whereas cool T_B values < 210 K are evident in the NE quadrant extending 200-300 km from the center. The SW quadrant is mostly devoid of convection beyond 75-100 km from the TC center. Based on these characteristics, Typhoon Dolphin (2015) resembles a Category 1 TC. Figure 34 is used as an overlay in Figure 42 to depict expected characteristics. JTWC assessed a best track intensity of 75 knots, thus, the microwave intensity assessment is in agreement as a Category 1 TC.

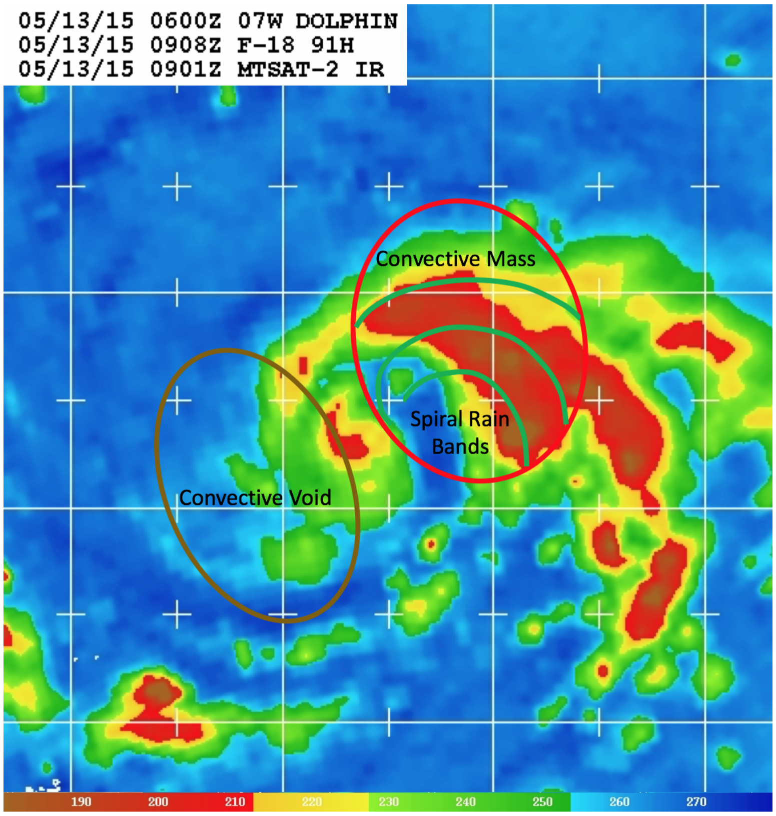

Figure 42: SSMI/S imagery for Typhoon Dolphin (2015) from 13 May at 0908 UTC. Solid white lines and hash marks depict lines of latitude and longitude, which are approximately 111 km apart from one another in zonal and meridional directions. The color scale depicts T_B values in K (Adapted from NRL 2017).

Next, SSMI/S imagery for Typhoon Megi (2010), depicted in Figure 43, is evaluated based the spatial relationship of the T_B values to imply the TC structure. The TC center is exposed on the SW side suggesting the core is not yet well formed. Cool T_B values < 210 K are evident 50-75 km NW of the center, whereas the majority of the convection is in the NE quadrant extending 100-200 km from the center and in the SE quadrant extending 200-300 km from the center. This convection depicts a single rain band wrapping around the NE portion of the TC. The SW quadrant is not devoid of convection, yet it contains a lower amount relative to the NE and SE quadrants. Based on these characteristics, Typhoon Megi (2010) resembles a Category 1 TC. Figure 34 is used as an overlay in Figure 43 to depict expected characteristics.

JTWC assessed a best track intensity of 65 knots, thus, the microwave intensity assessment is in agreement with the best track data as a Category 1 TC.

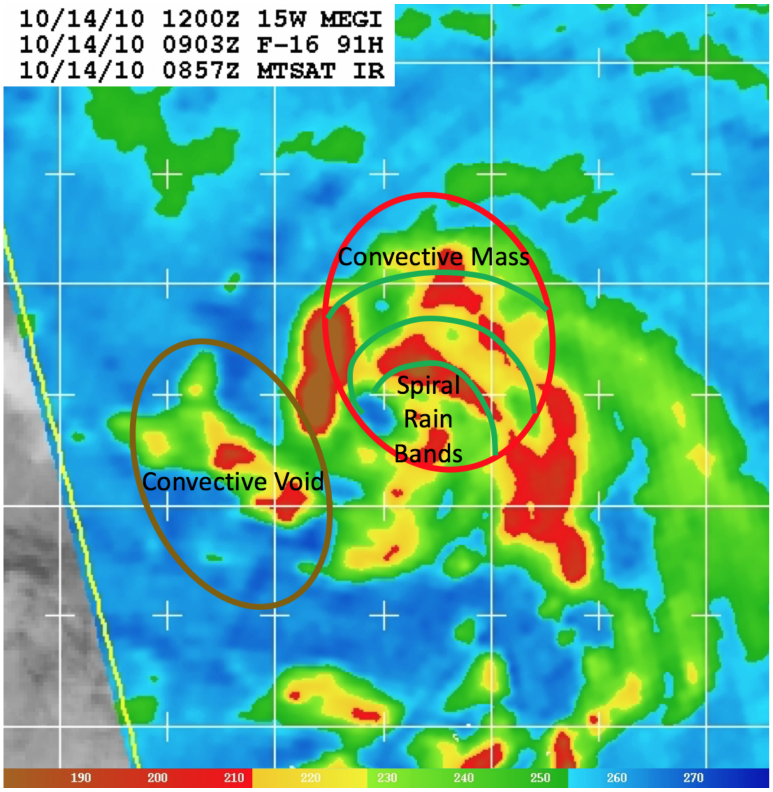

Figure 43: SSMI/S imagery as in Figure 42, except for Typhoon Megi (2010) from 14 October at 0903 UTC (Adapted from NRL 2017).

4.3.2 Category 2 Results Validation

Three test cases are evaluated as examples of the results validation process for Category 2 TCs. First, SSMI/S imagery for Typhoon Dolphin (2015), depicted in Figure 44, is evaluated based the spatial relationship of the T_B values to imply the TC structure. The TC center is exposed on the south side, whereas a partially formed eye wall does exist on the east, north, and west sides of the center. Two spiral rain bands are evident in the SE, NW, and NE quadrants. These features extend beyond 300 km from the TC center in the NE quadrant. The NW and SW quadrants are devoid of intense convection beyond the eye wall and an intense band that extends from the eye wall into the SE and SW quadrants. Based on these characteristics, Typhoon Dolphin (2015) resembles a Category 2 TC. Figure 36 is used as an overlay in Figure 44 to depict expected characteristics. JTWC assessed a best track intensity of 105 knots, thus, the microwave intensity assessment is not in agreement as a Category 2 TC.

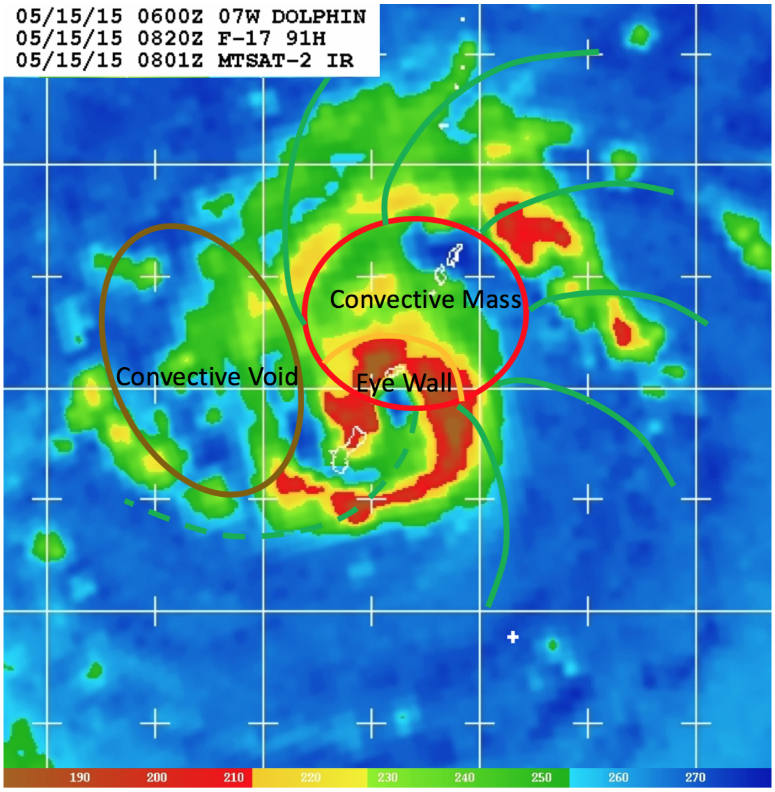

Figure 44: SSMI/S imagery as in Figure 42, except for Typhoon Dolphin (2015) from 15 May at 0820 UTC (Adapted from NRL 2017).

Next, SSMI/S imagery for Typhoon Krovanh (2015), depicted in Figure 45, is evaluated based the spatial relationship of the T_B values to imply the TC structure. The TC center is exposed on the south side, whereas a partially formed eye wall does exist on north side of the center. Individual spiral rain bands are not evident in the imagery, whereas an intense area of T_B values < 210 K exists extending 100 km north of the TC center. Weaker convection extends to 300 km from the TC center in the NE quadrant. The NW, SW and SE quadrants are devoid of convection beyond the eye wall. Based on these characteristics, Typhoon Krovanh (2015) resembles a Category 2 TC. Figure 36 is used as an overlay in Figure 45 to depict expected characteristics. JTWC assessed a best track intensity of 105 knots, thus, the microwave intensity technique assessment is not in agreement with the best track data as a Category 2 TC.

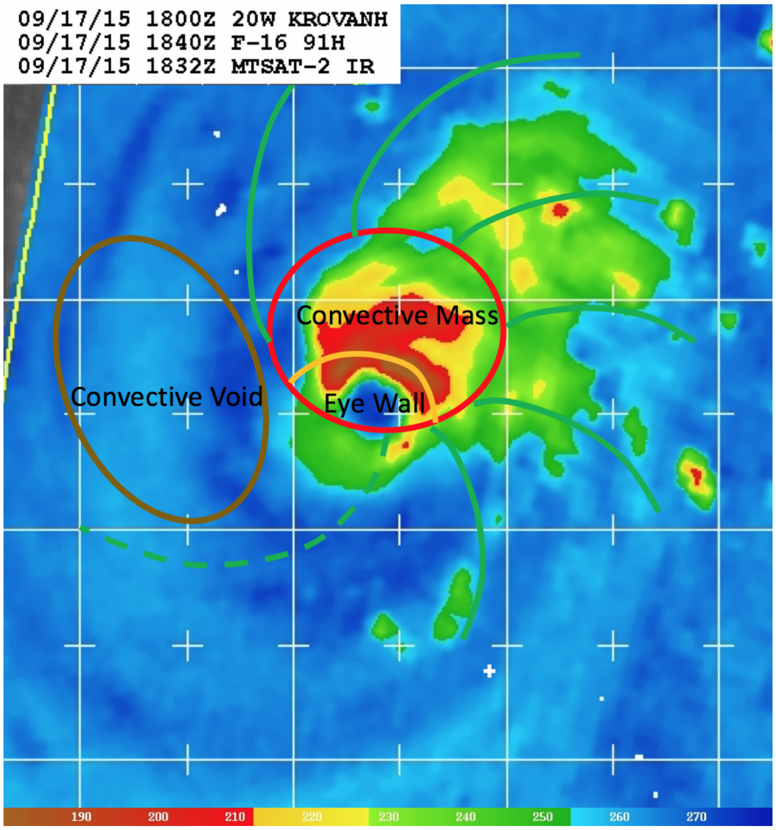

Figure 45: SSMI/S imagery as in Figure 42, except for Typhoon Krovanh (2015) from 17 September at 1840 UTC (Adapted from NRL 2017).

Typhoons Dolphin (2015) and Krovanh (2015) do not display the axisymmetric, closed eye wall characteristics of a Category 3 TC and do not appear to have a moat or secondary eye wall. Banding is not as extensive in the NW, SE, and SW quadrants as would be expected with a typical Category 3 TC. This result is indicative of the fact that the four TC schematics are based on a generalized average of a large data set and cannot account for subtle differences in structure across TC intensity categories. Not all Category 3 TCs have a closed, axisymmetric eye wall, a moat, a secondary eye wall, and banding extending beyond 300 km in all four quadrants.

Lastly, SSMI/S imagery for Typhoon Tembin (2012), depicted in Figure 46, is evaluated based the spatial relationship of the T_B values to imply the TC structure. A closed eye wall is evident, yet it is narrow on the south and east sides, extending 25 km or less from the TC center. Banding features are evident in the NE quadrant with a small, disorganized feature in the SE quadrant 200-250 km from the TC center. Additionally, convection extends beyond 300 km from the TC center in the NE quadrant. The NW and SW quadrants are devoid of intense convection beyond

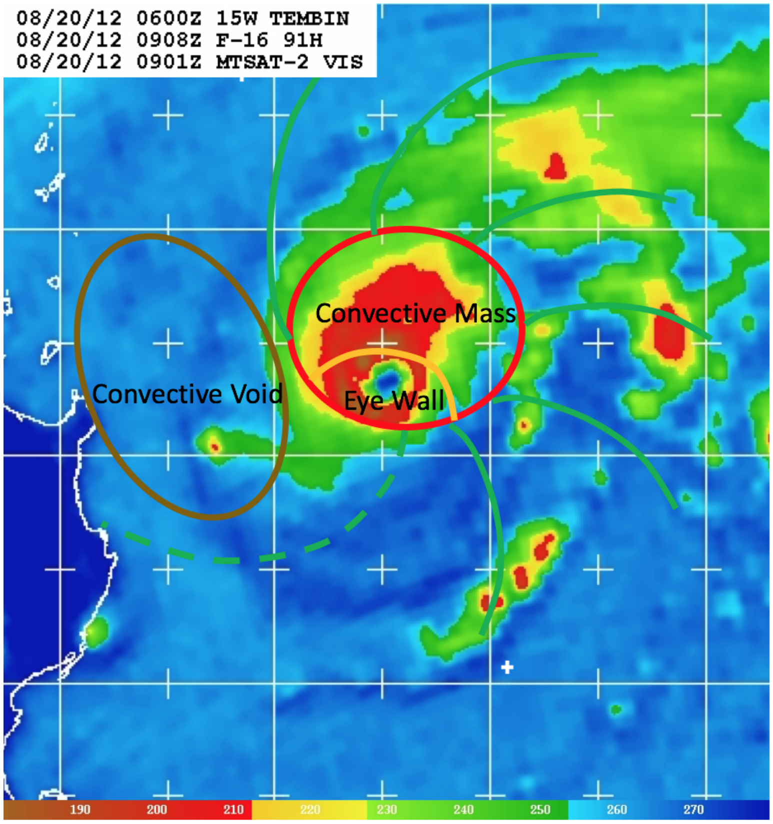

Figure 46: SSMI/S imagery as in Figure 42, except for Typhoon Tembin (2012) from 20 August at 0908 UTC (Adapted from NRL 2017).

the eye wall. Based on these characteristics, Typhoon Tembin (2012) resembles a Category 2 TC. Figure 36 is used as an overlay in Figure 46 to depict expected characteristics. JTWC assessed a best track intensity of 95 knots, thus, the microwave intensity assessment is in agreement with the best track data as a Category 2 TC.

4.3.3 Category 3 Results Validation

Three test cases are evaluated as examples of the results validation process for Category 3 TCs. First, SSMI/S imagery for Typhoon Rammasun (2008), depicted in Figure 47, is evaluated based the spatial relationship of the T_B values to imply the TC structure. A closed eye wall is evident extending 75 km from the TC center in

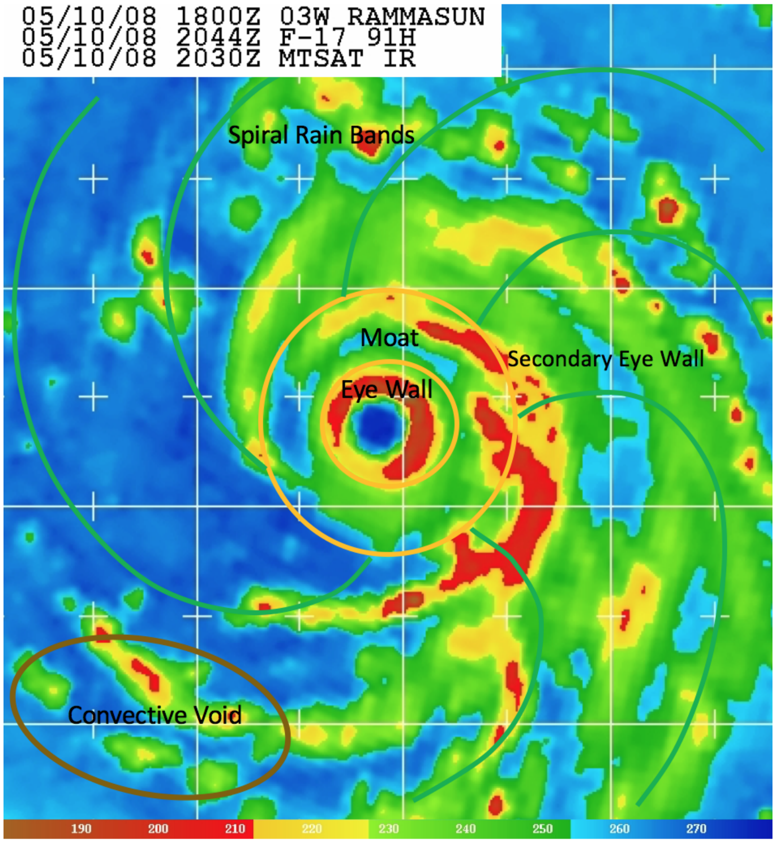

Figure 47: SSMI/S imagery as in Figure 42, except for Typhoon Rammasun (2008) from 10 May at 2044 UTC (Adapted from NRL 2017).

all four quadrants. Additionally, a partially formed secondary eye wall is evident 150 km from the TC center in the NE and SE quadrants. A moat with relatively little convection exists between the eye wall and the secondary eye wall. Banding features are evident in all four quadrants, though the NW quadrant is relatively devoid of convection in the western portions of the quadrant. These features extend up to 400 km from the TC center in all four quadrants. Based on these characteristics, Typhoon Rammasun (2008) resembles a Category 3 TC. Figure 38 is used as an overlay in Figure 47 to depict these characteristics. JTWC assessed a best track intensity of 130 knots, thus, the microwave intensity technique assessment is not in agreement with the best track data as a Category 3 TC.

Next, SSMI/S imagery for Typhoon Songda (2011), depicted in Figure 48, is evaluated based the spatial relationship of the T_B values to imply the TC structure. Typhoon Songda (2011) appears to be undergoing secondary eye wall replacement. A closed secondary eye wall extending 100 km from the TC center in all four quadrants surrounds an open, concentric region convection. This open, inner convection is likely an eye wall that is being replaced. A moat with relatively little convection exists between the eye wall and the secondary eye wall. Additionally, three distinct banding features are evident in the NW, NE, and SE quadrants. These features extend up to 300 km from the TC center in the NW and NE quadrants and up to 250 km in the SE quadrant. Based on these characteristics, Typhoon Songda (2011) resembles a Category 3 TC. Figure 38 is used as an overlay in Figure 48 to depict expected characteristics. JTWC assessed a best track intensity of 130 knots, thus, the microwave intensity assessment is not in agreement with the best track data as a Category 3 TC.

Lastly, SSMI/S imagery for Typhoon Talim (2017), depicted in Figure 49, is evaluated based the spatial relationship of the T_B values to imply the TC structure.

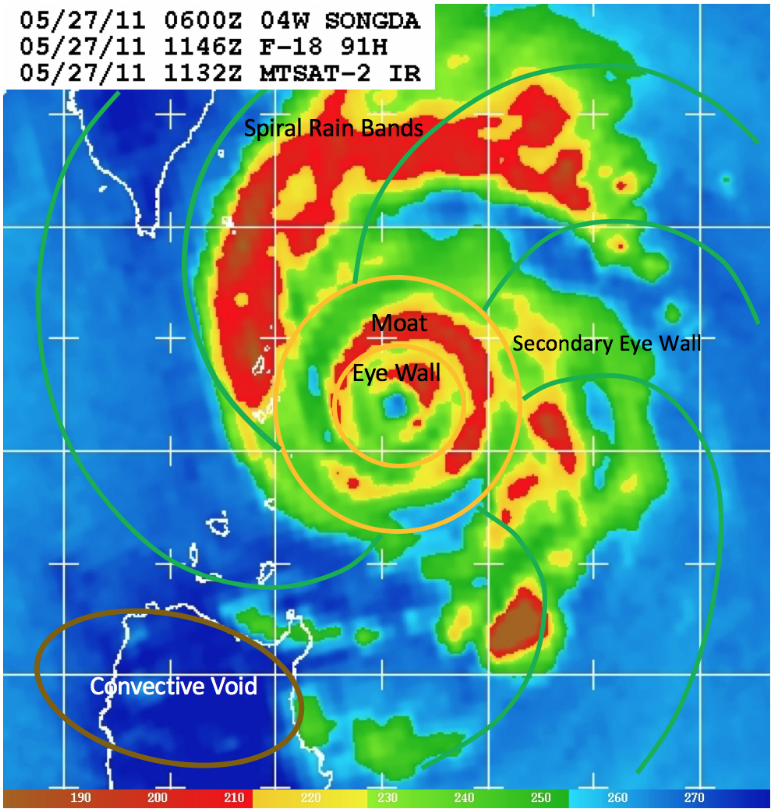

Figure 48: SSMI/S imagery as in Figure 42, except for Typhoon Songda (2011) from 27 May at 1146 UTC (Adapted from NRL 2017).

Typhoon Talim (2017) has a large convective void at the TC center. As a result, the core features extend beyond the typical maximum extent expected of a Category 3 TC. The eye wall convection is almost completely closed, yet is slightly exposed in the SW quadrant. Additionally, a partial secondary eye wall is evident in the SW and NW quadrants with a moat between the two eye walls. Banding features are evident in all four quadrants. These features are somewhat limited in organization beyond the apparent eye wall and secondary eye wall, and extend up to 350 km in the SW and NW quadrants, and up to 400 km in the NE and SE quadrants. Based on these characteristics, Typhoon Talim (2017) resembles a Category 3 TC. Figure 38 is used as an overlay in Figure 49 to depict expected characteristics. JTWC assessed a best track intensity of 70 knots, thus, the microwave intensity technique assessment is not in agreement with the best track data as a Category 3 TC.

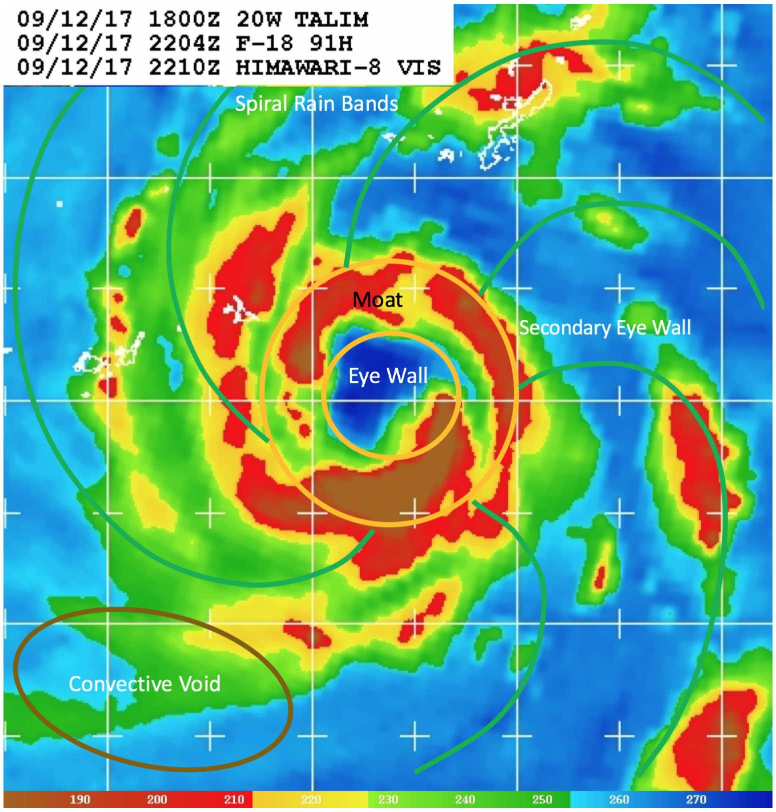

Figure 49: SSMI/S imagery as in Figure 42, except for Typhoon Talim (2017) from 12 September at 2204 UTC (Adapted from NRL 2017).

Typhoons Rammasun (2008), Songda (2011), and Talim (2017) were assessed differently using the microwave intensity schematics compared to the JTWC best track data. Typhoons Rammasun (2008) and Songa (2011) do not display the wide, concentric ring of very cold T_B values in the eye wall indicative of a Category 4 or 5 TC. Additionally, banding was not as extensive in the NW quadrant of Typhoon Rammasun (2008) and the NW and SW quadrants of Typhoon Songda (2011) as would be expected with a typical Category 4 or 5 TC. Typhoon Talim (2017) did not match the Category 3 schematic well due to the abnormally large eye, but it certainly did not match the Category 1 schematic at all. This result is indicative of the fact that the four TC schematics are based on a generalized average of a large data set, and cannot account for subtle differences in structure across TC intensity categories. No Category 4 data was available below 135 knots, necessitating the combination of the two highest categories in this paper. Thus, the microwave intensity technique is not likely to work well classifying Category 4 TCs. The reason for Typhoon Talim's (2017) axisymmetric core, banding, and eye wall despite its Category 1 intensity is unclear.

4.3.4 Categories 4 and 5 Results Validation

Two test cases are evaluated as examples of the results validation process for Category 4 and 5 TCs. First, SSMI/S imagery for Typhoon Haiyan (2013), depicted in Figure 50, is evaluated based the spatial relationship of the T_B values to imply the TC structure. A closed eye wall is evident extending 75-100 km from the TC center in all four quadrants. Additionally, the eye wall is comprised of a dense, wide region of cold T_B values < 210 K. A secondary eye wall is not evident, but a large region devoid of convection extends from the outer edge of the eye wall out to 200 km before additional banding features are observed. Spiral rain bands are evident in all four quadrants, though the SE quadrant contains only weak convection with T_B values generally > 230 K. These features extend up to 400 km from the TC center in the SW, NW, and NE quadrant. Based on these characteristics, Typhoon Haiyan (2013) resembles a Category 4 or 5 TC. Figure 40 is used as an overlay in Figure 50 to depict expected characteristics. JTWC assessed a best track intensity of 150 knots, thus, the microwave intensity assessment is in agreement with the best track data as a Category 5 TC.

Next, SSMI/S imagery for Typhoon Megi (2010), depicted in Figure 51, is evaluated based the spatial relationship of the T_B values to imply the TC structure.

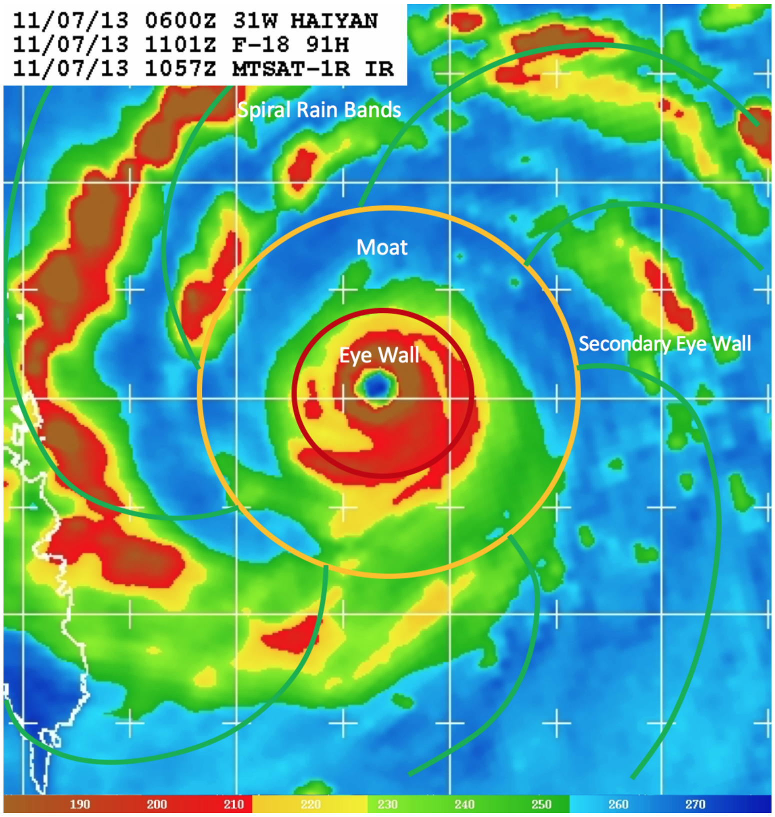

Figure 50: SSMI/S imagery as in Figure 42, except for Typhoon Haiyan (2013) from 7 November at 1101 UTC (Adapted from NRL 2017).

A closed eye wall is evident extending 75-100 km from the TC center in all four quadrants. Additionally, the eye wall is comprised of a dense, wide region of cold T_B values < 210 K. A partial secondary eye wall may exist north of the inner eye wall extending 100-150 km from the TC center, as a bounded region of warmer T_B values 220-230 K potentially comprising a moat exists 75-100 km from the TC center. Spiral rain bands are evident in all four quadrants, and these features extend 300-350 km from the TC center. Based on these characteristics, Typhoon Megi (2010) resembles a Category 4 or 5 TC. Figure 40 is used as an overlay in Figure 51 to depict expected characteristics. JTWC assessed a best track intensity of 155 knots, thus, the microwave intensity technique assessment is in agreement with the best track data as a Category 5 TC.

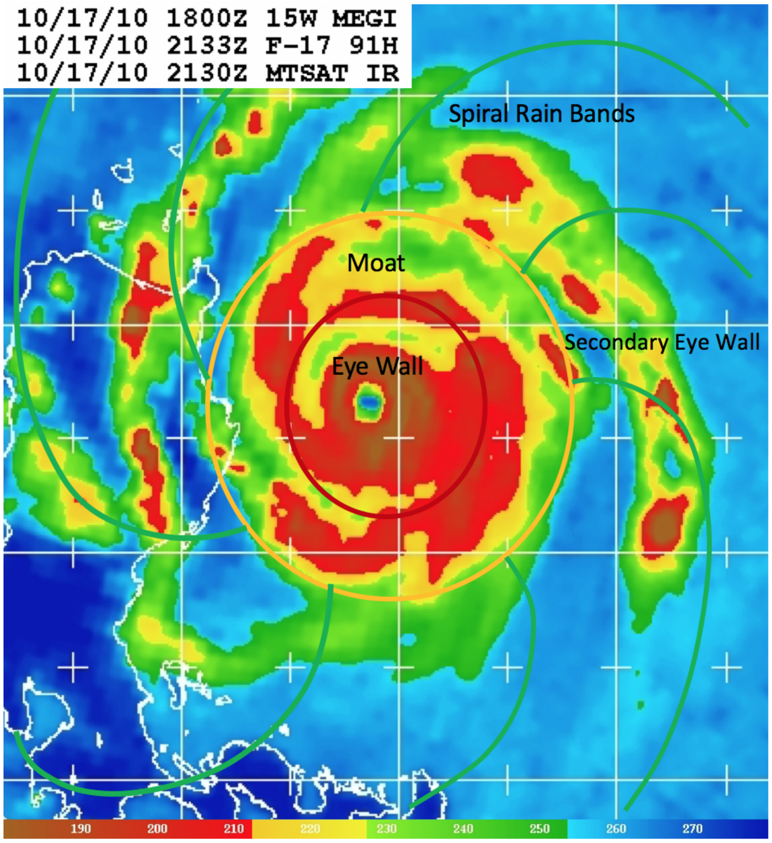

Figure 51: SSMI/S imagery as in Figure 42, except for Typhoon Megi (2010) from 17 October at 2133 UTC (Adapted from NRL 2017).

V. Conclusion

5.1 Summary

The motivation for this thesis arises from the necessity for the DoD to accurately forecast TC intensity. TC forecasts are dependent on real-time observations for data assimilation in NWP models. Remote sensing of TCs using satellite instruments in the visible and infrared spectra provide the majority of observations for deriving TC intensity over the ocean. However, these spectra are limited to sensing information at the cloud top, which can mask convective processes indicative of TC intensity. Microwave imagery provides TC information below the cloud top. Several frequencies are sensitive to the absorption of rain drops and scattering of ice crystals that occur in the intense convection that is indicative of TC intensity. A technique that utilizes microwave imagery to determine TC intensity can be a valuable tool in accurately characterizing these weather systems.

The background chapter provided the physical basis for the radiant intensity passively sensed by satellite instruments. Applicable microwave frequencies for oxygen, liquid water, and ice crystal absorption and scattering were provided along with supporting scientific data. A review of TC organization, structure, formation locations, and intensity classifications provided context to the meteorological phenomena at the center of this research. Furthermore, a description of the satellite instruments used to sense TC convection was necessary to understand the strengths and weaknesses of using microwave instruments to study TCs. Previous research cases in the utilization of T_B and TC intensity predictors provided ideas on how to formulate the methodology.

The methodology chapter described the data selected for this research and why it was selected. The NRL microwave imagery metadata and characteristics were necessary to explain how the images were acquired for each instrument. The data was sorted by TC intensity, and filtered to remove extraneous noise from the imagery. To facilitate the composite brightness averaging process, the color pixel values were converted to T_B values then normalized for data interpretation. Twelve composite average T_B images were produced for three microwave frequencies.

The analysis and results chapter explored the spatial relationship between the T_B values in the composite average T_B images. These relationships were compared to each of the three sensor types to identify common features. Combining these common features with the TC background information from Chapter II yielded four idealized TC schematics. These schematics were used as a subjective technique to assess TC intensity using only microwave imagery. This technique was applied to ten case studies encompassing four TC categories to validate the technique. Five successful and five unsuccessful TC intensity assessments were observed, and possible reasons why the technique did not work were provided.

5.2 Limitations

The technique developed in this study represents a first step in the utilization of microwave imagery to assess TC intensity. Several limiting factors influenced the outcome of the analysis and the results. First, the sample size of the data for the three instruments was not ideal. While SSMI/S had hundreds of images available for three of the intensity categories, AMSR has fewer than 100 samples for all but Category 1, and TMI had fewer than 100 samples available for Category 3, 4, and 5. None of the sensors had enough Category 4 or 5 images for a composite average technique to be useful, so the categories were combined. Thus, the combined Category 4 and 5 imagery encompassed a broad range of intensities. Additionally, since no imagery with Category 4 winds below 135 knots was available, Category 4 TCs are unable to be classified using this technique as was discussed in the results section.

Next, the composite average method produced a singular result for a large dataset. This imagery was useful as the foundation for producing the TC schematics, but in operational practice it is unlikely a TC microwave image will fit perfectly into one of the four categorical schematics. Additionally, it is unlikely that TCs with a unique or uncommon structure will be assessed correctly, such as annular, midget, or subtropical TCs. Furthermore, even if the TC category is assessed correctly, the intensity is still ambiguous. The TC categories in this paper encompass a range of 15-20 knots, which is too large of a range of values if the objective is to accurately assess TC intensity.

Lastly, this technique was developed using only the best track wind values and the spatial relationship of T_B values. In real-world operations, a TC forecaster has additional data available for context. Visible and infrared imagery, automated wind intensity algorithms, and TC intensity history should be used as part of the assessment process. An intensifying or decaying TC may have a different structural appearance in microwave imagery. Due to the inherent spatial and temporal limitations of microwave remote sensing, it is not ideal to assess TC intensity as a standalone process. Additional types of data should be used to augment microwave imagery to obtain an accurate result.

5.3 Future Work

Further work is necessary to improve techniques to accurately assess TC intensity utilizing microwave imagery. The data set for this paper was limited to the Atlantic Ocean as higher confidence exists in the wind intensity measured by aircraft. The inclusion of additional ocean basins would bolster the low sample size values for the number of TC images included in the composite average process, and may improve the technique. Extraordinarily large data sets may require the use of machine learning for pattern recognition in the future.

Expanding the binned intensity categories may increase confidence and usefulness of the technique. TCs could be separated into 5-10 knot bins. Additionally, the data could be filtered for specific TC types such as annular, midget, and subtropical TCs. Separating TCs that are intensifying or decaying may also be useful, as well as filtering TCs into a separate category if they interact with land.

Lastly, additional work is required to test and validate the results of this research. Only ten case studies were included in the results validation section, which is too small a sample size to confirm the usefulness of this technique. Thousands of TC microwave images exist for further validation of these results. Additional application of this technique would refine the process and ideally reach the end-state of this research topic.

References

Bain, L. J., and M. Engelhardt, 1991: *Introduction to Probability and Mathematical Statistics.* 2nd ed., Duxbury Press, 466 pp.

Brueske, K. F., and C. S. Velden, 2003: Satellite-based tropical cyclone intensity estimation using the NOAA-KLM series Advanced Microwave Sounding Unit (AMSU). *Mon. Wea. Rev.*, **131**, 687–697.

Cecil, D. J., and E. J. Zipser, 1999: Relationships between tropical cyclone intensity and satellite-based indicators of inner core convection: 85-ghz ice-scattering signature and lightning. *Mon. Wea. Rev.*, **127**, 103–123.

Center for Satellite Applications and Research, cited 2017, Advanced Scatterometer imagery archive. [Available from https://manati.star.nesdis.noaa.gov/datasets/ASCATData.php].

Chan, J. C., and J. D. Kepert, 2010: *Global Perspectives on Tropical Cyclones: From Science to Mitigation*, Vol. 4. World Scientific, 448 pp.

Du, J., J. S. Kimball, J. Shi, L. A. Jones, S. Wu, R. Sun, and H. Yang, 2014: Inter-calibration of satellite passive microwave land observations from amsr-e and amsr2 using overlapping fy3b-mwri sensor measurements. *Remote Sens.*, **6**, 8594–8616.

Dvorak, V. F., 1975: Tropical cyclone intensity analysis and forecasting from satellite imagery. *Mon. Wea. Rev.*, **103**, 420–430.

Figa-Saldaña, J., J. J. Wilson, E. Attema, R. Gelsthorpe, M. Drinkwater, and A. Stoffelen, 2002: The advanced scatterometer (ASCAT) on the meteorological operational (MetOp) platform: A follow on for European wind scatterometers. *Can. J. Remote Sensing*, **28**, 404–412.

Hawkins, J. D., F. J. Turk, T. F. Lee, and K. Richardson, 2008: Observations of tropical cyclones with the ssmis. *IEEE Trans. Geosci. Remote Sens.*, **46**, 901–912.

Kidder, S. Q., M. D. Goldberg, R. M. Zehr, M. DeMaria, J. F. Purdom, C. S. Velden, N. C. Grody, and S. J. Kusselson, 2000: Satellite analysis of tropical cyclones using the advanced microwave sounding unit (amsu). *Bull. Amer. Meteor. Soc.*, **81**, 1241–1259.

———, S. Q., W. M. Gray, and T. H. Vonder Haar, 1978: Estimating tropical cyclone central pressure and outer winds from satellite microwave data. *Mon. Wea. Rev.*, **106**, 1458–1464.

———, S. Q., and T. H. V. Haar, 1995: *Satellite Meteorology: An Introduction.* Gulf Professional Publishing, 466 pp.

Kummerow, C., W. Barnes, T. Kozu, J. Shiue, and J. Simpson, 1998: The tropical rainfall measuring mission (trmm) sensor package. *J. Atmos. Oceanic Technol.*, **15**, 809–817.

Lee, T. F., F. J. Turk, J. Hawkins, and K. Richardson, 2002: Interpretation of trmm tmi images of tropical cyclones. *Earth Interactions*, **6**, 1–17.

Mapes, B., R. Milliff, and J. Morzel, 2009: Composite life cycle of maritime tropical mesoscale convective systems in scatterometer and microwave satellite observations. *J. Atmos. Sci.*, **66**, 199–208.

Naval Research Laboratory, cited 2017, Tropical cyclone microwave imagery archive. [Available from https://www.nrlmry.navy.mil/TC.html].

Petty, G., 2006: *A First Course In Atmospheric Radiation*. 2nd ed., Sundog Publishing, 452 pp.

Poe, G., K. Germain, J. Bobak, S. Swadley, J. Wessel, B. Thomas, J. Wang, and B. Burns, 2001: Dmsp calibration/validation plan for the special sensor microwave imager sounder (ssmis). *Naval Research Laboratory Rep.*, 1–32.

Raschke, E., 2013: *Radiation And Water In The Climate System: Remote Measurements*, Vol. 45. 1st ed., Springer Science & Business Media, 617 pp.

Sitkowski, M., J. P. Kossin, and C. M. Rozoff, 2011: Intensity and structure changes during hurricane eyewall replacement cycles. *Mon. Wea. Rev.*, **139**, 3829–3847.

Velden, C., B. Harper, F. Wells, J. L. Beven, R. Zehr, T. Olander, M. Mayfield, C. C. Guard, M. Lander, R. Edson, L. Avila, A. Burton, M. Turk, A. Kikuchi, A. Christian, P. Caroff, and P. McCrone, 2006: The Dvorak tropical cyclone intensity estimation technique: A satellite-based method that has endured for over 30 years. *Bull. Amer. Meteor. Soc.*, **87**, 1195–1210.

Wacker, R., 2005: Correcting for precipitation effects in satellite-based passive microwave tropical cyclone intensity estimates. Ph.D. thesis, University of Wisconsin Madison, 146 pp.

Warner, T. T., 2010: *Numerical Weather and Climate Prediction*. Cambridge University Press, 526 pp.

Wilheit, T., A. Chang, M. V. Rao, E. Rodgers, and J. S. Theon, 1977: A satellite technique for quantitatively mapping rainfall rates over the oceans. *J. Appl. Meteo.*, **16**, 551–560.

REPORT DOCUMENTATION PAGE

Form Approved
OMB No. 0704-0188

1. REPORT DATE *(DD-MM-YYYY)* 22-03-2018	**2. REPORT TYPE** Master's Thesis	**3. DATES COVERED** *(From - To)* Sept 2016 - Mar 2018

4. TITLE AND SUBTITLE

Methodology to Analyze Tropical Cyclone Intensity from Microwave Imagery

5a. CONTRACT NUMBER

5b. GRANT NUMBER

5c. PROGRAM ELEMENT NUMBER

6. AUTHOR(S)

Perkins, Matthew W., Captain, USAF

5d. PROJECT NUMBER

5e. TASK NUMBER

5f. WORK UNIT NUMBER

7. PERFORMING ORGANIZATION NAME(S) AND ADDRESS(ES)

Air Force Institute of Technology
Graduate School of Engineering and Management (AFIT/EN)
2950 Hobson Way
Wright-Patterson AFB OH 45433-7765

8. PERFORMING ORGANIZATION REPORT NUMBER

AFIT-ENP-18-M-094

9. SPONSORING/MONITORING AGENCY NAME(S) AND ADDRESS(ES)

Joint Typhoon Warning Center
Attn: Robert J. Falvey 425 Luapele Road
Pearl Harbor, HI 96860-3103
COMM 808-474-3946, FAX 808-471-5676
Email: robert.falvey.1@us.af.mil

10. SPONSOR/MONITOR'S ACRONYM(S)

JTWC

11. SPONSOR/MONITOR'S REPORT NUMBER(S)

12. DISTRIBUTION/AVAILABILITY STATEMENT

DISTRIBUTION STATEMENT A:
APPROVED FOR PUBLIC RELEASE; DISTRIBUTION UNLIMITED.

13. SUPPLEMENTARY NOTES

This material is declared a work of the U.S. Government and is not subject to copyright protection in the United States.

14. ABSTRACT

Satellites with microwave remote sensing capabilities can be utilized to study atmospheric phenomena through high-level cloud cover (particularly cirrus), an advantage over visible and infrared bands, which only sense cloud tops. This unique capability makes microwave imagery ideal for studying the cloud structures of tropical cyclones (TCs) in detail, and relating these features to TC intensity. Techniques to estimate the intensity of TCs using infrared imagery, such as the Dvorak technique, have been used in TC forecasting for 40 years. However, due to the inherent temporal limitations of microwave imagery, no such similar technique exists for the microwave spectrum. This study utilizes pattern recognition to develop a subjective technique for estimating TC intensity using microwave imagery. The dataset includes TC composite imagery from the Special Sensor Microwave Imager (85 GHz), Advanced Microwave Scanning Radiometer-Earth Observing System (89 GHz), Advanced Microwave Scanning Radiometer 2 (89 GHz), and the Special Sensor Microwave Imager/Sounder (91 GHz) from the Atlantic basin, and aircraft reconnaissance data are used for verification. The composite imagery is binned into four categories to facilitate detection of common patterns for TCs of similar size and estimated intensity. This analysis provides the foundation for a new method to estimate TC intensity when aircraft data are unavailable. Multiple techniques are applied to explore relationships between brightness temperature values and TC intensity, and ten test cases in the Western Pacific basin are presented to validate the results. Five out of the ten TCs were classified correctly applying the microwave intensity techniques developed by this analysis.

15. SUBJECT TERMS

Tropical Cyclone Intensity Estimates, SSMI/S, AMSR, TMI Remote Sensing, Satellite Meteorology, Tropical Meteorology, Tropical Cyclone Forecasting, Hurricanes

16. SECURITY CLASSIFICATION OF:			**17. LIMITATION OF ABSTRACT**	**18. NUMBER OF PAGES**	**19a. NAME OF RESPONSIBLE PERSON**
a. REPORT	**b. ABSTRACT**	**c. THIS PAGE**			Robert A. Stenger, Ph.D., Altamira Technologies Corporation
U	U	U	UU	111	**19b. TELEPHONE NUMBER** *(Include area code)* (937) 490-4884 Robert.Stenger@Altamiracorp.com